

https://dspace.org/

Modelling capacitive-coupled electromanetic interference for electromyography sensors on upper limb amputees

Ambelal, Deepam Yasvant

2022

https://hdl.handle.net/10539/34150

Downloaded from a DSpace repository. https://dspace.org/

MODELLING CAPACITIVE-COUPLED ELECTROMAGNETIC INTERFERENCE FOR ELECTROMYOGRAPHY SENSORS ON UPPER LIMB AMPUTEES

Deepam Yasvant Ambelal

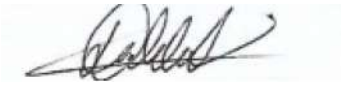
A dissertation submitted to the Faculty of Engineering and the Built Environment, University of the Witwatersrand, Johannesburg, in fulfilment of the requirements for the degree of Master of Science in Engineering.

Johannesburg, 2021

DECLARATION

I declare that this dissertation is my own unaided work. It is being submitted for a degree of Master of Science in Engineering at the University of the Witwatersrand, Johannesburg. It has not previously been submitted for any degree or examination to any other university.

The financial assistance of the National Research Foundation (NRF) towards this research is hereby acknowledged. Opinions expressed and conclusions arrived at, are those of the author and are not necessarily to be attributed to the NRF



Deepam Yasvant Ambelal

13 November 2021

Date

ABSTRACT

Prosthetics are used to substitute for the missing limb sections to aid the amputee's mobility and quality of life. The shift towards electromyography (EMG) -controlled hand prosthetics from mechanical ones is to offer multiple movements or gestures. This transition in environments with electrically-powered devices results in the challenge of noise interference. Capacitively-coupled electromagnetic interference (CC-EMI) is the predominant noise source and it is found almost everywhere.

An example scenario is an upper limb amputee person grasping a household lamp's cable with their non-amputated hand. EMI is expected to galvanically circulate through the body from the dipole source. Therefore, the suitable selection of the instrumentation amplifier's common mode rejection ratio (CMRR) is important. Limited literature shows it is possible to determine the EMI in the body using MRI scans-based FEM modelling, however, it is costly and time-consuming to process. Human body electric circuit models are used for high electrocution scenarios but are not applicable for the scenario. This research addresses the problem by modelling the hand-to-hand (H2H) region of the human body as an electric circuit, to determine the CC-EMI magnitude at the site of an EMG sensor.

The model developed has three sub-models: The capacitive-coupling (CC) circuit model, the human body circuit model, and the EMI measurement circuit model. The circuit model for the CC between the power cable and the grasping hand was developed using COMSOL simulations. The measurement system circuit model is considered to be a pair of voltage followers with hydrogel electrode inputs. The human body model is the main model and the development was based on modifying the Freiberger human body model. The Freiberger model was modified into a ladder

network where the upper limb circuit path was split into two transverse paths using parallel resistor theory. Along with genetic algorithm optimization, impedances for the multiple loops were obtained between the two hands in order to mimic galvanic circulation and its paths.

The model was applied for the scenario using 18 healthy, un-amputated participants grasping an insulated, flat, two-core power cable for a lamp in a controlled environment. The experiment evaluated four cases which covered the combinations of using each hand to grasp the cable and two rotational orientations of the cable in the grasp. The average error across all participants for modelling the four cases was 27.4 %. The lowest average error achieved for a single participant was 9.6 %. The error magnitudes were considered acceptable because it was achieved using more accessible equipment than using MRI scans-based FEM modelling.

Validation was conducted with a lightly modified scenario and confirms that alternate scenarios can be simulated for the same participant by modifications to the sensor position and/or the CC sub-model. Thus the CMRR can be determined from the EMI evaluations of multiple scenarios.

ACKNOWLEDGEMENTS

The author would like to acknowledge with gratitude the support rendered by both Dr M.V. Shuma-Iwisi and Mr A.K. Mohamed. The author would also like to express gratitude to the National Research Foundation (NRF) for support funding through the Grantholder-Linked Student Support Programme.

CONTENTS

Declaration i

Abstract ii

Acknowledgements iv

List of Figures x

List of Tables xv

Nomenclature xviii

Chapter 1 Introduction 1

1.1. Context to Research Carried Out 2

1.2. Electromyography 2

1.3. Noise in EMG Sensors 3

1.4. Electromagnetic Interference (EMI) noise 4

1.4.1. Capacitively-Coupled Electromagnetic Interference (CC-EMI) 4

1.5. Problem Identification 6

1.5.1. Model Requirements 7

1.5.2. Research Question 9

1.5.3. Research Contributions 10

1.6. Chapter Summary 11

Chapter 2 Human Body Electric Circuit Models & Human Tissue Electrical Characteristics 13

2.1. Galvanic Circulation 13

2.1.1. Discussion 15

2.2. Human Body Impedance 16

2.2.1. Freiberger Human Body Model [35] 17

2.2.2. Discussion 19

2.3. Electrical Properties of Human Tissue 20

2.3.1. Assumptions 21

2.4. Chapter Summary 21

Chapter 3 Proposed Model 22

3.1. Capacitive-Coupling Source Model 22

3.1.1. Conceptualising the Electric Field on the grasped Type P3 cable .. 23

3.1.2. Modelling Capacitance on a grasped, flat power cable 24

3.1.3. Capacitance on a Grasped Flat Power Cable: COMSOL modelling 25

3.1.4. Discussion 28

3.2. Development of the Human Body Circuit Model 29

3.2.1. Modification 1: Modifying Percentages of the Hand-To-Hand Impedance 29

3.2.2. Modification 2: Reducing original Model Scope to Hand-to-hand Model 30

3.2.3. Modification 3: Introducing the 2nd Pathway using Parallel-Resistor Theory 32

3.2.4. Modification 4: Introducing Inter-Pathway Resistances for Multiple Galvanic Flow Paths and H2H Capacitance 32

3.2.5. Modification 5: Dividing Bicep area of Upper Arm for placement of Bipolar electrode nodes 35

3.2.6. Discussion 37

3.3. Chapter Summary 38

Chapter 4 Experimentation & Results 39

4.1. Experimental Environment and Component Design 39

4.1.1. Environment Setup 40

4.1.2. Measurement System 43

4.2. Experiment Procedure 48

4.2.1. Preparation 48

4.2.2. Participant Parameter measurements 48

4.2.3. Experiment 51

4.2.4. Discussion 55

4.3. Results 56

4.3.1. Participant Parameter Measurements 56

4.3.2. Experiment Measurements 57

4.3.3. Experiment Data Analysis 65

4.3.4. Experiment Discussion 69

4.4. Chapter Summary 70

Chapter 5 Model Assembly and Optimization 72

5.1. Unified Model of Experiment 72

5.2. Model Optimisation Results and Error Calculations 75
5.2.1. 'Naturally Selected' Parameters *Z*, *Y*, *X*, *W* and *V* Combinations ... 76
5.2.2. Averaged Output Voltages with Relative Error 78
5.2.3. *V(Out_A) – V(Out_B)* Magnitude Comparison 80
5.2.4. Discussion 81
5.3. Chapter Summary 81
Chapter 6 Model Validation and Critical Analysis 83
6.1. Model Validation 83
6.1.1. Validation Experiment 84
6.1.2. Validation Experiment Results 86
6.1.3. Validation Experiment Data Analysis 87
6.1.4. Validation Model 88
6.1.5. Simulated Results of Validation Model 91
6.1.6. Discussion 91
6.2. Critical Analysis 93
6.2.1. Successes 93
6.2.2. Failures 93
6.2.3. Satisfying Problem Statement 94
6.2.4. Research Contributions 95
6.3. Chapter Summary 96
Chapter 7 Future Works and Conclusion 97
7.1. Possible Improvements and Future Works 98

7.1.1. Experiment 99

7.1.2. Model Development 100

7.2. Chapter Conclusion 100

References 101

Appendix A – Circuit Figures of Unified Model 106

Appendix B – Application Sample of Genetic Algorithm – Participant A 111

Appendix C - Determining Inter-Pathway Resistances using Genetic Algorithm 119

7.2.1. Model Amendments 120

7.2.2. Genetic Algorithm Pseudo-Code 121

7.2.3. Applying the Genetic Algorithm 125

LIST OF FIGURES

Figure 1 – Electrostatic Coupling between the Overhead Cables and EMG system. A) Describes the inherent electric field coupling between the EMG electrode wires and overhead power cables. B) Describes the parasitic capacitances that exist between the subject, electrode wires and power cables. 5

Figure 2 – Electrostatic Coupling between Powered Cables and the subject describing the inherent electric field coupling between the subject and power cables. Electric field direction indicates the positive half cycle. The negative half cycle will reverse the field direction. 6

Figure 3 – Describing the parasitic capacitances that exist between the subject and appliance or electrical component chassis. 6

Figure 4 – Electrostatic Coupling between Powered Cables and the Amputee subject. The subject is grasping a lamp's insulated power cable with their un amputated hand. The flow of EMI induced current conducting through the body is indicated with orange dashed lines (arrows' pointing direction is arbitrary). The negative half cycle will reverse the field direction. 7

Figure 5 – Intra-body signal propagation through the fore-arm. A simplified view of the fore-arm with three tissue-layered skin (i.e. skin, muscle and bone). 14

Figure 6 – Intra-body signal propagation through the fore-arm - Current flow paths for galvanic coupling, where primary current flow (shown in green arrows) do not affect receiver signal and the secondary current flow is the current that induces a potential difference across the receiver electrodes(shown in blue arrows). Z_{T1} represents the impedance of the primary flow path, Z_{L1} and Z_{L2} refer to the impedance of the longitudinal forward and return path of the secondary flow, respectively. Z_{T2} refers to the transverse

path of the secondary flow and *l* is the distance between transmitter and receiver electrode pairs..... 15

Figure 7 – Total body impedance as a function of applied voltage for various contact areas; dry hand-to-hand electrodes measured by Beigelmeier [44]. The image was extracted from Reilly [47] and the various curves illustrated are identified by the contact area on each hand. 16

Figure 8 – Internal Partial Impedances of the Human body. The numbers indicate the percentage of the internal impedance of the human body for the part of the body concerned, in proportion to the 'hand-to-foot' path. (Red arrows indicate skin impedances from the top layer to the nodes in the body). 18

Figure 9 – Hand grasping a flat power cable, with cable in the cross-sectional view. Blue and brown circles indicates insulation around the neutral and live wire, respectively. Human fist outline adapted from Wikimedia Commons [52]..... 23

Figure 10 – Simulated Electric Potential of a flat power cable with a floating potential boundary surrounding sheath. The legend indicates the arrow potentials in V/m. Live and neutral conductors are on the right and the left, respectively. 24

Figure 11 – Segmenting Cross-section of type flat power cable into three capacitance regions..... 24

Figure 12 – Simplified current paths in a cross-section of a flat power cable 25

Figure 13 – Simulated Capacitance C_1 and Calculated Capacitances C_2 and C_3 for Various Hand Widths Between 50 mm And 120 mm 27

Figure 14 – Capacitive-Coupling Model, where magnitudes of C_2 and C_3 are determined using Equation (4)..... 28

Figure 15 – Original Freiberger Model with human body outline..... 31

Figure 16 – Hand-to-hand Section of Freiberger Model..... 31

Figure 17 – Modification 2 of Hand-to-hand Human Body Impedance Model..... 32

Figure 18 – Modification 3 of Hand-to-hand Human Body Impedance Model..... 33

Figure 19 – Network of two series capacitors in parallel to another two series capacitors (Labelling is unrelated to the Human Body circuit model's element numbering). 35

Figure 20 – Modification 5 of Hand-to-Hand Human Body Circuit Model 36

Figure 21 – View of Anechoic Chamber from the entrance 40

Figure 22 – Sample measurement of the 230 V_{rms} power supply found in the Anechoic Chamber 41

Figure 23 – FFT of Sample measurement of the 230V_{rms} power supply found in the Anechoic Chamber 41

Figure 24 - Orientation of electrical connections to the lamp. 42

Figure 25 - High-level System Diagram of sensor employed 43

Figure 26 – EMI Measurement System Circuit Model. V_{CC} and V_{EE} are powered by the lithium batteries 46

Figure 27 – Virtual Op-Amp Settings 46

Figure 28 – PCB design for the Measurement sensor 47

Figure 29 – Pre-Experiment measurements of Body Parameter A) Measurement of placement of the electrodes (marked with blue dots) and arms span. Human body outline adapted from *Clker-Free-Vector-Images* [29]. B) Measurement region of hand width. Palm image was available through Creative Commons Licence [61] 49

Figure 30 – Hand-to-hand Impedance measurement setup. A Type P3 (2 × 0.75mm) cable was wrapped with copper tape on its end. The brown wire was connected to the copper plate on the left to the red node of the LCR meter. The black node was connected to the right copper plate with a jumper wire. 50

Figure 31 – Grasping the Hand-to-hand Impedance measurement setup 51

Figure 32 – Simplified setup for the experiment in the Anechoic Chamber. Participant does not hold any surfaces during baseline measurements. Figure of person was available through Creative Commons Licence [63] 52

Figure 33 – Two cases of the main experiment where the cable has are in two different rotational orientation in the hand. Note that the experiment had the thumb was placed on the cable for a more natural grip. Figure of fist was adapted through Creative Commons Licence [64] 53

Figure 34 – Simplified setup for the Case 1 and Case 2 experiment in the Anechoic Chamber. Figure of person was available through Creative Commons Licence [63] 54

Figure 35 – Simplified setup for the Case 3 and Case 4 experiment in the Anechoic Chamber. Figure of person was available through Creative Commons Licence [63] 55

Figure 36 – Two cases of the validation experiment where the cable has are in two different rotational orientation in the hand. Note that the experiment had the thumb was placed on the cable for a more natural grip [vii]. 55

Figure 37 – Baseline Measurements of Participant **C**. Measurements taken from the Voltage Follower Outputs for Electrode A and B; and Plug point source with 20:1 Step Down Transformer. 62

Figure 38 – Case 1 Measurement of Participant **C**. Measurements taken from the Voltage Follower Outputs for Electrode A and B; and Plug point source with 20:1 Step Down Transformer 62

Figure 39 – Case 2 Measurements of Participant **C**. Measurements taken from the Voltage Follower Outputs for Electrode A and B; and Plug point source with 20:1 Step Down Transformer 63

Figure 40 – Case 3 Measurements of Participant **C**. Measurements taken from the Voltage Follower Outputs for Electrode A and B; and Plug point source with 20:1 Step Down Transformer 64

Figure 41 – Case 4 Measurements of Participant **C**. Measurements taken from the Voltage Follower Outputs for Electrode A and B; and Plug point source with 20:1 Step Down Transformer 64

Figure 42 – Box and Whisker Diagram of Averaged Voltage Follower Output Voltages, Baseline Offset Removed, for all Four Cases. 68

Figure 43 – Unified Model of Experiment, with the Noise Source connection shown in Figure 43 73

Figure 44 – Noise Source Connection Diagram for the Four Different Cases. A) Case 1, B) Case 2, C) Case3, and D) Case 4 74

Figure 46 – Box-and-Whisker diagram describing the clustering of relative error data shown in Table 21 for the four different cases. 80

Figure 47 – Noise Source Connection Diagram for the Four Different Cases. A) Case 1, B) Case 2, C) Case3, and D) Case 4 89

Figure 48 – Unified Model of Validation Experiment, with the Noise Source connection shown in Figure 45 90

Figure 49 – Comparison of *V(Out_A) – V(Out_B)* against Z Values used in Parameter Optimization for Case 1 and Case 2, for Participant **A** – Generation 1 113

Figure 50 – Comparison of *V(Out_A) – V(Out_B)* against Z Values used in Parameter Optimization for Case 3 and Case 4, for Participant **B** – Generation 1 113

Figure 45 – Flowchart of the Pseudo-code for the desired Genetic Algorithm [66]..... 122

LIST OF TABLES

Table 1 – List of Internal Partial Impedances Percentages of the Human body, in Proportion to the 'Hand-to-Foot' Path 19

Table 2 – Permittivity and Conductivity Values for Human Body Tissue at 50 Hz and 200 Hz [50], ... 21

Table 3 – Simulated Capacitances for Various Hand widths between 50 mm and 120 mm 26

Table 4 – Error on Capacitance values obtained with Linear Relationship equations (3) and (4) 28

Table 5 – Factor adjusted percentages of Body Areas mentioned in Freiberger Model to result in a 100% Hand-to-Hand Impedance 30

Table 6 – Defining the Regions for UArmA, UArmAB and UArmB 37

Table 7 –Percentages of Body Segment Impedances after Modification 4 38

Table 8 – Specific Requirements for flat, two-core cable 42

Table 9 – Comparison of various Op-Amps Characteristics. Green fill indicates Best Performance and Orange fill indicates Poorest Performance 45

Table 10 – Ranges of Non-Amputee Participant sample set 56

Table 11 – Participant Parameter Measurements recorded off Non-Amputee Participants 57

Table 12 – Condensed Table of Non-Amputee Baseline Measurements for Main Experiment 59

Table 13 – Condensed Table of Non-Amputee Case 1 and Case 2 Main Measurements of the Experiment. 59

Table 14 – Condensed Table of Non-Amputee Case 3 and Case 4 Validation Measurements of the Experiment. 60

Table 15 – Participant **C's** Parameter Measurements recorded from (sourced from Table 11). 60

Table 16 – Summary of Measurements Recorded from Participant C 61

Table 17 – Analysis of Output Voltages Difference between Electrodes for all Four Cases 66

Table 18 – Averaged Output Voltages between Electrodes for all Four Cases 67

Table 19 – Analysis of Averaged Voltage Follower Output Voltages, Baseline Offset Removed, for all Four Cases. Shaded Values indicate a less than ±5% difference between the median and average measurements 67

Table 20 – Participant Parameters and the' Naturally Selected' Parameters *Z*, *Y*, *X*, *W* and *V* 77

Table 21 – Comparison and Error Calculation of Averaged Output Voltages between Experiment and Simulation 79

Table 22 – Comparison of $V(IA_Input+) - V(IA_Input-)$ between from the Experiment and the Simulation measurements 81

Table 23 – Clustering of Parameters *Z*, *Y*, *X*, *W* and *V* in Participants 84

Table 24 – Participant Parameter Measurements recorded off Non-Amputee Participants 86

Table 25 – Condensed Table of Non-Amputee Baseline Measurements for Validation Experiment 86

Table 26 – Condensed Table of Non-Amputee Case 1 and Case 2 Measurements for Validation Experiment 87

Table 27 – Condensed Table of Non-Amputee Case 3 and Case 4 Measurements for Validation Experiment 87

Table 28 – Validation Experiment: Averaged Output Voltages between Electrodes for all Four Cases 87

Table 29 – Validation Experiment: Analysis of Averaged Voltage Follower Output Voltages, Baseline Offset Removed, for all Four Cases. 88

Table 30 – Comparison and Error Calculation of Averaged Output Voltages between Validation Experiment and Simulation 92

Table 31 – Extract of Table 21: Comparison and Error Calculation of Averaged Output Voltages between Experiment and Simulation 92

Table 30 – Desired Average Output voltages that the Model needs to Optimize to (values obtained from Table 19) 112

Table 31 – Generation 2 − Top 10 Combinations of Variables *Z*, *Y* and *X* that produced Lowest Relative Error for Main Experiment and meet Natural selection requirements. 114

Table 32 – Generation 2 − Top 10 Combinations of Variables *Z*, *Y* and *X* that produced Lowest Relative Error for Validation Experiment and meet Natural selection requirements 115

Table 33 – Generation 3 − Top 10 Combinations of Variables *Z*, *Y* and *X* that produced Lowest Relative Error for Main Experiment and meet Natural selection requirements. 116

Table 34 – Generation 3 − Top 10 Combinations of Variables *Z*, *Y* and *X* that produced Lowest Relative Error for Validation Experiment and meet Natural selection requirements 117

NOMENCLATURE

AC	Alternating Current
CAD	Computer-Aided Design
CC	Capacitively-Coupled
CC-EMI	Capacitively-Coupled Electromagnetic Interference
CMR	Common Mode Rejection
CMRR	Common Mode Rejection Ratio
DB board	Distribution Box Board
DC	Direct Current
DSP	Digital Signal Processing
EMG	Electromyography
EMI	Electromagnetic Interference
FEM	Finite Element Modelling
H2H	Hand-to-Hand
HREC	Human Research Ethics Council
HV	High Voltage
IEC	International Electrotechnical Commission
LCR	Inductor, Capacitor, Resistor
MRI	Magnetic Resonance Imaging
MU	Motor Units

MUAP	Motor Unit Action Potential
Op-amp	Operational Amplifier
PCB	Printed Circuit Board
PVC	Poly-Vinyl Chloride
SOIC	Small outline integrated circuit
SNR	Signal-to-Noise Ratio
SPICE	Simulation Program with Integrated Circuit Emphasis

Chapter 1

INTRODUCTION

Surface Electromyography (EMG) is a common, non-invasive medical procedure used to record muscle signals for prosthetic devices. The sensor used in this procedure can easily amplify millivolt signals but have the disadvantage of being corrupted by a variety of external electrical signals [1]. Electromagnetic Interference (EMI) at power-line frequency is known to be particularly troublesome. In literature, there are several techniques used to deal with EMI, such as Common Mode Rejection (CMR) [2], active and passive shielding [3]–[5], analogue filters [6] [7], and Digital Signal Processing (DSP) techniques [8]–[16].

Most EMG sensors use Instrumentation Amplifiers (IA) to provide CMR of EMI. They are recommended to have a Common Mode Rejection Ratio (CMRR) greater than 80 dB and result in a noise floor of 2 μV_{RMS} in the 20 Hz and 500 Hz frequency band [17]. However, one can only confidently specify a CMRR if the actual magnitude of the EMI is known. To determine this EMI at the input positions of the EMG sensors, empirical data and/or model projection of the current induced by EMI flowing through the body, from the source to the sensor inputs, is required.

Finite Element Modelling (FEM) methods can provide this information, but at the cost of accessibility and time, which is unfeasible for evaluating multiple people and/or scenarios [18] [19]. More accessible methods that can model EMI

magnitudes as it propagates through the body and the resulting interference at the site of EMG measurement are unknown.

1.1. Context to Research Carried Out

A missing limb or a loss of a limb can occur congenitally or from the amputation of a severely diseased, injured or dysfunctional limb [20], [21]. This limb loss can affect the amputee's mobility, psychological well-being, quality of life, socialization, and employability [20]. Prosthetics are used to substitute for the missing limb section. Most mechanical prosthetics have one degree of freedom which results in limited movement capabilities. Over the past decade, there has been a shift towards EMG-controlled hand prosthetics from mechanical ones. This shift is because EMG-controlled prosthetic hand offer multiple movements or gesture control through the use of multiple EMG inputs and modern control systems.

1.2. Electromyography

EMG, defined by De Luca [17], "*is the discipline that deals with the detection, analysis and use of the electrical signals that emanate from contracting muscles*". However, this term refers to the act of achieving a graphical representation of the signal, which was more prevalent before the computer age. With the ability to store data digitally, the more appropriate term to define electrical signals emanating from muscles is 'myoelectric' signals, though the term EMG is still commonly used [22].

The current flow generated by the ionic chemical flow across the muscle fibres' membranes is the source of EMG signals. The chemical changes result in the contractions of muscle fibres and depends on the degree of stimulation. Muscle fibres are grouped into Motor Units (MU) and share a common motor neuron. The pulse voltages produced by the MUs are called Motor Unit Action Potentials (MUAP). These are the most basic signal component into which an EMG signal can be separated into.

The frequency of EMG signals ranges between 2 Hz and 500 Hz [23] and the dominant frequencies are between 20 Hz and 150 Hz, depending on the MU's density, the stimulation intensity and/or the stimulation duration [1], [24]. Smaller muscle like the Flexor Carpi Radialis (the muscle that controls the wrist) mainly emits signals at lower frequencies at 55 Hz – 95 Hz due to smaller set of MU. Larger muscle like the Biceps Femoris mainly emits higher frequencies at 155 Hz – 195 Hz because of a larger set of MU [25]. The myoelectric voltages are known to range between 10 μV and 10 mV, however, it is expected that maximum myoelectric voltage for amputated muscles to not peak above 1 mV because a portion of the MU has been lost or shortened [24], [26]. Additionally, intensive muscle stimulation over long durations results in a reduction in the muscle's characteristic frequencies and amplitude because the muscle fibres become fatigued. This is called muscle fatigue [1].

The overlap in the characteristic muscle frequency and the frequency of various electrical noise sources in the EMG measurement of amputated and/fatigued muscles may lead to the poor performance of an EMG-controlled prosthetic.

1.3. Noise in EMG Sensors

Due to the small amplitude nature of EMG signals and a characteristic frequency range of a few hundred Hz, the EMG sensors are required to be sensitive to changes in signal voltages across the required frequency range.

The use of EMG-controlled prosthetics in environments populated by electrically powered devices such as domestic homes and offices results in the challenge of noise interference. Several noise sources are present in the EMG characteristic frequency range of 10 Hz to 1 000 Hz, which deform or drown the EMG signal measurements. These noise sources are:

- Electrode Noise,
- Movement Artefact Noise,
- Electromagnetic Interference (EMI) Noise,

- Cross-Talk Noise, and
- Internal Noise.

Clancy et. al. [27], extensively reviews the above-mentioned noises. EMI is the most common source of noise in EMG measurements, and it is found almost everywhere.

1.4. Electromagnetic Interference (EMI) noise

Electrified spaces, such as homes and offices, contain wired electrical equipment. Current flowing through cables generates electromagnetic waves which are regarded as EMI. Continuous EMI noise sources in the EMG frequency bandwidth below 1 kHz are from the powerlines (at 50/60 Hz), power supplies and their associated harmonics. Impulse EMI noise sources can be from switching of heavy load appliances, electrostatic discharges and lightning. The human body is largely a conductive composite, and the EMI noise can either be capacitively or inductively coupled to the human body [27]. Inductively coupled EMI is taken care of by using shielding techniques but increases the exposure to Capacitively-Coupled (CC) EMI [3]–[5].

1.4.1. Capacitively-Coupled Electromagnetic Interference (CC-EMI)

CC involves charge movement from higher electrostatic potential surfaces to lower potential surfaces. Figure 1 A show a diagram of an individual, attached to EMG sensor probes, standing between an overhead powerline and a ground plane. The gaps between the two different levels of potentials are parasitic capacitances and result in stray charge flows from the powered cables to objects as shown in Figure 1 B [27] [28]. These potentials make the external environment influence the outcome of the EMG measurement.

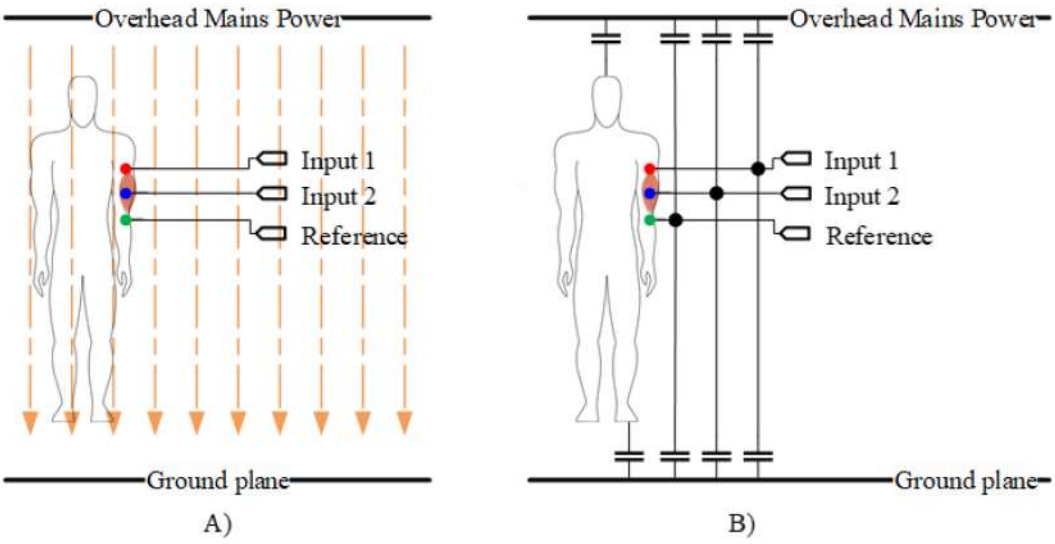


Figure 1 – Electrostatic Coupling between the Overhead Cables and EMG system. A) Describes the inherent electric field coupling between the EMG electrode wires and overhead power cables. B) Describes the parasitic capacitances that exist between the subject, electrode wires and power cables.

In Figure 1 B the individual is in a uniform electric field. In environments that may be experienced by an amputee equipped with an EMG-controlled prosthetic, the EMI is influenced by powered appliances and equipment (like electric stoves and fridges), active electrical components (like power cords, extensions and wall switches), and non-grounded metallic surfaces (like metal frame tables) [31]. This results in a non-uniform electric field unlike in the uniform electric fields shown in Figure 1 A and B.

The location of the largest concentration of stray electric fields is expected to radiate close to the source. As seen in Figure 2, where the subject's hand is in proximity to the appliance chassis or electrical component surface, the hand will provide a better conduction medium, than air. A return path for the high potential electric field from the live wire back to the neutral wire is established. Instead of parasitic capacitance occurring across the air as shown in Figure 1 B, the capacitance is across the cable insulation as shown in Figure 3. The contacts made by the hand results in a dipole interaction and a potential difference develops between the areas of the hand that are nearest to the live and neutral wires which would attribute to the EMI induced current circulating through the body.

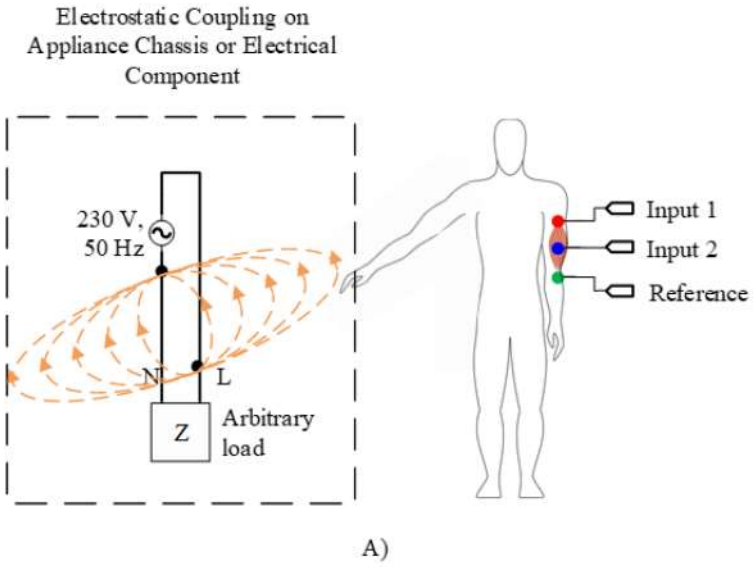


Figure 2 – Electrostatic Coupling between Powered Cables and the subject describing the inherent electric field coupling between the subject and power cables. Electric field direction indicates the positive half cycle. The negative half cycle will reverse the field direction.

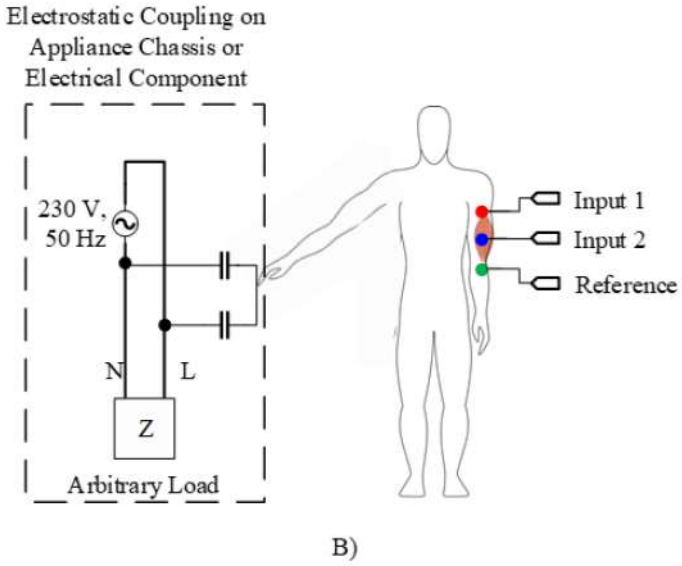


Figure 3 – Describing the parasitic capacitances that exist between the subject and appliance or electrical component chassis.

1.5. Problem Identification

Modifying the interaction found in Figure 2 and Figure 3 to the potentially common scenario with an amputee person. As shown in Figure 4, the subject has an EMG

sensor on the bicep of the amputated arm. The amputee would use their non-amputated hand for grasping a household lamp's power cable. It is expected that the current induced by EMI will be conducted through the body, from the un-amputated hand to the EMG sensor on the amputated arm. Therefore, a suitable selection of an IA with an appropriate CMRR is important. However, there is limited literature on the human body interacting with a dipole EMI source.

The conduction from the un-amputated hand to the EMG sensor is similar to the galvanic circulation experiment conducted by Wegmüller [32]. Galvanic circulation is expected to occur in the body, where the flow will begin from the grasping hand, through the torso, to the bicep-placed sensor on the amputated arm, and back to the grasping hand. This is shown by the orange arrows in Figure 4.

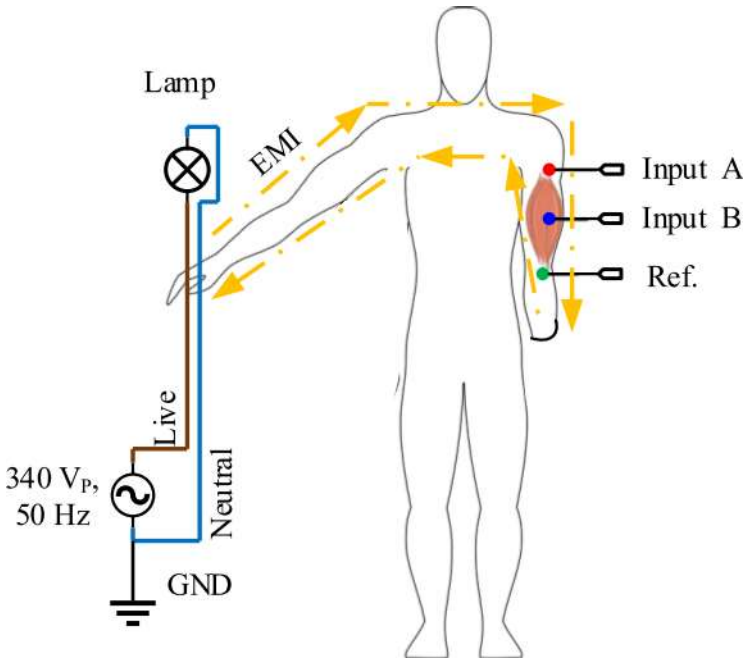


Figure 4 – Electrostatic Coupling between Powered Cables and the Amputee subject. The subject is grasping a lamp's insulated power cable with their un amputated hand. The flow of EMI induced current conducting through the body is indicated with orange dashed lines (arrows' pointing direction is arbitrary). The negative half cycle will reverse the field direction.

1.5.1. Model Requirements

The EMI measurements at various EMG electrode positions on the human body are simple voltage measurements, often using buffer amplifiers to separate the subject

from bench-powered oscilloscopes [31]. There are many different possibilities involving a subject interacting with EMI sources in a household or office environment and many more unique human body compositions. Therefore, a base model that can be adjusted for the various possibilities and the subject's unique parameters can be developed to determine the potential range of EMI magnitudes that an IA must account for. The ability to model copious quantities of possibilities with reasonable accuracy would reduce the accumulated experimentation time and resources.

Modelling the EMI due to grasping of the power cable as shown in Figure 4 requires two types of sub-models:

1. sub-model of the capacitive coupling between the source and the surface of the hand, and
2. sub-model of the electrical current flow pathways in the human body from the grasping hand to the EMG sensor

The EMI source, being a two-core power cable, is a dipole because the electrostatic potential will propagate from the live wire to the neutral wire, which is tethered to the ground in the DB board. Modelling CC can be done using a physics-based simulator, like "COMSOL Metaphysics".

The human body model will need sufficient parameters to uniquely describe the subject. Enough nodes are also needed to distinguish between the positions of the EMG sensor's inputs and the CC interception points. Since the body interacts with a dipole, the EMI will galvanically circulate through the body, similarly to the experiment conducted by Wegmüller [32]. The circulation will begin from the grasping hand, through the torso, to the sensor on the amputated arm where the sensor is placed on the bicep, and back to the grasping hand.

Modelling the human body electrical pathways often occurs in two ways. The first uses FEM to model the subject and the second uses electric circuit models.

Finite Element Modelling (FEM)

FEM divides the human body's three-dimensional volume into small blocks with a certain characteristic or property [18]. FEM models can be constructed from CAD models or MRI scans. MRI scans have the benefit of being true representations of the subject however the model generated is not deformable. CAD models, being inherently deformable, allows the model to perform a motion or a gesture.

Though FEM models may produce high-resolution data, the use of MRI as a source of data has several shortcomings. MRIs are expensive to run and take a long time to acquire complete data [19]. Highly detailed or high-resolution models also require high-performance computing hardware to process the circuit analysis which adds to the processing cost. Open-Source models are available online from several sources; however, most models require procurement [18].

Electric Circuit Human Body modelling

The second method is to model the human body as an electric circuit which is simpler and easier to compute. These models are often used to simulate the HV electrocution of subjects due to lightning or coupling to HV power lines, but they have not yet been implemented for EMG measurements. The circuit model can also be adjusted for different scenarios as well as specific human body parameters.

1.5.2. Research Question

As explained before, electrically modelling multiple human bodies using circuit models is more viable to practice than using FEM due to accessibility reasons. The unavailability of a human body electric circuit model to model dipole-sourced EMI in EMG-sensors, lead to the following research question:

"What is the human body electric circuit model for the prediction of EMI due to a dipole capacitively-coupled source, given the following conditions?"

- The subjects are non-amputees that have right-handed dominancy,
- The EMI sensor is placed on the right arm's bicep of the subject,
- The subjects are grasping a flat, two-core power cable used for lamp applications, to induce EMI currents in the body
- The lamp will be powered by 230 V_{RMS} (330 V_{Peak}), 50 Hz, and
- The subjects are measured in a controlled environment.

Constraints

The limited accessibility to research participants resulted in the following constraints:

- No access to amputee subjects. Therefore, modelling of non-amputee subjects was carried out, and
- No dominant left-handed subjects were evaluated due to their low prevalence. Therefore, modelling was conducted only on dominant right-handed participants.

1.5.3. Research Contributions

The objective of this research is to develop a model that can determine the noise voltages induced by EMI, at the inputs of the EMG sensor that are placed on the upper limb, using empirical data. This model would be used to predict the voltages induced by the EMI for an alternate but similar scenario. By achieving this objective, some contributions made to this field of research are:

- Possible utilization or modification of the existing electric circuit model of the human body.
- Providing an experiment method which can be used to examine the flow of EMI interference that is due to near-field or capacitive coupling with sources. This method was demonstrated for the events where the subject's measurements are not ground or common-node referenced to a non-foot region of the human body.

- Results of the experiment may provide useful empirical data to determine the required CMRR specification for the sensor. Usually this is approximated EMI noise “roof” value.
- Likewise, to the empirical EMI measurements, CMRR can be determined using the model projections of scenarios similar to the base scenario.

1.6. Chapter Summary

This chapter has introduced the possibility of problems due to the impact of CC-EMI on EMG-controlled prosthetics. Upper limb amputees seek these EMG-controlled prosthetics to regain mobility and independence. But the EMG sensors used to operate the prosthetic have CMRR that are not specified according to empirical data or model projections. Therefore, when the prosthetic user is performing a daily task that introduces higher than normal EMI noise conditions for the sensor, the user may have difficulty in operating the prosthetic using amputated or weaker arm muscles. This circumstance is because the EMG signal’s characteristic frequency band overlaps with that of the EMI’s frequency band.

In particular, the purpose of this research is directed towards modelling the magnitude of the CC-EMI, at 50 Hz, that conducts through the human body and could interfere with the Bicep EMG measurements. To be able to model the magnitude of the EMI, it is required that a model of the human body, as well as the model of the capacitive coupling, be developed.

Achieving a functioning electrical model of the human body that accounts for the current flow from one hand to the other will potentially reduce the time and resources required to capture EMI magnitudes found when an EMG-user is interacting with the various EMI sources found in homes or offices, and thus a CMRR can be prescribed.

The research requires the understanding and modelling of electric fields and parasitic capacitances in homes and office space, the electrical properties of human tissue and the human body as an electric circuit. Chapter 2 provides some

background knowledge on the human body electrical models and electrical nature of human tissue.

Chapter 3 documents the theoretical development of the capacitive-coupling and the human body circuit model.

In Chapter 4 the experimentation and the measurement results are discussed.

In Chapter 5, the final model derived from the sub-models discussed in Chapter 3, and the parameters recorded in Chapter 4 is presented.

In Chapter 6, model validation is conducted and research work is critically analysed. Potential future works are also discussed.

The research work is concluded in Chapter 7.

Chapter 2

HUMAN BODY ELECTRIC CIRCUIT MODELS & HUMAN TISSUE ELECTRICAL CHARACTERISTICS

This chapter examines the literature on galvanic circulation, human body electric circuit models and human tissue electrical characteristics. The magnitudes of body impedance depend on several factors such as current path, touch voltage, duration of current flow, frequency, degree of moisture of the skin, surface area of contact, the pressure exerted and temperature. [33], [34]. The Freiberger Human Body model [35] which does account for several of the factors is discussed in this chapter.

2.1. Galvanic Circulation

Wegmüller [32] attempted to describe the portions of the human body as a signal propagation mediums for Intra-body Communication. Considering the areas of the body with simple anatomical structures like the arms and legs. The modelling of the geometrical and physical properties was approximated by three types of tissue:

skin, muscle, and bone. This is shown in Figure 5. experimental setup was described as being similar to electrical impedance tomography [36]. Electrodes that were attached to a low-amplitude current source were placed on the lower part of the subject's forearm and detection electrodes were attached to the upper part of the forearm.

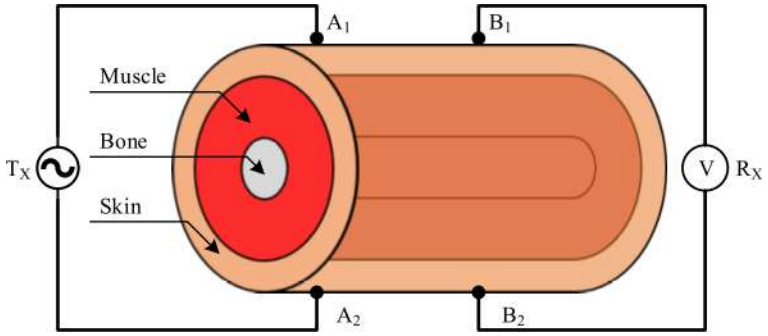


Figure 5 – Intra-body signal propagation through the fore-arm. A simplified view of the fore-arm with three tissue-layered skin (i.e. skin, muscle and bone).

However, to describe the galvanic current flow between the transmission electrodes and the receiver electrodes. Kibret et al. describes the processes better in a graphical form and this is shown in Figure 6. In this figure, there are two groups of currents flowing between the electrodes. The primary flow occurs between the transmission nodes and it can be considered the transverse path. The secondary flow moves laterally across the limb and is intercepted by the receiver electrodes which measures across second transverse path and it would be a fraction of the input voltage [37]. However, this diagram is for a single, homogenous medium and will differ when a multi-medium model is developed.

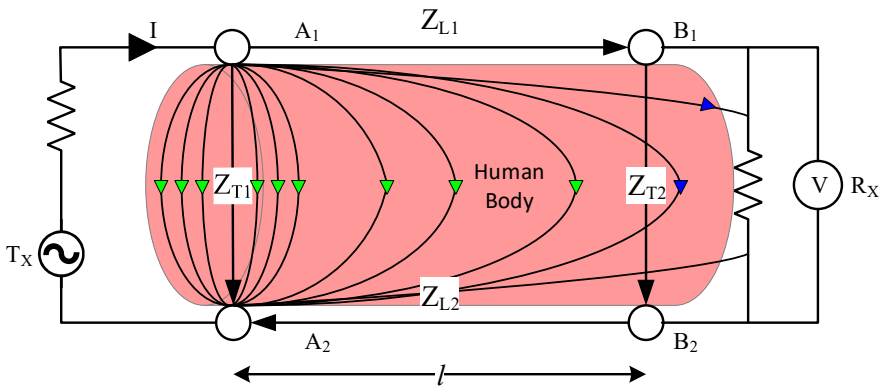


Figure 6 – Intra-body signal propagation through the fore-arm - Current flow paths for galvanic coupling, where primary current flow (shown in green arrows) do not affect receiver signal and the secondary current flow is the current that induces a potential difference across the receiver electrodes(shown in blue arrows). Z_{T1} represents the impedance of the primary flow path, Z_{L1} and Z_{L2} refer to the impedance of the longitudinal forward and return path of the secondary flow, respectively. Z_{T2} refers to the transverse path of the secondary flow and *l* is the distance between transmitter and receiver electrode pairs.

2.1.1. Discussion

Current research into modelling CC-EMI on the human body is limited to scenarios with overhead powerlines and its effect in electrocardiography measurements [38]–[40]. Haberman [31] may have touched on proximity CC-EMI with the experiment involving contact with a light switch. These works all reduced the human body component of the model, between the electrodes, to arbitrary star or delta triple resistor network or a potential divider pair.

Apart from the Freiberger model, to be discussed, human body circuit models have been used to simulate the lightning or electrostatic discharge electrocution of persons. These models are “stick-figure” human body impedance models and are described in Andrews [41] and Sutherland [42]. However, these do not support or cannot be modified to support galvanic circulation.

Galvanic circulation is considered an important concept in the developed model. Like the current propagation in Figure 6, the current propagation in the CC-EMI H2H Human Body model will also circulate, however, across a larger transverse path, i.e., from one hand to the other and with more nodes.

Adapting Figure 4 to describe the EMI coupling and propagation like the processes occurring in Figure 6, the developed model will break up into three sub-models. The transmission source containing the EMI source and the CC, the transmission medium consisting of the human body model, and the receiver part consisting of the measurement system. The developed human body model will essentially perform as a two-port network, where two terminal inputs will interact with the CC model and a three terminal output will connect to the EMI measurement sensor.

2.2. Human Body Impedance

Biegelmeier [43]–[45] conducted experiments showing the relationship between dry Hand-to-Hand (abbreviated to "H2H") impedance and applied AC voltage for various hand contact areas between 1 mm^2 and 8200 mm^2. It was found that at 25 V, the H2H impedance was inversely proportional to the contact area. The experiment results are shown in Figure 7 [46].

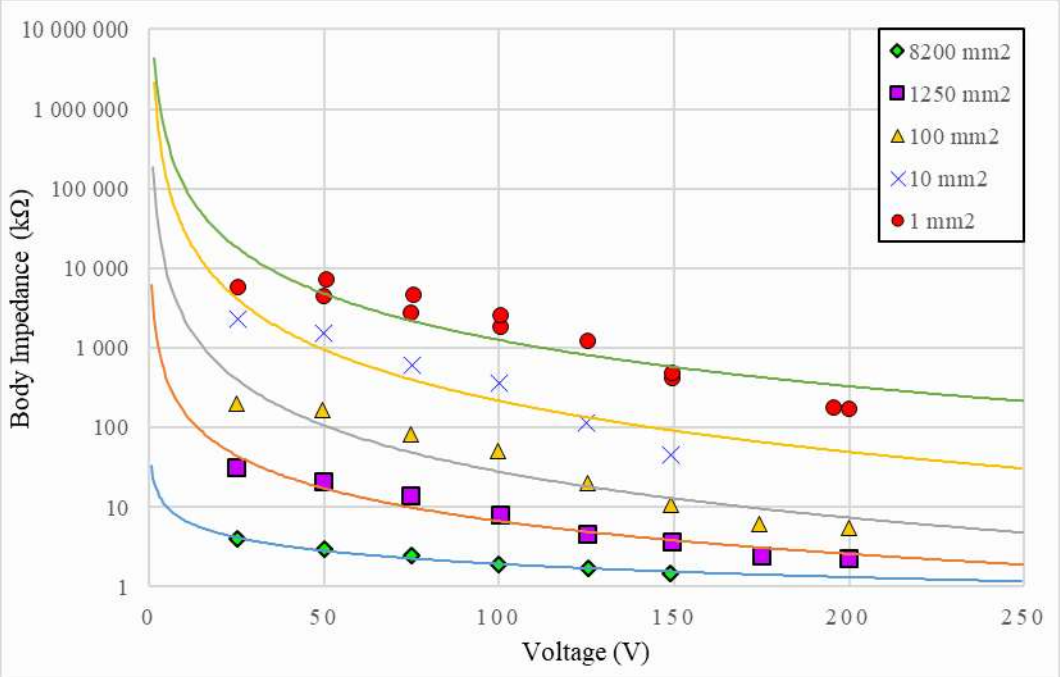


Figure 7 – Total body impedance as a function of applied voltage for various contact areas; dry hand-to-hand electrodes measured by Beigelmeier [44]. The image was extracted from Reilly [47] and the various curves illustrated are identified by the contact area on each hand.

2.2.1. Freiberger Human Body Model [35]

Over 80 years ago, Freiberger [35] determined the impedance contribution of different segments of the body and the impedance contributions of the skin in different areas of the body. Figure 8 depicts the distribution of body impedance for various current paths. The numbers indicate internal impedance for various electrode placements as a percentage of the total hand-to-foot impedance body. This model was also adopted and is easily accessible in the International Electrotechnical Commission (IEC) technical standard TS 60479-1 [33], [34]

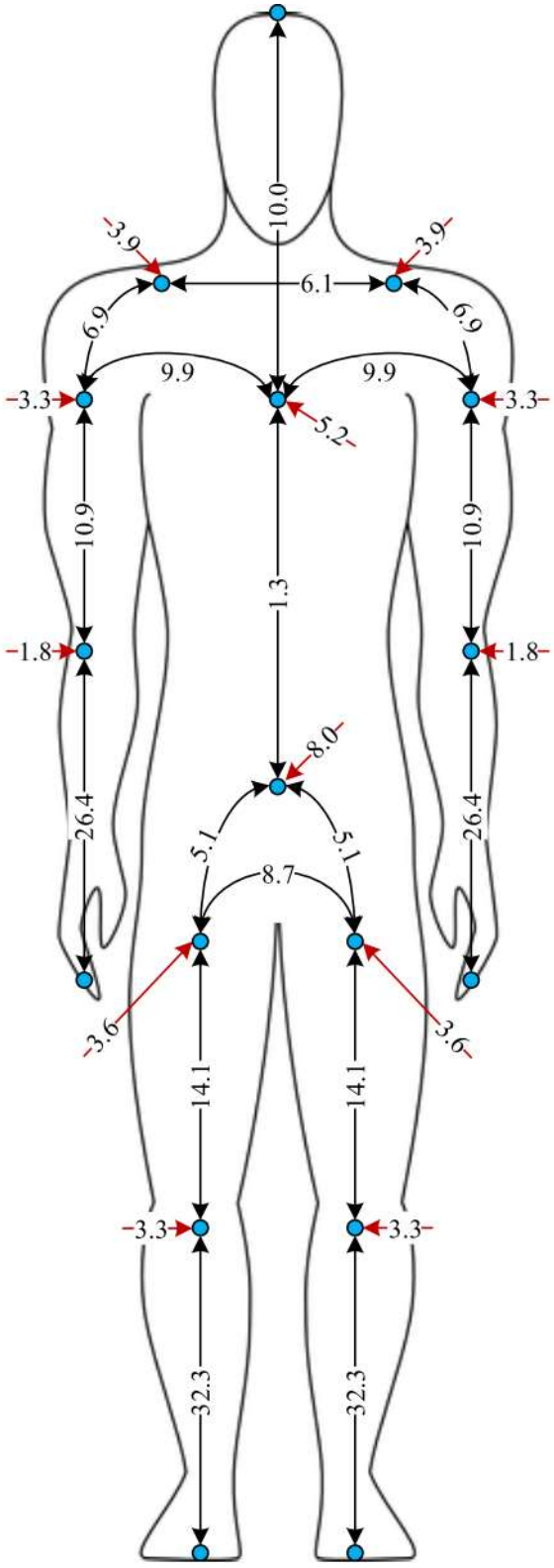


Figure 8 – Internal Partial Impedances of the Human body. The numbers indicate the percentage of the internal impedance of the human body for the part of the body concerned, in proportion to the 'hand-to-foot' path. (Red arrows indicate skin impedances from the top layer to the nodes in the body). [i]

Table 1 below, derived from Figure 8 lists the impedance contribution for each body section and different skin contact areas. The total of 100 % 'hand-to-foot' path body impedance does not include the outer skin impedance. Reilly [46] described that 50% of the internal impedance for hand-to-hand or hand-to-foot contacts resides in the extremities, i.e., wrists or ankles, and is due to the prevalence of poorer conducting bone and ligament. Reilly suggests that the impedance distribution in Figure 8 is consistent with the investigations of Taylor [48], who used high-voltage capacitive discharges on living people.

TABLE 1 – LIST OF INTERNAL PARTIAL IMPEDANCES PERCENTAGES OF THE HUMAN BODY, IN PROPORTION TO THE 'HAND-TO-FOOT' PATH

Body Part Areas	Percentage
Head to heart	10
Heart to navel	1.3
Navel to Upper leg	5.1
Upper Leg	14.1
Lower Leg	32.3
Lower Arm	26.4
Upper Arm	10.9
Deltoid	6.9
Shoulder to Shoulder	6.1
Upper Arm to heart	9.9
Waist	8.7
Skin Areas	Percentage
Lower Arm	1.8
Upper Arm	3.3
Shoulder	3.9
Heart	5.2
Navel	8
Upper Leg	3.6
Lower Leg	3.3

2.2.2. Discussion

The Freiberger model is an appropriate foundation for developing the human body electrical circuit model based on dipole inputs because the body is separated into similar characteristic segments, like the upper arm, lower arm, upper leg, etc. The benefit of segmentation by percentages is that each iteration of the model is unique to the subject's hand-to-hand or hand-to-foot impedances. The model also offers

skin impedance percentages at numerous locations which allows more accuracy for the measurement site's position.

If the H2H impedance is measured with skin impedances are included, it will be 98.1 % of the hand-to-foot impedance measured below the skin surface. Therefore, this model will require a scale adjustment to make it appropriate for H2H impedance measurement matching up to 100%.

2.3. Electrical Properties of Human Tissue

To model a basic electric circuit model of the human body, one would need to know the electrical properties, i.e., permittivity ε and conductivity σ, of affected tissue such as skin, muscles, blood, and bone. Gabriel [49] mentions that there are few reliable datasets on the human body tissue for frequencies below 100 kHz because the tissue degrades due to decomposition and electric current. Reilly [46] provides an in-depth work on the dielectric properties of tissue, effects of electricity on the human body for a wide range of voltages, current and frequencies.

Gabriel et. al. [50], [51] is often referenced in literature and is currently assumed to be a reliable source of data for conductance and permittivity of human body tissue for frequencies between 10 Hz and 10 GHz. Table 2 lists the permittivity and conductivity of the human body tissue of interest [50], [51]. As shown in Table 2, tissue with high electrolyte content, like blood and muscle, have higher conductivities.

It should be noted that skin conductance can change due to sources of hydration and salinity, like perspiration. Also, subcutaneous adipose tissue or fat is less conductive than muscle. Therefore, one would expect the attenuation of signal voltage to be proportional to the quantity of fat that lies between the skin and muscle.

TABLE 2 – PERMITTIVITY AND CONDUCTIVITY VALUES FOR HUMAN BODY TISSUE AT 50 HZ AND 200 HZ [50],

Tissue	ε @ 50 Hz	ε @ 200 Hz	σ @ 50 Hz (m/S)	σ @ 200 Hz (m/S)
Blood	5.26×10^3	5.26×10^3	0.700	0.700
Muscle	1.77×10^7	3.70×10^6	0.233	0.291
Subcutaneous Adipose Tissue	4.58×10^5	6.56×10^5	4.04×10^{-2}	4.08×10^{-2}
Cortical Bone	8.87×10^3	4.79×10^3	2.01×10^{-2}	2.01×10^{-2}
Dry Skin	1.14×10^3	1.14×10^3	2.00×10^{-3}	2.00×10^{-3}

2.3.1. Assumptions

Based on Table 2, an assumption that wet tissues have negligible capacitances can be made. Therefore, if capacitance is measured off the subject, it will be attributed to the skin surface of the developed model.

2.4. Chapter Summary

In this chapter, human body electrical impedance and human body tissues characteristics are discussed. The Freiberger human body model was presented and discussed is expected to serve as a usable base for building the desired model. Human body tissues are also discussed to identify the different degrees of resistances and capacitances in the body. Making use of existing verified human body models and data will benefit the development of the desired model by reducing the difficulties and complexities of 'starting from zero.' This base model developed in the next chapter should serve to emulate the galvanic circulation as well as to provide the inputs and output interfaces for the CC model and the EMI measurement sensor.

---

[i] NOTE : In order to calculate the total body impedance Z_T for a given current path, the internal partial impedances Z_{ip} for all parts of the body of the current path have to be added as well as the impedances of the skin of the surface areas of contact. The numbers outside the body show internal portions of the impedance to be added to the total, when the current enters at that point

Chapter 3

PROPOSED MODEL

In this chapter, the sub-models that make up the CC-EMI model for EMG sensors are developed. These sub-models are the capacitive-coupling (CC) source model and the human body circuit model.

3.1. Capacitive-Coupling Source Model

The deliberate selection of grasping a flat, two-core, power cable (2×0.75 mm^2) as the source of EMI was done to reduce the complexity of the CC component in the final model. These cables have Poly Vinyl Chloride (PVC) insulation for each of their twin-cores and further surrounded by a PVC insulation sheath, forming an elliptical cross-section profile. The cables are identified by the code "H03VVH2-F".

Power cables come in various geometries and several core numbers. Therefore, the CC model used for this cable is not expected to be directly usable for other cable variations. For example, there are other two-core wire geometries used in common household and office environments. Some have circular cross-sections, and some have thinner wires. These properties affect the electric fields between the wires and therefore affect the CC induced due to grasp.

3.1.1. Conceptualising the Electric Field on the grasped Type P3 cable

As mentioned in the last chapter, the subject can become capacitive coupled to the power grid when the cable is grasped, as shown in Figure 9. This results in the tissue that is in proximity and surrounds the cable becoming a floating potential medium.



Figure 9 – Hand grasping a flat power cable, with cable in the cross-sectional view. Blue and brown circles indicates insulation around the neutral and live wire, respectively. Human fist outline adapted from Wikimedia Commons [52].

The electric potential of the flat power cable is modelled in COMSOL V5.3 and the cross-section is shown in Figure 10. The copper cylinders are 2 mm apart (from their centres), the insulation is 0.5 mm thick, and the sheath thickness is 0.6 mm [53]. The material domains which were PVC were given a relative permittivity of 4.5 [54]. The source potential is set to 330 V_{peak} and is based on the rounded-up average source voltage measured during the experimentation of 329.9 V_{peak}. The result shows that the floating potential surface was at 165 V_{peak}.

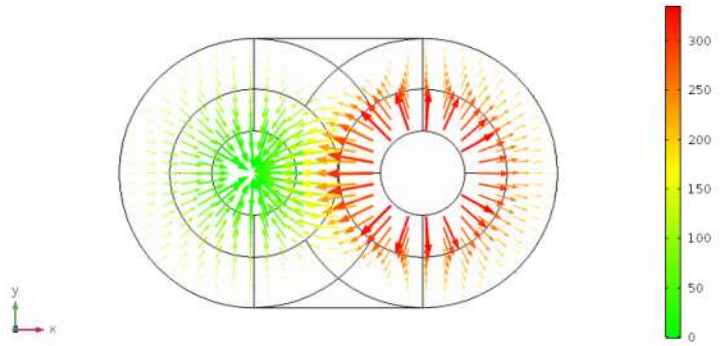


Figure 10 – Simulated Electric Potential of a flat power cable with a floating potential boundary surrounding sheath. The legend indicates the arrow potentials in V/m. Live and neutral conductors are on the right and the left, respectively.

3.1.2. Modelling Capacitance on a grasped, flat power cable

The analysis of the electric field lines in Figure 10, indicates two different travel paths. The first path propagates directly between the Live and Neutral and is concentrated in the region between the two conductors. The second path moves from the live conductor to the floating potential, conducts along the floating potential, and finally returns to the neutral conductor.

To convert the electrostatic model into an electric circuit model with minimal elements, it can be assumed that the first path can be represented as a single capacitor, C_1. And the second path can be represented as two capacitors, C_2 and C_3, each for the span across the dielectric. The regions transformed into capacitors are shown in a graphical representation in Figure 11.

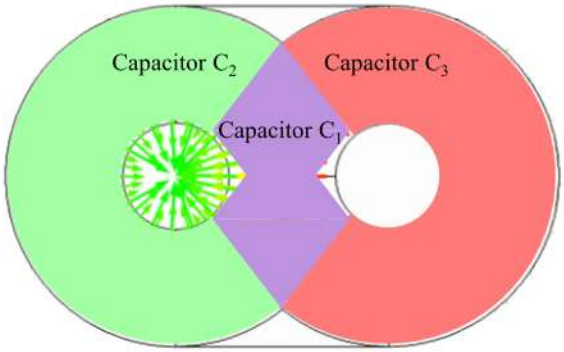


Figure 11 – Segmenting Cross-section of type flat power cable into three capacitance regions

Essentially, Figure 12 is the result of the electric circuit transformation, where two current paths are between the live and neutral conductors. The current path that connects C_2 and C_3, can follow any path along with the floating potential along the sheath and in the figure. In theory, the capacitances C_2 and C_3 have the same capacitance because the geometry of the cable is symmetrical along the tangent where the two insulators meet.

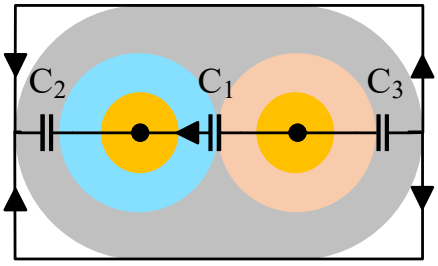


Figure 12 – Simplified current paths in a cross-section of a flat power cable

3.1.3. Capacitance on a Grasped Flat Power Cable: COMSOL modelling

COMSOL V5.3 was used to model the capacitance between Live and Neutral for the region that is grasped. COMSOL Electrostatics solver has the capability of measuring capacitances that lie between terminal voltages and ground. To use a superposition type calculation to determine the three capacitor values, two simulation geometries were conducted, where one had the sheath as a floating potential surface and the other did not.

Capacitance C_1 was determined by simulating the electrostatic field of the flat power cable without a floating potential where the charge moves directly from the live wire to the neutral wire. When simulating the electrostatic field of the flat power cable with the floating potential, the resulting capacitance measured is a combination of series connected C_2 and C_3; which is parallel connected to capacitor C_1. In this case, the charge has two paths to flow, the first is directly like the last case and the second is through the floating potential. Using the capacitor arithmetic,

Equations (1) and (2), one can deduce capacitances for C_2 and C_3 from the total capacitance when floating potential is present.

$$C_{parallel\ equiv} = C_1 + C_2 + \cdots + C_n \tag{1}$$

$$\frac{1}{C_{series\ equiv}} = \frac{1}{C_1} + \frac{1}{C_2} + \cdots + \frac{1}{C_n} \tag{2}$$

Capacitances simulated and calculated were for the hand widths between 50 mm and 100 mm at increments of 5 mm and are displayed in Table 3. The minimum width is based on the average for 6-year-old child [55], and the maximum is slightly larger than the 95th percentile for a 40-year-old male [56].

TABLE 3 – SIMULATED CAPACITANCES FOR VARIOUS HAND WIDTHS BETWEEN 50 MM AND 120 MM

Capacitance (pF)	Simulated Measurements		Calculated Values
	No Floating Potential	With Floating Potential	
Hand width (mm)	$C_{L\text{-}N} = C_1$	$C_{L\text{-}N} = C_1 + 2\times C_2$	$C_2 = C_3$
50	3.65	6.15	5.00
55	4.02	6.77	5.50
60	4.38	7.38	6.00
65	4.75	8.00	6.50
70	5.11	8.61	7.00
75	5.48	9.23	7.50
80	5.84	9.84	8.00
85	6.21	10.50	8.58
90	6.58	11.10	9.04
95	6.94	11.70	9.52
100	7.30	12.30	10.00
105	7.67	12.90	10.46
110	7.93	13.30	10.74
115	8.38	14.10	11.44
120	8.76	14.80	12.08

Figure 13 is a plot of the values found in Table 3 which also contains the trend-lines describing the linear relationship between the hand width and the Capacitances C_1, C_2 and C_3. The linear relationships are described in Equations (3) and (4) . The

relative errors between the linear Equations (3) and the simulated values are described in Table 4 , along with the corresponding impedances at 50 Hz. Most deviation errors were below 1 % except for the event with 110 mm hand width.

$$C_1 = 72.9\, pF/m \tag{3}$$

$$C_2 = C_3 = 99.8\, pF/m \tag{4}$$

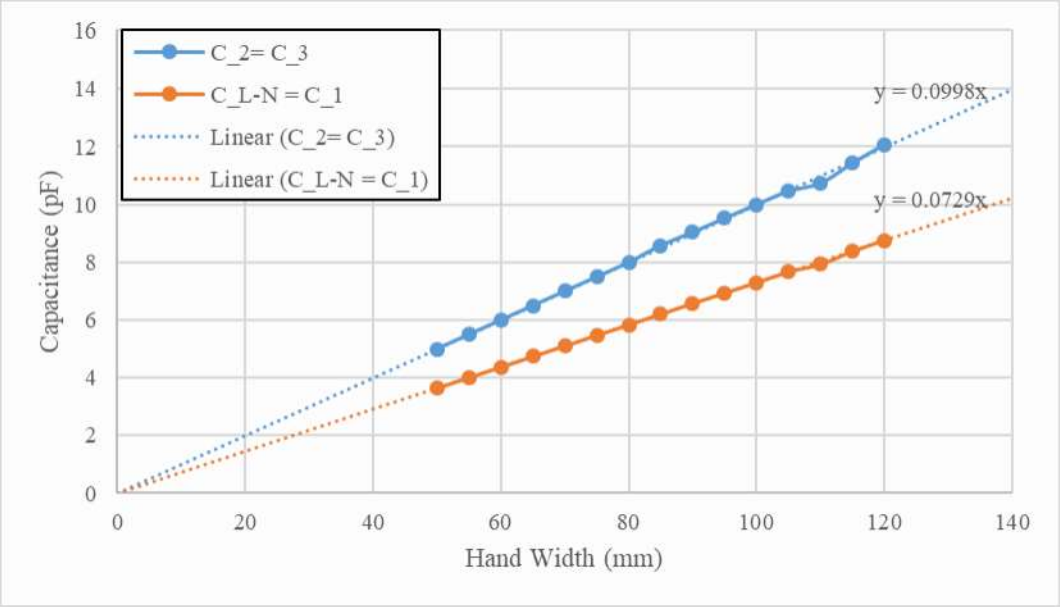


Figure 13 – Simulated Capacitance C_1 and Calculated Capacitances C_2 and C_3 for Various Hand Widths Between 50 mm And 120 mm

TABLE 4 – ERROR ON CAPACITANCE VALUES OBTAINED WITH LINEAR RELATIONSHIP EQUATIONS (3) AND (4)

	$C_{L-N} = C_1$			$C_2 = C_3$		
Hand width (mm)	Capacitance (pF)	Error %	Impedance @ 50 Hz (MΩ)	Capacitance (pF)	Error %	Impedance (MΩ)
50	3.65	0.14%	873	4.99	0.20%	638
55	4.01	0.26%	794	5.49	0.20%	580
60	4.37	0.14%	728	5.99	0.20%	532
65	4.74	0.24%	672	6.49	0.20%	491
70	5.10	0.14%	624	6.99	0.20%	456
75	5.47	0.23%	582	7.49	0.20%	425
80	5.83	0.14%	546	7.98	0.20%	399
85	6.20	0.22%	514	8.48	1.13%	375
90	6.56	0.29%	485	8.98	0.64%	354
95	6.93	0.21%	460	9.48	0.41%	336
100	7.29	0.14%	437	9.98	0.20%	319
105	7.65	0.20%	416	10.48	0.18%	304
110	8.02	1.12%	397	10.98	2.22%	290
115	8.38	0.04%	380	11.48	0.32%	277
120	8.75	0.14%	364	11.98	0.86%	266

3.1.4. Discussion

In this sub-section, the aim was to obtain an equation that estimates the coupling capacitance values (C_2 and C_3) that describe a hand grasping a flat power cable. The coupling capacitance values were determined by comparing simulation values of the use case that has a floating potential with a set of simulations that do not contain floating potentials. It can be deduced that the coupling capacitances C_2 and C_3, between the cable conductors and the subject grasping the cable, was between 4.99 pF and 11.98 pF (638 MΩ and 266 MΩ, respectively at 50 Hz), for hand widths between 50 mm and 120 mm. The CC circuit model, to be used in the final model, is shown in Figure 14.

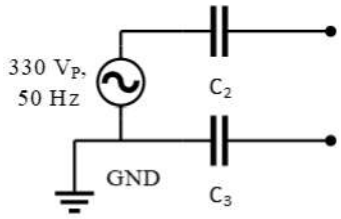


Figure 14 – Capacitive-Coupling Model, where magnitudes of C_2 and C_3 are determined using Equation (4)

3.2. Development of the Human Body Circuit Model

Using the Freiberger model as a base, several modifications are required to morph it into the desired model with the following characteristics:

- Multiple circuit loops to mimic galvanic current flow, and
- Ability to divide the length of the bicep (or any other measured muscle) to place the EMG electrodes,

To achieve the above characteristics, the below modifications to the Freiberger model were made.

3.2.1. Modification 1: Modifying Percentages of the Hand-To-Hand Impedance

The focus of this research is on upper limb measurements. Using the hand-to-leg impedance percentages in Table 1 yield 88.12 % for the H2H impedance using Equation (5). This equation was derived by calculating the impedance between the two hands of Figure 8, where the paths from the torso to the head and the torso to the legs are considered open circuits.

The H2H impedance percentage values were recalculated to make Equation (5) amount to 100% H2H impedance, including the skin impedance. This resulted in a scale-up factor of 1.135 applied to each of the impedance values and the new proportioned values are listed in Table 5 .

$$R_{H2H_0} = 2 \times \left(R_{skin_{LArm}} + R_{LArm} + R_{UArm}\right) + \left(2 \times R_{UArm_{Heart}}\right) || (2 \times R_{Deltoid} + R_{Shoulder}) \quad (5)$$

TABLE 5 – FACTOR ADJUSTED PERCENTAGES OF BODY AREAS MENTIONED IN FREIBERGER MODEL TO RESULT IN A 100% HAND-TO-HAND IMPEDANCE

Body Part Areas	Abbreviated name	Original %	New %
Head to heart	Head_heart	10	11.35
Heart to navel	Heart_navel	1.3	1.48
Navel to Upper leg	Navel_Uleg	5.1	5.79
Upper Leg	ULeg	14.1	16.00
Lower Leg	LLeg	32.3	36.65
Lower Arm	LArm	26.4	29.96
Upper Arm	UArm	10.9	12.37
Deltoid	Deltoid	6.9	7.83
Shoulder to Shoulder	Shoulders	6.1	6.92
Upper Arm to heart	UArm_heart	9.9	11.23
Waist	Waist	8.7	9.87
Skin Areas	Abbreviated name	Original %	New %
Lower Arm	skin_LArm	1.8	2.04
Upper Arm	skin_UArm	3.3	3.74

3.2.2. Modification 2: Reducing original Model Scope to Hand-to-hand Model

The Freiberger model was potentially suitable for “far-field capacitive coupling” where the person is some distance away from an EMI source and the EMI induced currents will dissipate to the ground plane via the subject’s feet. In other words, the current path flows from one extremity to another. The model was plotted in LTspice and is shown in Figure 15. Terms *Left_Hand1* and *Right_Hand1* on the extremity nodes refer to the right hand and left hand of the participant.

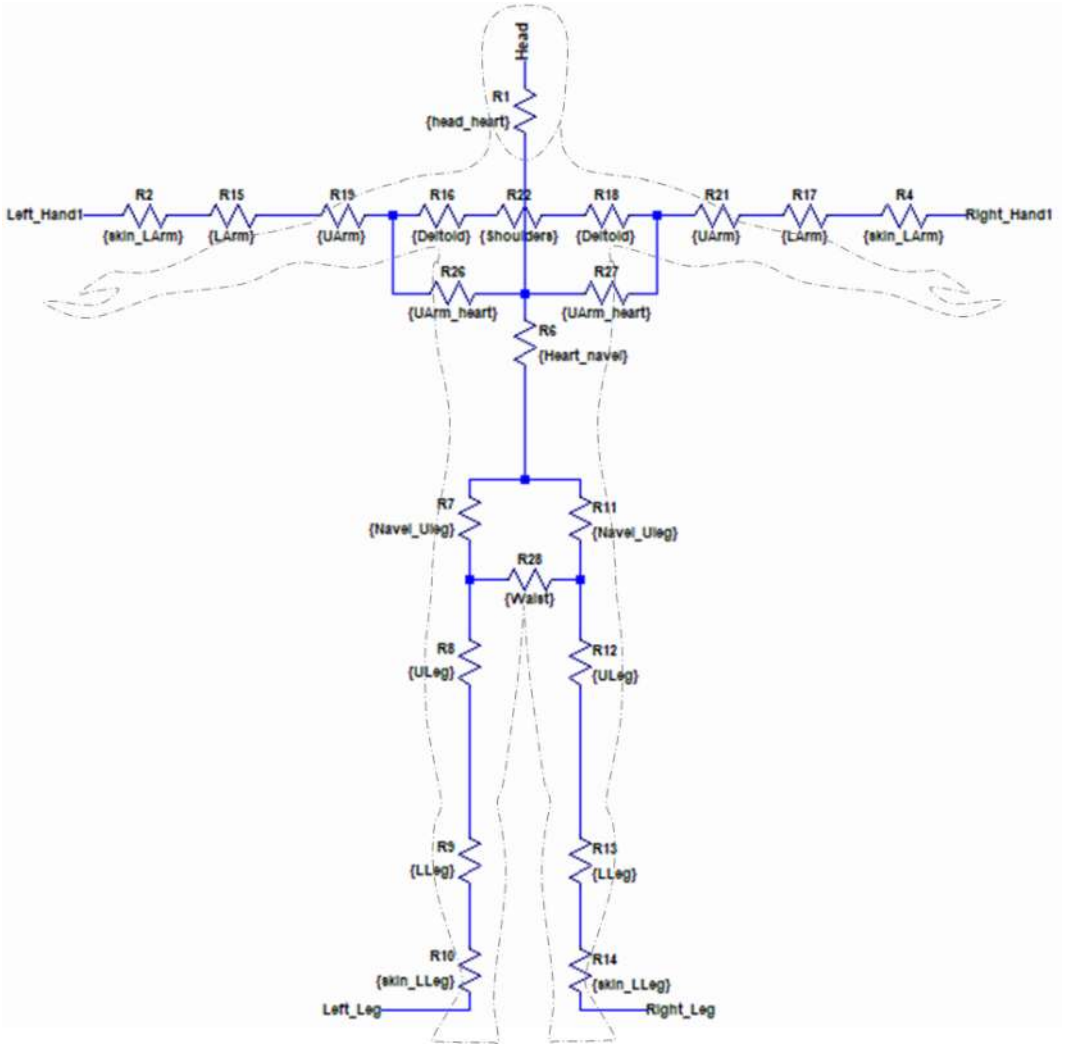


Figure 15 – Original Freiberger Model with human body outline.

Based on the values in Table 5, it is assumed that the path of least resistance between the hands does not pass through the head and legs. Therefore, the first model modification was to remove parts of the model that would have a negligible effect, which are the head and legs. The result is shown in Figure 16.

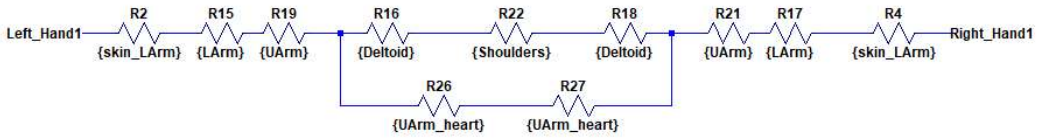


Figure 16 – Hand-to-hand Section of Freiberger Model

3.2.3. Modification 3: Introducing the 2nd Pathway using Parallel-Resistor Theory

Modification 2 simplified the original model for a H2H transmission case. Modification 3 was done to introduce the anterior and posterior electrical pathways. This modification was the next step in creating a closed loop between the noise source and the measurement site. Another reason for having separated anterior and posterior paths was because the bicep muscle is adjacent to the inner elbow and not to the elbow bone. It should be noted that the EMG sensor reference is placed above the elbow bone which implies that this separation is important.

The upper limb sections of the model were duplicated and placed in parallel to connect to the *UArm_heart* resistors, as shown in Figure 17. Since the upper limbs have two paths each, the resistance values of *skin_LArm*, *LArm* and *UArm*, need to be doubled to maintain the 100 % hand-to-hand impedance value. The resulting H2H impedance is still 100 %.

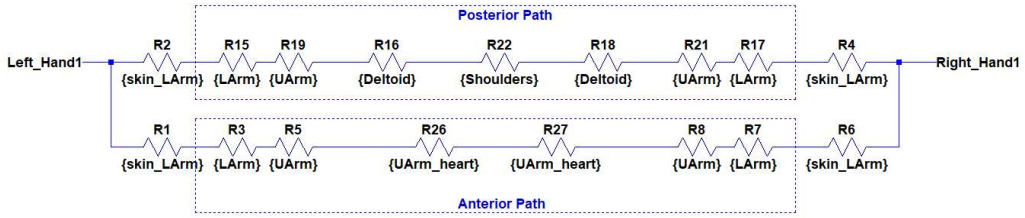


Figure 17 – Modification 2 of Hand-to-hand Human Body Impedance Model

3.2.4. Modification 4: Introducing Inter-Pathway Resistances for Multiple Galvanic Flow Paths and H2H Capacitance

This modification is to introduce resistors between the anterior and posterior paths, thus creating multiple meshes for current to circulate. Based on the literature presented in Section 2.3, it is assumed that current flow path preference is through the body tissue with the least impedance, which in this modelling case is muscle tissue. Current will enter the muscles at attachment points on the skeleton.

As shown in Figure 18 , eight resistors crossing between the anterior and posterior paths have been introduced. Ideally, these inter-pathway resistors placed between the anterior and posterior paths represent higher impedance body tissue like bone or tendon that connects opposite muscles at joints for the wrists, elbows, and shoulders. The inter-pathway resistors are positioned to join at the existing eight nodes on both arms of the Freiberger model. It is assumed that the current leakage to higher impedance tissues like bone and skin are negligible, therefore, no inter-pathway resistors partway between the upper arm or lower arm segments.

The sub-sections below describe the modifications to the inter-pathway resistances, H2H capacitance and the extremity nodes.

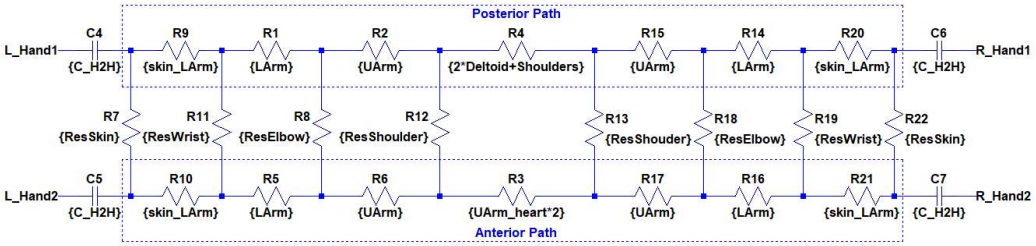


Figure 18 – Modification 3 of Hand-to-hand Human Body Impedance Model

Inter-Pathway Resistors

Assuming both arms have the same impedance composition, the four resistors, *ResSkin*, *ResWrist*, *ResElbow* and *ResShoulder*, were added in each arm circuit to represent the Stratum Corneum and the joints for the wrists, elbows, and shoulders, respectively. It should be noted that the resistor *skin_LArm* represents the resistance experienced by the current flow through the Stratum Corneum layer and into the sub-Stratum Corneum layers of the skin. And *ResSkin* represents the resistance across the skin surface. Based on the literature that states cortical bone is more conductive than dry skin, it is assumed that the magnitude of *ResSkin* must be greater than *ResWrist*.

It is known that a sizeable portion of the internal impedance for hand-to-hand contacts resides in the extremities due to the prevalence of poorer conducting bone

and ligament [46]. Subsequently, regions surrounded by a greater proportion of muscles to joint tissue will have lower resistance. It is assumed that the magnitude of *ResWrist* would be larger than *ResElbow*.

To maintain proportionality of the magnitudes of *ResSkin*, *ResWrist*, *ResElbow* and *ResShoulder* between participants, the values were derived as a factor of the Hand-to-hand resistance, R_{H2H}, magnitude resulting in Equations (6) to (10) .

$$ResSkin = Y \times R_{H2H}\ (\Omega) \tag{6}$$

$$ResWrist = X \times R_{H2H}\ (\Omega) \tag{7}$$

$$ResElbow = W \times R_{H2H}\ (\Omega) \tag{8}$$

$$ResShoulder = V \times R_{H2H}\ (\Omega) \tag{9}$$

$$ResSkin > ResWrist > ResElbow > ResShoulder \tag{10}$$

The above mentioned four resistance values are unknown and are determined in Chapter 5, Section 7.2.3.

Hand-to-Hand Capacitance (C_{H2H_0})

Capacitors with a 'C_{H2H}' capacitance magnitude were placed at the ends of *skin_LArm* to represent the capacitance due to the Stratum Corneum. Assuming the subject's H2H series capacitance was measured and stored at the value 'C_{H2H_0}'. The C_{H2H} value could be derived by converting the single capacitor magnitude to a capacitor network of two series capacitors in parallel to another two series capacitors, as shown in Figure 19. The result is that each capacitors magnitude is equal to the total capacitance of the system, C_{H2H_0}.

$$C_{H2H} = 0.5 \times C_{H2H_0} \,||\, 0.5 \times C_{H2H_0} = C_{H2H_0}$$

(11)

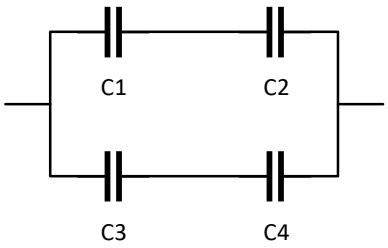


Figure 19 – Network of two series capacitors in parallel to another two series capacitors (Labelling is unrelated to the Human Body circuit model's element numbering).

Extremity Node Modification

The nodes *Left_Hand1* and *Right_Hand1* in Figure 17 were split into two nodes due to the addition of *ResSkin* in Figure 18. The naming was revised to *L_Hand1* and *L_Hand2* for the nodes on the left hand, and *R_Hand1* and *R_Hand2* for the nodes on the right hand. These nodes will be connected as the left-hand or right-hand pairs to the Noise model developed in the CC Source Model in Section 3.1.

3.2.5. Modification 5: Dividing Bicep area of Upper Arm for placement of Bipolar electrode nodes

This modification was to subdivide the right-hand side's upper arm resistor (*R15* in Figure 18) into regions separated by the bipolar electrode positions. The result shown in Figure 20 has the three resistors (*R23*, *R24* and *R25*) with the values of *UArmA*, *UArmAB* and *UArmB*, respectively. The nodes between them are labelled *Pad_A* and *Pad_B* and represent the electrode position. It should be noted that the resistance percentage values of *UArmA*, *UArmAB* and *UArmB* are proportional to the length

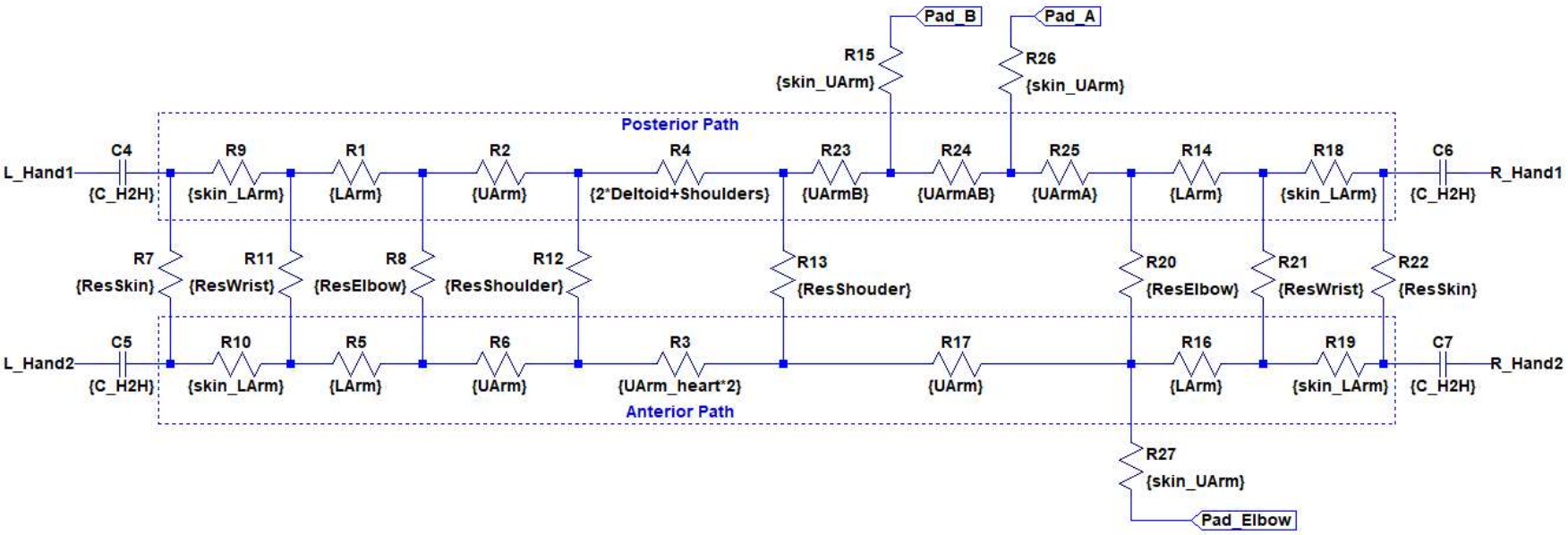


Figure 20 – Modification 5 of Hand-to-Hand Human Body Circuit Model

each region occupies of *UArm*. The regions are described in Table 6.

TABLE 6 – DEFINING THE REGIONS FOR UARMA, UARMAB AND UARMB

Parameter	Equation or Magnitude
A	Length between *Pad_A* and Elbow electrode (m)
B	Length between *Pad_B* and Shoulder bone (m)
AB	Length between the *Pad_A* and *Pad_B* centres

The percentage resistance values of *UArmA*, *UArmAB* and *UArmB* are calculated using the mathematical equations (12) to (15). Using the assumption by Wegmüller [32] that the internal resistance across the length of the upper arm was uniform. This allowed the simple subdivision described in the equations below.

$$UArm_Length = A + B + AB\ (m) \tag{12}$$

$$UArmA = A \times UArm/UArm_Length\ (\%) \tag{13}$$

$$UArmB = B \times UArm/UArm_Length\ (\%) \tag{14}$$

$$UArmAB = AB \times UArm/UArm_Length\ (\%) \tag{15}$$

3.2.6. Discussion

In this sub-section, the aim was to obtain a human body electrical circuit model that accounts for galvanic circulation using the knowledge found in the literature. The developed model made use of the Freiberger model as a base. However, the model is incomplete as there are undefined resistances, that account for current circulation between anterior and posterior paths. The human body model requires experimental data to derive unknown resistor values. The resulting body segment percentages after all the modifications are shown in Table 7.

TABLE 7 –PERCENTAGES OF BODY SEGMENT IMPEDANCES AFTER MODIFICATION 4

Body Part Areas	Abbreviated name	New Percentage
Lower Arm	LArm	59.91
Upper Arm	UArm	24.74
Deltoid	Deltoid	7.83
Shoulder to Shoulder	Shoulders	6.92
Upper Arm to heart	UArm_heart	11.23
Skin Areas	Abbreviated name	New Percentage
Lower Arm	skin_Larm	4.09
Upper Arm	skin_Uarm	7.49

3.3. Chapter Summary

In this chapter, a basic CC-circuit model was developed for the flat, two-core power cable using COMSOL electrostatic simulations, and the Human Body circuit model was developed from the literature presented in Chapter 2. The CC-circuit model was designed to provide capacitance across the insulation based on the subject's hand width. The relationship between the hand width and capacitance is linear and is represented by Equation (4).

The Human Body circuit model was developed from the Freiberger model and accounts for galvanic circulation of EMI due to a dipole source. However, the circuit is incomplete as there are abstract resistors that represent the resistance across the skin, and joints of the wrist, elbow, and shoulder. These abstract resistors currently do not have specified magnitudes and will be determined by use of experimental data.

Chapter 4

EXPERIMENTATION & RESULTS

In this chapter, the experimentation procedure and the measurement results are processed and discussed. The data obtained will be used for populating the input parameters into the combined model and optimising to proximate the output parameters in Chapter 5. The sections in this chapter will present the decisions taken on and setup of the noise source, the component selections for the measurement sensor, and the data collection procedure used during the experiment. The measurement results are processed and analysed, and a sample data set is presented.

4.1. Experimental Environment and Component Design

The designed experiment will need to provide the input data, required to characterise the participant based on their externally measureable parameters. As well as output data required to calibrate the model for improved accuracy. To re-iterate, the conditions are:

- The subjects are non-amputees that have right-handed dominancy,
- The EMI sensor is placed on the right arm's bicep of the subject,
- The subjects are grasping a flat, two-core power cable used for lamp applications, to induce EMI currents in the body.
- The lamp will be powered by 230 V_{RMS} (330 V_{Peak}), 50 Hz, and

- The measurements are done in a controlled environment.

The environment and lamp used during the experiment are discussed in Section 4.1.1 - Environment Setup. The component selection and design of the developed EMI sensor are discussed in Section 4.1.2 - Measurement System.

4.1.1. Environment Setup

The requirement for a controlled environment leads to the use of the School of Electrical and Information Engineering's Anechoic Chamber facility in the Electromagnetic Laboratory. The chamber is virtually isolated from noise sources such as power cables and telecom signals. The chamber's one 230 V_{rms}, 50 Hz plug point source will be used for powering the lamp, as well as the oscilloscope that will be recording the measurements obtained from the EMI sensor.

As shown in Figure 21 , a table was positioned in the chamber, and the lamp and the oscilloscope were placed on the table. The 230 V_{rms}, 50 Hz power source was measured via a generic, 20:1 step down transformer with a 300mA current rating.

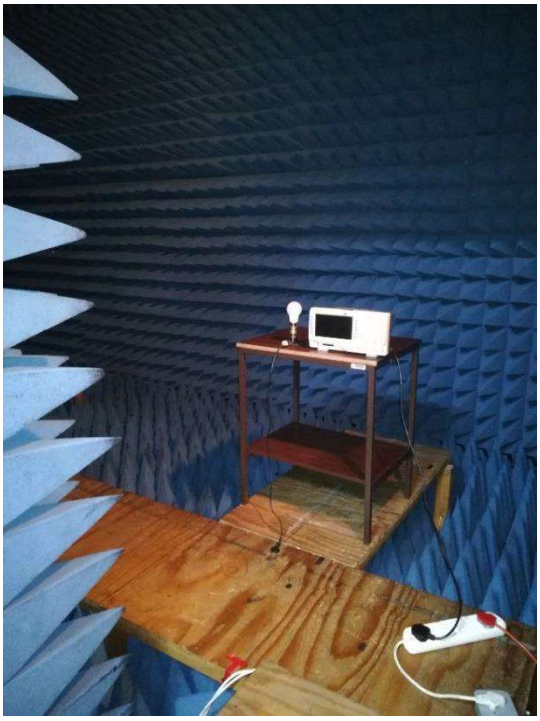


Figure 21 – View of Anechoic Chamber from the entrance

Power Supply Characteristics

The power supply was measured using the step-down transformer to isolate the oscilloscope's grounding and the measurement ground reference. The measurements were multiplied by 20 to compensate for the stepped-down voltage. The measurement sample is shown in Figure 22 , and the RMS and peak voltages were 230.7 V, and 329.84 V, respectively.

The 230 V_{rms}, 50 Hz power supply sample's frequency spectrum, with a 1 kHz filter, is shown in Figure 23, where one can see that harmonics at 150 Hz, 250 Hz, 350 Hz, 450 Hz, 550 Hz and 650 Hz are above 50 mV_p.

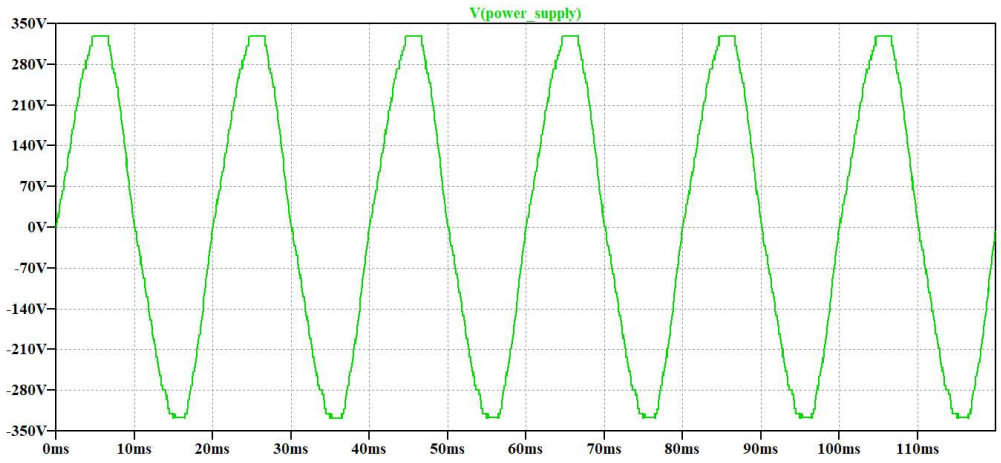


Figure 22 – Sample measurement of the 230 V_{rms} power supply found in the Anechoic Chamber

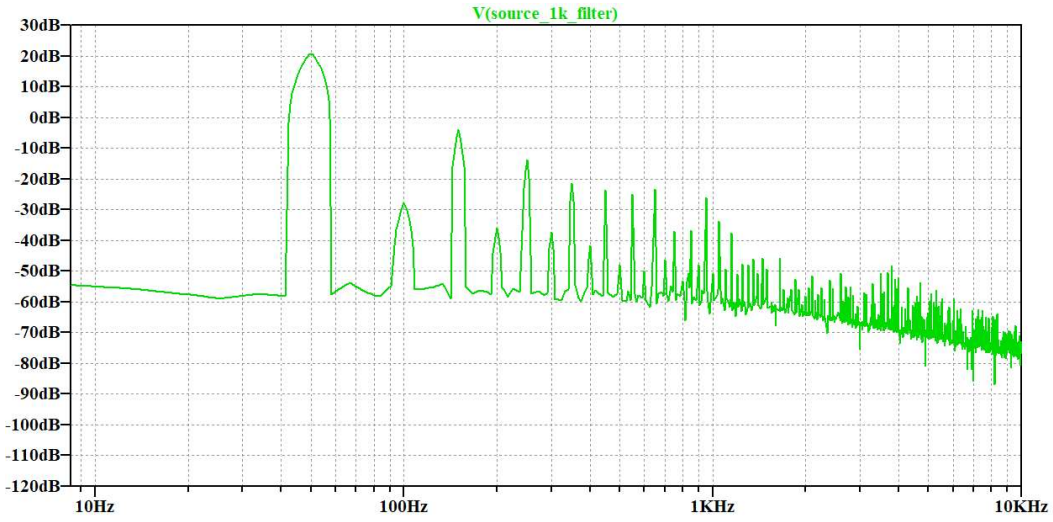


Figure 23 – FFT of Sample measurement of the 230V_{rms} power supply found in the Anechoic Chamber

Noise Source – Cable and Lamp

The cable was a 1.8 m "Aberdare 300/300V H03VVH2-F", used for electrical devices up to 3 A. The Type P3 cables dimensions are shown in Table 8 .

TABLE 8 – SPECIFIC REQUIREMENTS FOR FLAT, TWO-CORE CABLE

Number of cores and conductor size (mm^2)	Thickness of insulation (mm)		Thickness of Sheath (mm)		Overall breadth limits (mm)		Overall width limits (mm)	
	minimum	nominal	minimum	nominal	lower	upper	lower	upper
2 × 0.75	0.35	0.5	0.41	0.6	3.2	3.8	5.2	6.3

An important aspect of the lamp's cable to note was the orientation of the Live and Neutral wires. With the flat sides of the cable facing as shown in Figure 24, the Live and Neutral wires were on the left and right side, respectively. The light bulb used in the experiment was a "Eurolux G541BC", 6W, Warm White LED globe as it is the most common source of illumination in homes and offices due to its energy efficiency. It is known that LED lighting contain power regulation circuitry and are known to possess switching frequency noise, it is expected that the switching frequency will not occupy the frequencies adjacent to 50 Hz.



Figure 24 - Orientation of electrical connections to the lamp.

4.1.2. Measurement System

As shown in Figure 25, the EMI measurement system comprises of the Electrodes, the PCB-mounted Voltage Followers circuit, the Oscilloscope and the DC (Direct Current) Power Supply. The dual-rail DC power was provided by a pair of 7.2 V batteries. The recorded data was collected using the "RIGOL MSO1104Z" oscilloscope. In this subsection, the following are discussed.

- Hydrogel electrodes used and their characteristics, and
- The component selection and PCB design of the EMI sensor.

The oscilloscope will have some effect on the experiment as it is AC-powered. To reduce the effects of the any residual uncontrolled EMI within the anechoic chamber, a baseline measurement will required to acknowledge the ambient EMI on the body before interacting with the lamp cable.

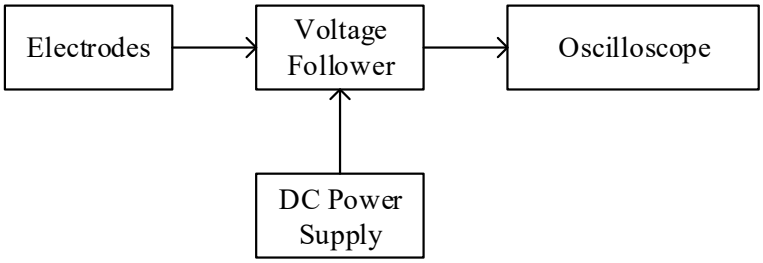


Figure 25 - High-level System Diagram of sensor employed

Hydrogel Electrodes used and Characteristics.

The hydrogel electrodes obtained for the EMI measurements were "SKINTACT FS-RG1/10 ECG Electrodes". These electrodes have dimensions of 32mm × 40 mm.

The series impedance of the hydrogel electrode pads was measured by placing two electrodes face to face and measuring the impedance between the two male press-studs using the LCR meter. The meter read 99.24 Ω and 44.02 μF for the resistance and capacitance, respectively. For simplicity, the resistance and capacitance were

rounded off to 100 Ω and 45 μF, respectively. Calculating a single electrode's impedance yielded the values of 50 Ω and 90 μF.

Voltage Follower Circuit

The op-amps TL061 ACDR, TL071BCD and TL081BCD were screened from the general-purpose op-amps section of the Texas Instruments free sample website [57]. The op-amps chosen to have the following specifications.

- a single channel, SOIC, 8-pin surface-mount packaging,
- can operate with dual-power supply, and
- has Typical Input Voltage Noise Density < 50 nV/ √Hz

The comparison between the three op-amps is displayed in Table 9. The TL071BCD and the TL081BCD specifications are similar in most categories. Though the TL071BCD is more purpose-built for low noise operation, the TL081CDR was chosen due to the shorter rise time overshooting period which should produce a more responsive circuit. It was expected that experiments would yield measureable harmonics of 50 Hz thus for requirement of the faster op-amp. However, this was not the case and therefore the TL071BCD would have been the better op-amp. It should be noted that the use of either of the listed Op-amps will provide a 1 TΩ input impedance which is larger than any known human body impedance.

TABLE 9 – COMPARISON OF VARIOUS OP-AMPS CHARACTERISTICS. GREEN FILL INDICATES BEST PERFORMANCE AND ORANGE FILL INDICATES POOREST PERFORMANCE

Parameter	TL061 ACDR [58]	TL071 BCD [59]	TL081 BCD [60]
Optimization	Low Power	Low Noise	General
Input Voltage Offset Range (mV)	3 to 7.5	2 to 5	3 to 5
Input Offset Current Range (nA)	0.005 to 3	0.005 to 2	0.005 to 10
Input Bias Current Range (nA)	0.03 to 7	0.05 to 7	0.03 to 7
Typ. Peak Output Voltage Swing (V)	± (V_{CC} - 1.5)		
Large Signal Differential Voltage Amplification (V/mV)	6	200	200
Unity Gain Bandwidth (MHz)	1	3	3
Input resistance (Ω)	10^{12}		
Max CMRR @ 1 kHz (dB)	86	100	86
Slew Rate (V/uS)	3.5	13	13
Input Voltage Noise @ 1 kHz (nV/√Hz)	42	18	18
Rise-time overshoot factor (µs)	0.2	0.1	0.05
Dual Power Supply Range (V)	± 5 to ± 15		
Max Supply Current per channel (mA)	0.25	2.5	2.8
Temperature Range (°C)	0 to +70		

Figure 26 shows the circuit diagram of the electrical components described in Figure 25. The measurement circuit made use of a virtual op-amp and the settings used in the virtual Op-amp is shown in Figure 27 and are based on the parameters obtained for the TL081BCD datasheet. The hydrogel pads impedances were also added in series to Voltage Follower inputs.

To create a floating reference potential for the measurement sensor, a 100 MΩ resistor was placed between the DC ground node and ground and was used to represent the air gap between the participant and the ground plane. The value of 100 MΩ was chosen from a range between 25 MΩ and 1.68 GΩ which are respectively ground separation and power line separation impedances of a person standing in a middle of a room obtained from Serrano et. al. [39].

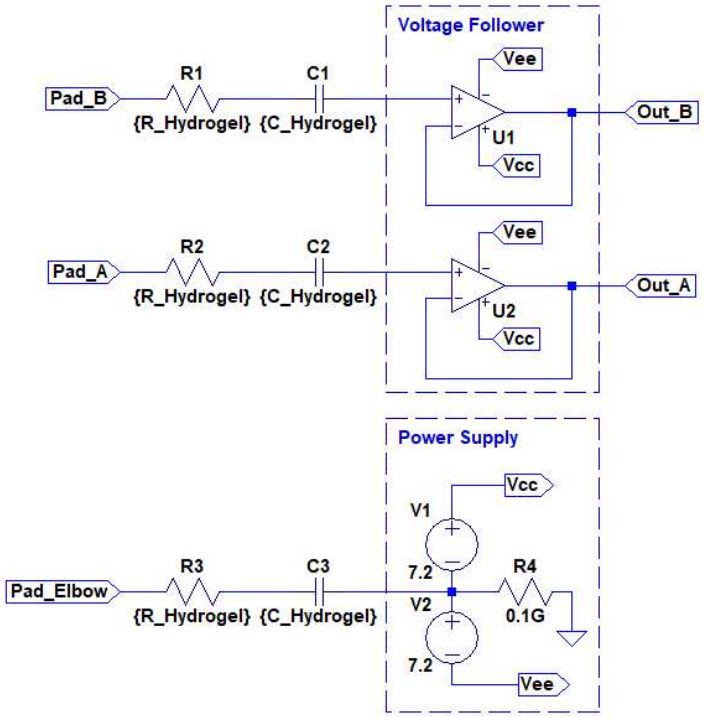


Figure 26 – EMI Measurement System Circuit Model. V_{CC} and V_{EE} are powered by the lithium batteries

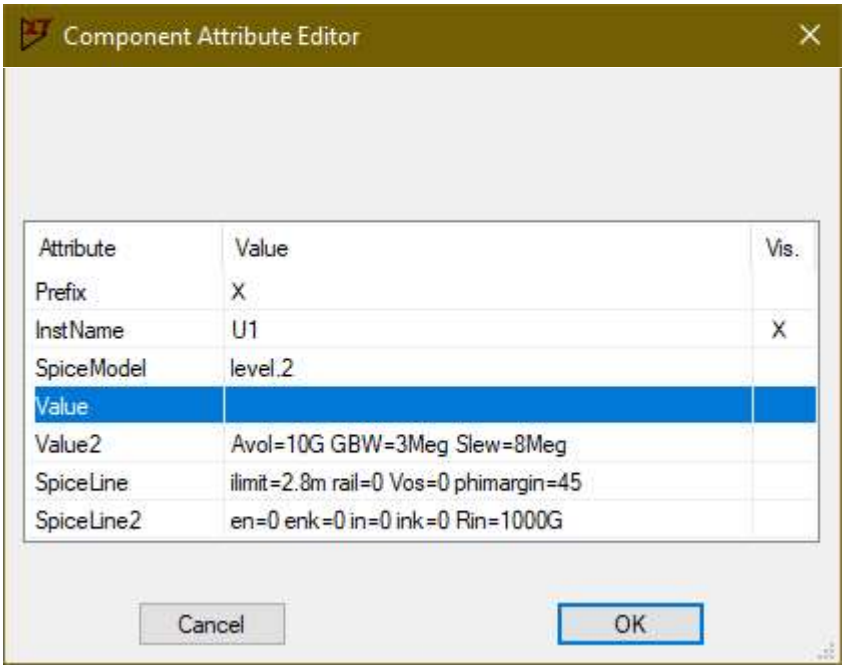


Figure 27 – Virtual Op-Amp Settings

PCB design for Voltage Followers

The PCB for the measurement sensor was designed in EAGLE (version 9.5.2) and is shown in Figure 28. The footprint size for the resistor and capacitors were 1206. Two 0.1 µF ceramic capacitors were used at the terminals as a non-DC bypass path.

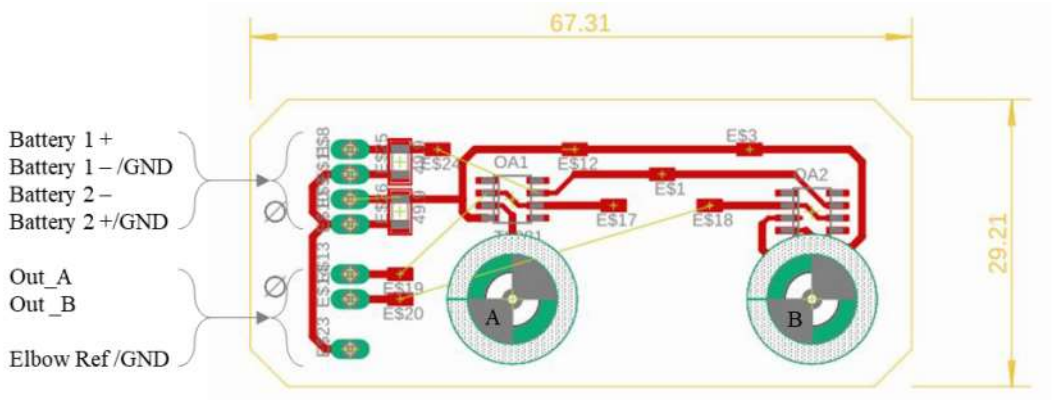


Figure 28 – PCB design for the Measurement sensor

The two 5.5 mm diameter holes with pads, marked ‘A’ and ‘B’, were connected to the inputs of the two voltage followers. The holes mounted female press-studs and therefore able to fasten onto the male press-studs of hydrogel electrodes. The centres of the 5.5 mm holes were 32 mm apart so that two hydrogel pads can be positioned side by side without overlapping.

The terminals of the batteries were connected to wires that are soldered on the pads on the top-left. The isolated V_{CC} and V_{EE} for the op-amps require jumper wires to connect them to the battery bus. The yellow lines in Figure 28 indicate the jumper wire relationship.

The pad below E$23 was used to attach the wire that connects to the elbow electrode to the DC ground bus.

To minimise inductive coupling noise in the sensor, a shielded seven-core cable was used to connect the PCB to the batteries and the oscilloscope. The two unmarked holes on the left were used to fasten down the cable to prevent strain on the PCB’s pads, and thus prevent jitter from loose wires or contacts.

4.2. Experiment Procedure

The experiment had three parts: The participant preparation, participant parameter measurements, and the experimental measurements.

4.2.1. Preparation

The areas on the participant's right arm where the hydrogel electrode pads were to be placed were cleaned using alcohol cleansing pads to provide the best adhesion between the hydrogel electrode pads and the skin. As mentioned in the literature review, the gentle cleaning of the skin surface reduces skin impedance.

The two hydrogel electrodes were placed on the bicep of the right arm's such that the span between the proximal electrode on the bicep and the shoulder would be equidistant to the span between the distal electrode on the bicep and the elbow. The reference hydrogel electrode was placed on the right elbow's bone.

4.2.2. Participant Parameter measurements

The participant parameter measurements comprised of taking dimensional measurements and the H2H impedance measurements of the participants.

Dimensional Measurements

Dimensional measurements were recorded to enable calculations to be made using Equations (12) to (15), from Section 3.2.5, for each participant. The dimensional measurements recorded are listed below and shown in Figure 29.

- Hand-to-hand arm span,
- Hand widths (taken in the middle of the palm where the width is the widest),
- The span between Elbow electrode to Electrode A (*Span A*), and
- The span between Shoulder to Electrode B *(Span B*).

The distance between the two electrode centres was always 32 mm due to the distance between the press-stud connectors on the sensor PCB

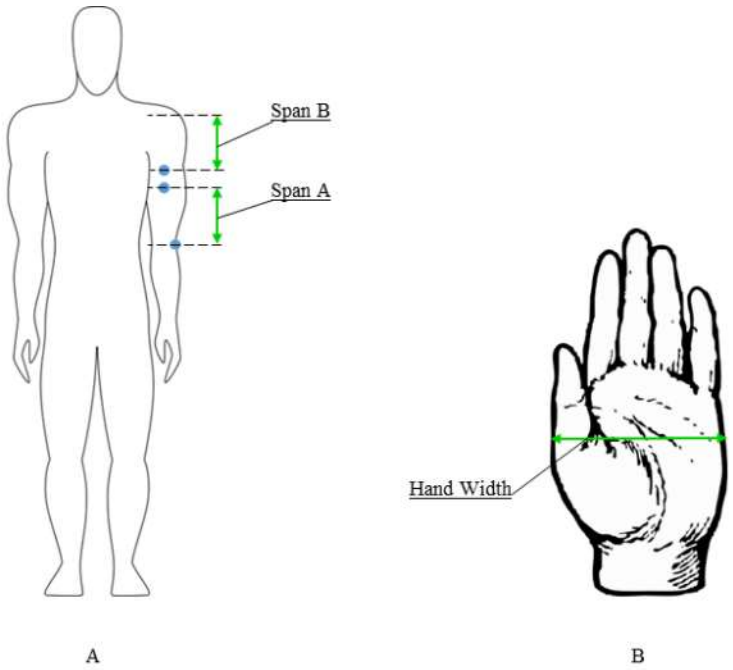


Figure 29 – Pre-Experiment measurements of Body Parameter A) Measurement of placement of the electrodes (marked with blue dots) and arms span. Human body outline adapted from *Clker-Free-Vector-Images* [29]. B) Measurement region of hand width. Palm image was available through Creative Commons Licence [61]

Hand to Hand Impedance Measurement Setup

An H2H impedance measurement experiment was devised to estimate the impedance that would occur when grasping the flat power cable. Like the H2H impedance measurement system described in Chinen et. al. [62], the devised experiment used copper tape wrapped around a 2×0.75 mm^2, flat power cable to make grasping surfaces for each hand. These surfaces are intended to mimic the grasping surface area of the participant's hand.

Each of the copper pieces joined lead wires that connected to each of the LCR meter terminals. When the participant grasps both the copper pieces with each hand, it would close the path between the plates and impedance can be measured by the inductance, capacitance and resistance (LCR) meter.

The pieces of copper tape had the dimensions of 20 mm × 150 mm. When these pieces were wrapped, there would be a 5 mm overlap which allows soldering a seam. Figure 30 is the hand-to-hand impedance measurement setup. A “TECPEL LCR 612” LCR meter was used to measure the series resistance and series capacitance of the participants.

It was expected that the participants will grasp the copper surfaces with a comfortable, medium force grasp as shown in Figure 31. Similar to the literature on hydrogel pads, closing the skin surfaces from open-air increases skin moisture retention and thus reduces the resistance, and increases the capacitance. It was noticed that resistance and capacitance measurements stabilised after 1 minute of grasping.

The approximate contact areas of the copper pieces were 1560 mm^2 for a 100 mm hand width. Grasping directly on the cable sheath resulted in a contact area of 1410 mm^2 for the 100 mm hand width.



Figure 30 – Hand-to-hand Impedance measurement setup. A Type P3 (2 × 0.75mm) cable was wrapped with copper tape on its end. The brown wire was connected to the copper plate on the left to the red node of the LCR meter. The black node was connected to the right copper plate with a jumper wire.

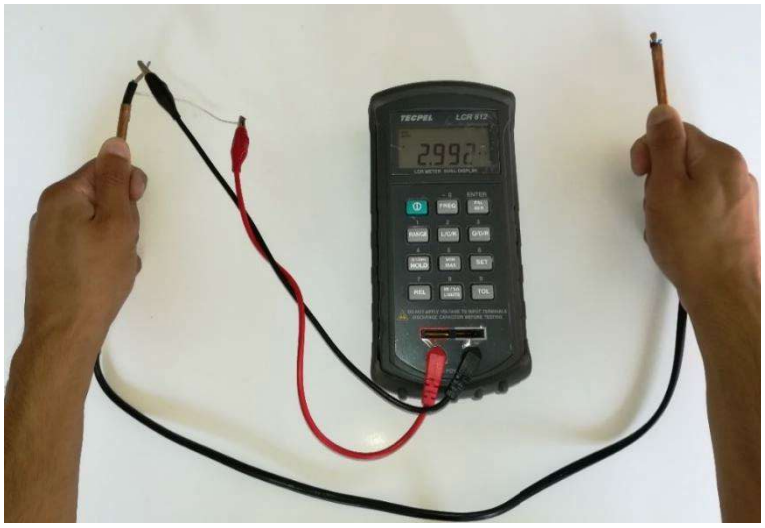


Figure 31 – Grasping the Hand-to-hand Impedance measurement setup

4.2.3. Experiment

As described at the beginning of this chapter, the main experiment took place in an Anechoic Chamber. Once the participant was in the chamber, the EMI sensor was connected to the electrodes on the participant. The experimental setup is shown in Figure 32.

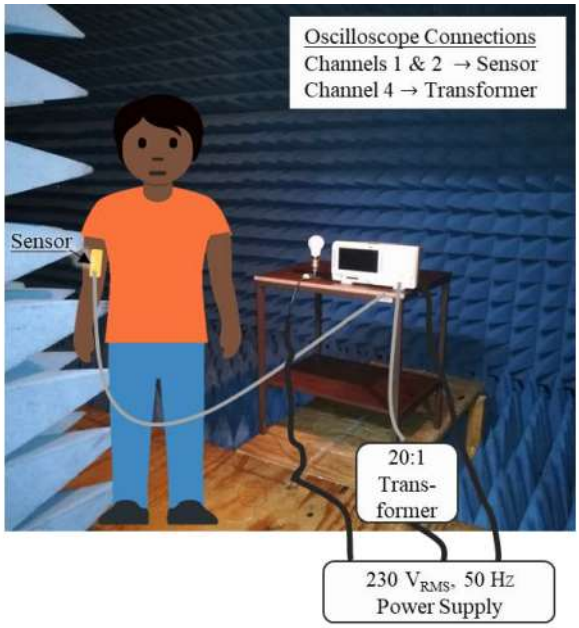


Figure 32 – Simplified setup for the experiment in the Anechoic Chamber. Participant does not hold any surfaces during baseline measurements. Figure of person was available through Creative Commons Licence [63]

Observations during Experimental Setup Preparation

With the source measurement used as a reference. It was observed that the 50 Hz EMI sine waves, measured at terminals *Out_A* and *Out_B*, both had phase differences that changed depending on the orientation of the grasp and the angle of the cable in the grasp. For example, when the left hand grasped the cable in such a way that the live wire side of the cable was orientated closest to knuckles. The EMI signal and the source signal looked as if they were almost in-phase. Whereas, if the cable orientation was changed such that the neutral wire side of the cable was closest to knuckles, i.e. a 180° rotation. The EMI signal and the source signal looked as if they were almost 180° out-of-phase. This occurrence led to the decision to record the two wire orientations within the left hand grasp which are shown in Figure 33.

Case 1 was given the description ‘Live-in-Palm’ because the live wire’s position was adjacent to the palm compared to the neutral wire. Case 2 was given the

description ‘Neutral-in-Palm’ because the neutral wire’s position was adjacent to the palm compared to the live wire.

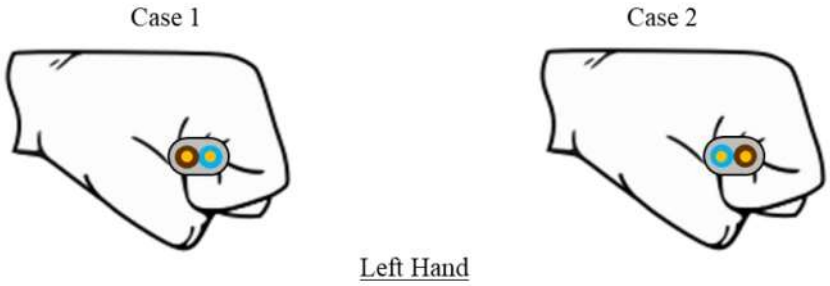


Figure 33 – Two cases of the main experiment where the cable has are in two different rotational orientation in the hand. Note that the experiment had the thumb was placed on the cable for a more natural grip. Figure of fist was adapted through Creative Commons Licence [64]

Oscilloscope Measurement Procedure

Three groups of measurements were recorded on the oscilloscope. The 1st group was the baseline measurement. The 2nd group was to collect the main experiment measurements as described in the above observation section. And the 3rd group was to collected additional measurements but with the right hand grasping the cable.

Oscilloscope Measurement 1: Baseline: A baseline measurement was recorded where the participant was standing beside the table, but not touching any surfaces, as shown in Figure 32. This baseline measurement was to record the ambient EMI induced voltage and was used for yielding net measurements when interacting with the cable. This ambient voltage may be due to inductive coupling between the supply and the participant, or the EMI could be due to inherent noise with the measurement sensor or oscilloscope.

Oscilloscope Measurements 2 and 3: Case 1 and Case 2 As shown in Figure 34, the main experiment required the participant to grasp the lamp’s insulated cable while the oscilloscope recorded the EMI measurements. This was performed for both Case 1 and Case 2, which were Measurements 2 and 3 respectively. The participant was made sure to not be tramping any power cable or grounding paths that would have affected the purpose of the experiment.

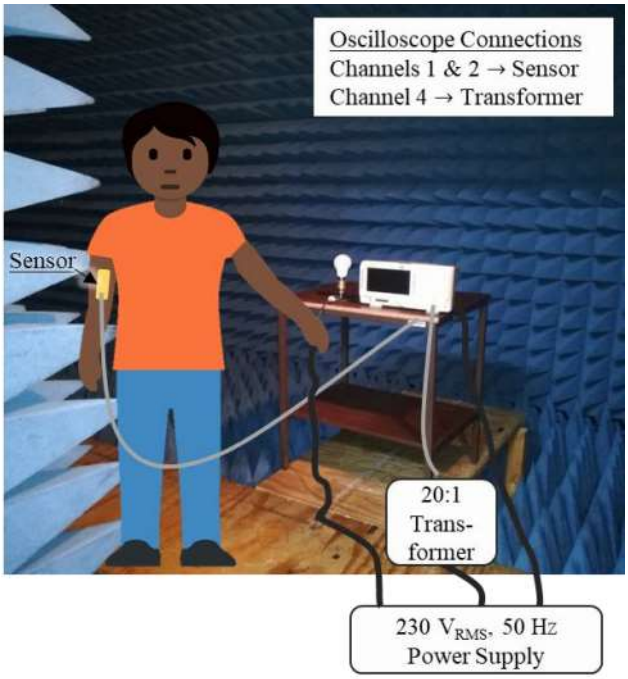


Figure 34 – Simplified setup for the Case 1 and Case 2 experiment in the Anechoic Chamber. Figure of person was available through Creative Commons Licence [63]

Oscilloscope Measurements 4 and 5: Case 3 and Case 4 In these two cases, the EMI will be introduced to the body using the right hand instead, while the EMI sensor remained in the same position as found in Measurements 1 to 3. These purpose of these two additional measurements was for reducing the error in the optimisation process of the human body model.

As shown in Figure 35, this experiment required the participant to grasp the lamp's insulated cable while the oscilloscope recorded the EMI measurements. Like the main experiment measurements, there were two cases of wire orientation in the right hand's grasp, which are shown in Figure 36.

Case 3 was given the description 'Neutral-in-Palm' because the neutral wire's position was adjacent to the palm compared to the live wire. Case 4 was given the description 'Live-in-Palm' because the live wire's position was adjacent to the palm compared to the neutral wire.

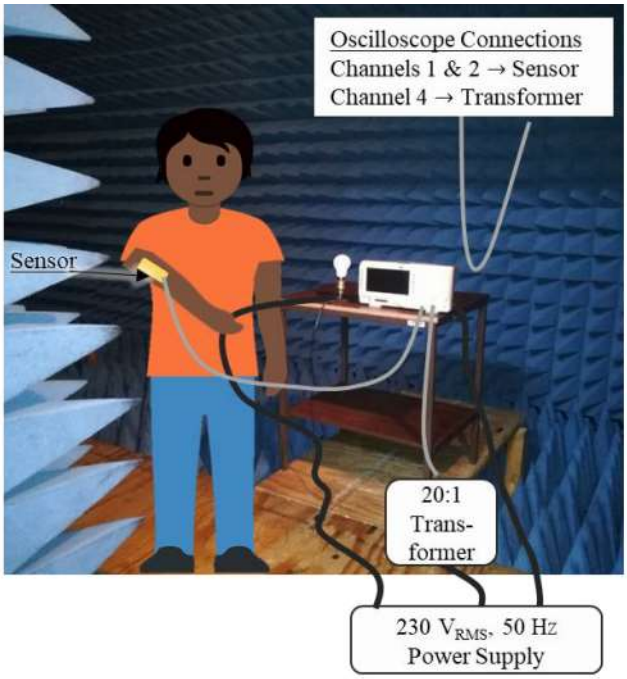


Figure 35 – Simplified setup for the Case 3 and Case 4 experiment in the Anechoic Chamber. Figure of person was available through Creative Commons Licence [63]

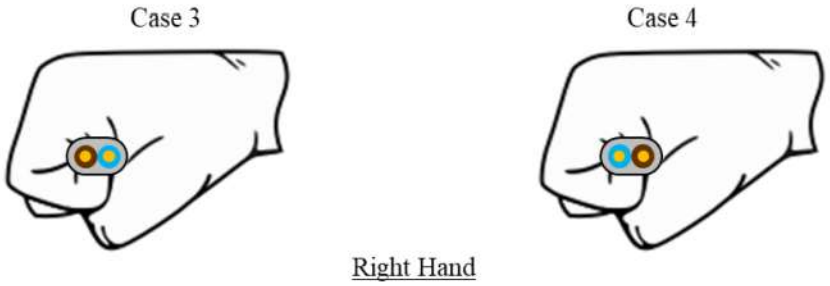


Figure 36 – Two cases of the validation experiment where the cable has are in two different rotational orientation in the hand. Note that the experiment had the thumb was placed on the cable for a more natural grip **Error! Bookmark not defined.**.

4.2.4. Discussion

The benefit of measuring the four different cases was to observe the changes to the EMI due to a change in tissue medium quantity between the sensor and the EMI source, and the EMI's galvanic circulation direction. As well as to validate the model by changing the position of the EMI input position. The grasp had the thumb

placed on the cable because participants found it a more natural grip and thus increased the contact surface area for the CC.

The re-iteration of the case descriptions is below.

- Case 1: Left Hand – Live-in-Palm
- Case 2: Left Hand – Neutral-in-Palm
- Case 3: Right Hand – Neutral-in-Palm
- Case 4: Right Hand – Live-in-Palm

4.3. Results

In this sub-section, the participant parameters and experiment measurements are analysed and discussed.

4.3.1. Participant Parameter Measurements

THE EXPERIMENT WAS CONDUCTED WITH 18 NON-AMPUTEE, RIGHT-HANDED DOMINANT PARTICIPANTS. THE GENDER DEMOGRAPHICS OF THE DATA SAMPLE WAS 11 MALES AND 7 FEMALES AND THE RANGES OF THE PARTICIPANT CHARACTERISTICS ARE SHOWN IN TABLE 10.

Table 11 is a record of the participant parameter measurements.

TABLE 10 – RANGES OF NON-AMPUTEE PARTICIPANT SAMPLE SET

Participant Characteristics	Minimum	Maximum	Mean
Hand Width (Both) (m)	0.090	0.115	0.100
Hand-to-hand Resistance (Ω)	1370	2540	1966
Hand-to-hand Capacitance (nF)	22.52	93.15	45.17

TABLE 11 – PARTICIPANT PARAMETER MEASUREMENTS RECORDED OFF NON-AMPUTEE PARTICIPANTS

		Hand Width		Distance between Electrodes		Hand- to-hand Impedance	
Participant ID	Gender	Right (m)	Left (m)	Span A (m)	Span B (m)	Resistance (Ω)	Capacitance (nF)
Participant A	Female	0.100	0.100	0.100	0.140	2085	55.94
Participant B	Male	0.105	0.105	0.140	0.130	2540	36.52
Participant C	Male	0.100	0.100	0.125	0.125	2222	40.06
Participant D	Male	0.115	0.115	0.130	0.130	1370	48.64
Participant G	Male	0.100	0.100	0.130	0.120	2193	22.52
Participant H	Male	0.100	0.100	0.130	0.140	2400	24.03
Participant I	Female	0.095	0.095	0.110	0.150	1410	93.15
Participant J	Male	0.095	0.095	0.120	0.180	1835	49.41
Participant K	Male	0.100	0.100	0.130	0.130	1650	62.26
Participant L	Female	0.090	0.090	0.140	0.130	1737	33.89
Participant M	Male	0.105	0.105	0.150	0.150	1667	55.26
Participant N	Male	0.100	0.100	0.100	0.140	1810	59.33
Participant O	Male	0.100	0.100	0.130	0.140	1938	33.50
Participant P	Female	0.100	0.100	0.130	0.140	2031	66.40
Participant Q	Female	0.095	0.095	0.120	0.130	2292	62.02
Participant R	Female	0.090	0.090	0.120	0.120	2316	36.70
Participant S	Female	0.095	0.095	0.120	0.130	2213	35.19
Participant T	Male	0.115	0.115	0.140	0.140	1792	35.19

4.3.2. Experiment Measurements

Table 12, Table 13 and Table 14 contain the peak voltage measurements when processing all the non-amputee participants' raw data as described in the next sub-section using Participant C as the sample.

TABLE 12 – CONDENSED TABLE OF NON-AMPUTEE BASELINE MEASUREMENTS FOR MAIN EXPERIMENT

		Hand-to-Hand Impedance		Baseline			
Participant ID	Hand Width (m)	Resis. (Ω)	Cap. (nF)	Out_A (mV)	Out_B (mV)	Δ Out (μV)	Source (V)
Participant A	0.100	2085	55.94	0.966	0.928	37.7	330.0
Participant B	0.105	2540	36.52	0.763	0.746	16.7	330.0
Participant C	0.100	2222	40.06	0.773	0.775	-2.8	332.0
Participant D	0.115	1370	48.64	0.613	0.629	-16.3	330.0
Participant G	0.100	2193	22.52	0.959	0.939	20.4	329.6
Participant H	0.100	2400	24.03	0.813	0.815	-1.9	330.3
Participant I	0.095	1410	93.15	0.365	0.386	-21.2	328.0
Participant J	0.095	1835	49.41	0.758	0.753	5.4	330.8
Participant K	0.100	1650	62.26	0.926	0.935	-9.8	329.9
Participant L	0.090	1737	33.89	2.315	2.381	-66.0	328.0
Participant M	0.105	1667	55.26	1.750	1.765	-14.7	330.2
Participant N	0.100	1810	59.33	1.017	0.996	21.2	332.0
Participant O	0.100	1938	33.50	2.375	2.382	-7.3	328.6
Participant P	0.100	2031	66.40	2.259	2.246	12.9	328.0
Participant Q	0.095	2292	62.02	1.754	1.754	0.6	330.6
Participant R	0.090	2316	36.70	1.810	1.824	-14.5	330.7
Participant S	0.095	2213	35.19	0.775	0.772	2.7	328.0
Participant T	0.115	1792	35.19	1.617	1.607	10.5	330.0

TABLE 13 – CONDENSED TABLE OF NON-AMPUTEE CASE 1 AND CASE 2 MAIN MEASUREMENTS OF THE EXPERIMENT.

	Case 1: Left hand, Live-in-Palm				Case 2: Left hand, Neutral-in-Palm			
Participant ID	Out_A (mV)	Out_B (mV)	Δ Out (μV)	Source (V)	Out_A (mV)	Out_B (mV)	Δ Out (μV)	Source (V)
Participant A	7.65	7.63	19.95	330.0	3.68	3.70	-0.02	330.0
Participant B	5.49	5.46	29.45	330.0	4.20	4.20	0.00	330.0
Participant C	13.24	13.18	56.65	332.1	15.32	15.32	0.70	330.0
Participant D	12.67	12.70	-29.35	329.9	14.07	14.07	-6.95	328.0
Participant G	7.07	7.04	28.55	329.4	11.36	11.30	58.05	332.0
Participant H	7.20	7.20	7.90	332.0	10.88	10.88	0.40	332.0
Participant I	8.18	8.21	-25.15	328.1	12.27	12.29	-17.30	329.4
Participant J	10.89	10.91	-19.70	330.4	20.38	20.43	-58.60	330.8
Participant K	6.60	6.61	-11.75	330.0	12.69	12.72	-35.90	328.2
Participant L	6.36	6.32	45.05	328.2	8.69	8.67	20.30	328.1
Participant M	8.44	8.45	-2.40	330.1	21.70	21.65	50.60	328.9
Participant N	5.67	5.73	-55.70	330.2	4.38	4.40	-22.33	330.8
Participant O	12.75	12.75	0.00	330.0	9.69	9.69	-2.80	329.4
Participant P	17.43	17.49	-63.55	328.0	24.66	24.69	-24.30	328.0
Participant Q	10.69	10.69	-4.30	332.0	14.02	13.97	45.00	332.0
Participant R	11.47	11.51	-35.15	330.0	15.25	15.25	-1.80	332.0
Participant S	9.85	9.86	-7.40	328.2	15.67	15.66	7.25	328.0
Participant T	11.74	11.70	39.50	331.8	13.44	13.39	41.75	332.0

TABLE 14 – CONDENSED TABLE OF NON-AMPUTEE CASE 3 AND CASE 4 VALIDATION MEASUREMENTS OF THE EXPERIMENT.

Participant ID	Case 3: Right hand, Neutral-in-Palm				Case 4: Right hand, Live-in-Palm			
	Out_A (mV)	Out_B (mV)	Δ Out (μV)	Source (V)	Out_A (mV)	Out_B (mV)	Δ Out (μV)	Source (V)
Participant A	10.47	10.45	0.02	330.0	9.29	9.29	0.00	330.0
Participant B	8.95	8.92	0.03	330.0	10.85	10.91	-0.06	330.0
Participant C	14.87	14.83	40.05	331.8	14.62	14.68	-61.15	332.2
Participant D	17.00	17.04	-32.85	328.0	11.52	11.46	59.15	328.0
Participant G	14.76	14.75	9.70	330.4	19.50	19.44	64.95	332.0
Participant H	10.64	10.66	-18.50	330.0	4.60	4.61	-3.28	330.1
Participant I	8.53	8.55	-19.65	328.0	7.75	7.71	45.00	330.0
Participant J	10.12	10.08	32.95	329.2	7.86	7.83	33.65	329.8
Participant K	9.64	9.73	-92.45	329.2	7.88	7.91	-31.00	328.2
Participant L	10.83	10.79	42.75	330.0	16.03	15.99	40.05	330.0
Participant M	19.80	19.75	54.60	329.0	4.20	4.18	23.73	328.4
Participant N	7.71	7.61	94.50	330.0	5.76	5.76	-1.50	328.0
Participant O	16.89	16.95	-60.80	328.0	8.49	8.49	-4.95	328.2
Participant P	25.78	25.78	1.45	328.0	21.91	21.84	72.30	328.0
Participant Q	11.63	11.62	11.50	332.0	9.71	9.69	22.80	330.0
Participant R	15.49	15.46	25.15	331.3	13.97	13.92	42.65	331.9
Participant S	14.81	14.83	-18.25	329.7	5.37	5.36	15.10	332.0
Participant T	22.27	22.20	62.90	331.9	13.11	12.98	128.65	330.9

Sample Data – Participant C

THE PURPOSE OF PRESENTING THE SAMPLE DATA WAS TO DEMONSTRATE THE PHASE DIFFERENCES BETWEEN THE FOUR CASES. PARTICIPANT **C**'S PRE-EXPERIMENT MEASUREMENTS ARE SHOWN IN TABLE 15 (SOURCED FROM Table 11). Summary measurements, shown in Figure 37 to Figure 41.

Table 16, were obtained by processing the "$V_{P\text{-}P} \div 2$" values obtained from the plots shown in Figure 37 to Figure 41. Terms "Filtered" or "10 kHz Filtered" are described in the endnote on Page 60 [ii].

TABLE 15 – PARTICIPANT **C'S** PARAMETER MEASUREMENTS RECORDED FROM (SOURCED FROM

TABLE 11).

	Hand width		Distance		Grasping Hand-to-hand Impedance	
Arm Span (m)	Right (m)	Left (m)	Elbow to A (m)	Shoulder to B (m)	Resistance (Ω)	Capacitance (nF)
1.65	0.10	0.10	0.125	0.125	2222	40.06

TABLE 16 – SUMMARY OF MEASUREMENTS RECORDED FROM PARTICIPANT C

$V_{p-p} \div 2$ (Filtered)	*Out_A* (mV)	*Out_B* (mV)	*Δ Out* (μV)	*Source* (V)	Δ Phase (ms)
Baseline	0.773	0.775	-2.81	332.0	N/A
Case 1: Left Hand –Live-in-Palm	13.236	13.179	56.65	332.1	19.57
Case 2: Left Hand – Neutral in-Palm	15.321	15.320	0.7	330.0	9.44
Case 3: Right Hand –Neutral-in-Palm	14.869	14.829	40.05	331.8	9.48
Case 4: Right Hand – Live-in-Palm	14.619	14.680	-61.2	332.2	19.60

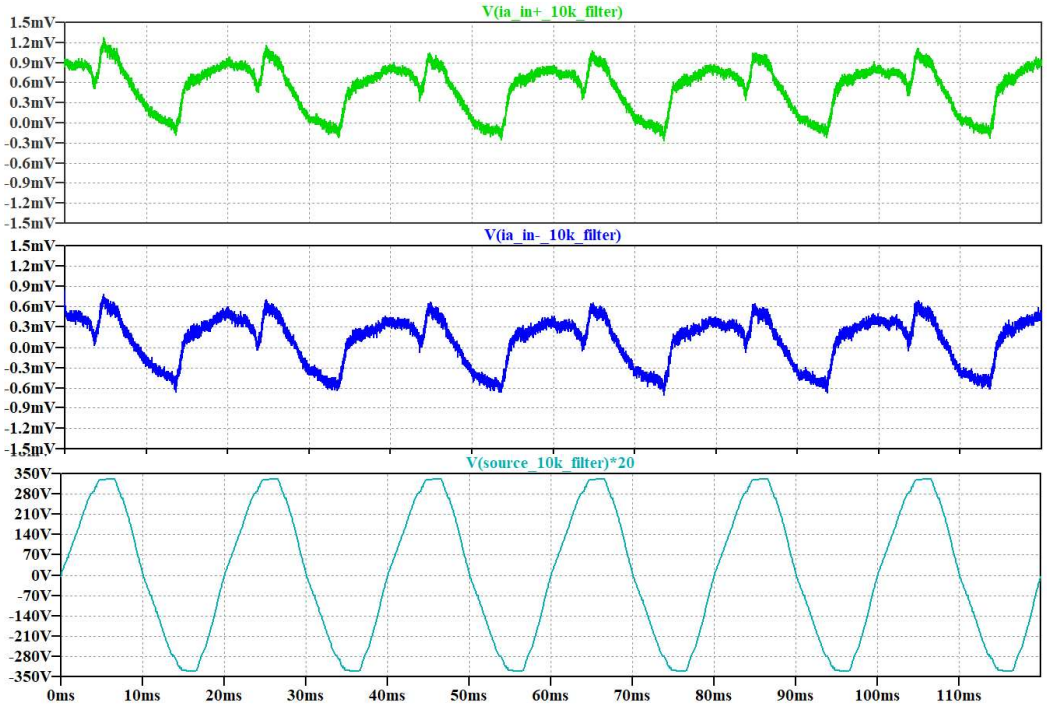


Figure 37 – Baseline Measurements of Participant **C**. Measurements taken from the Voltage Follower Outputs for Electrode A and B; and Plug point source with 20:1 Step Down Transformer.

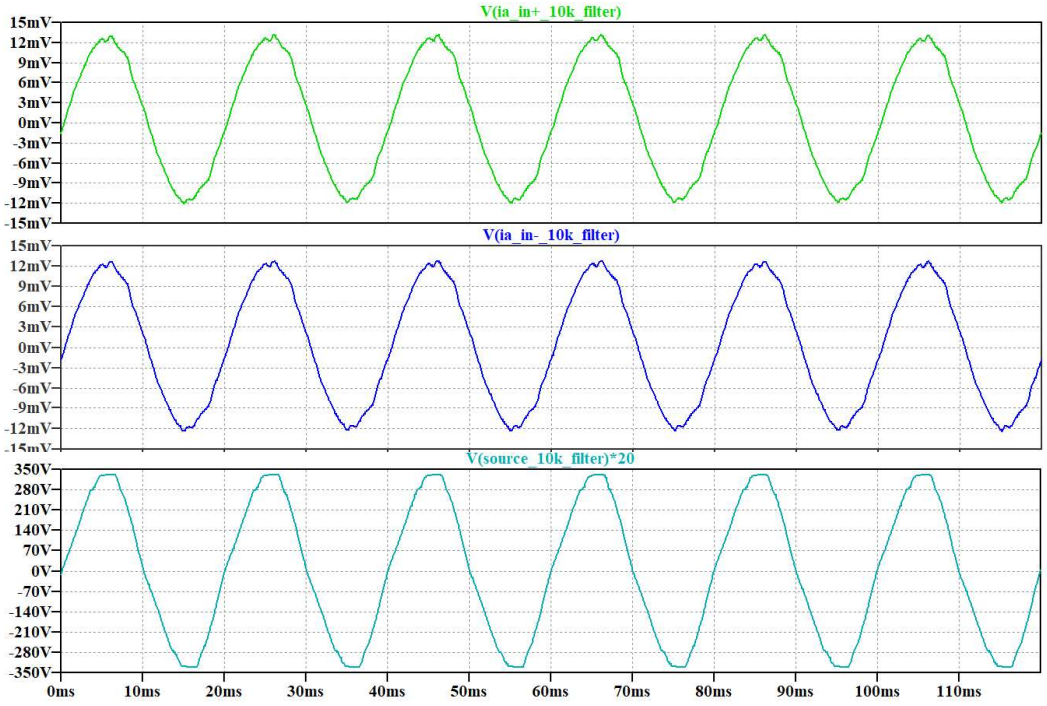


Figure 38 – Case 1 Measurement of Participant **C**. Measurements taken from the Voltage Follower Outputs for Electrode A and B; and Plug point source with 20:1 Step Down Transformer.

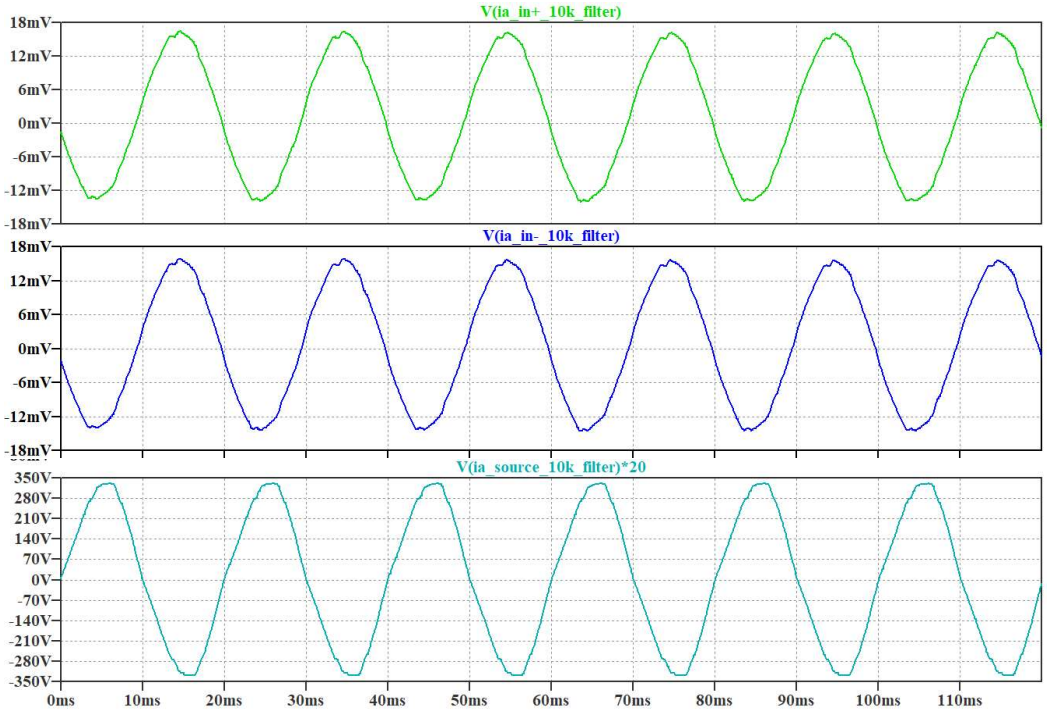


Figure 39 – Case 2 Measurements of Participant **C**. Measurements taken from the Voltage Follower Outputs for Electrode A and B; and Plug point source with 20:1 Step Down Transformer.

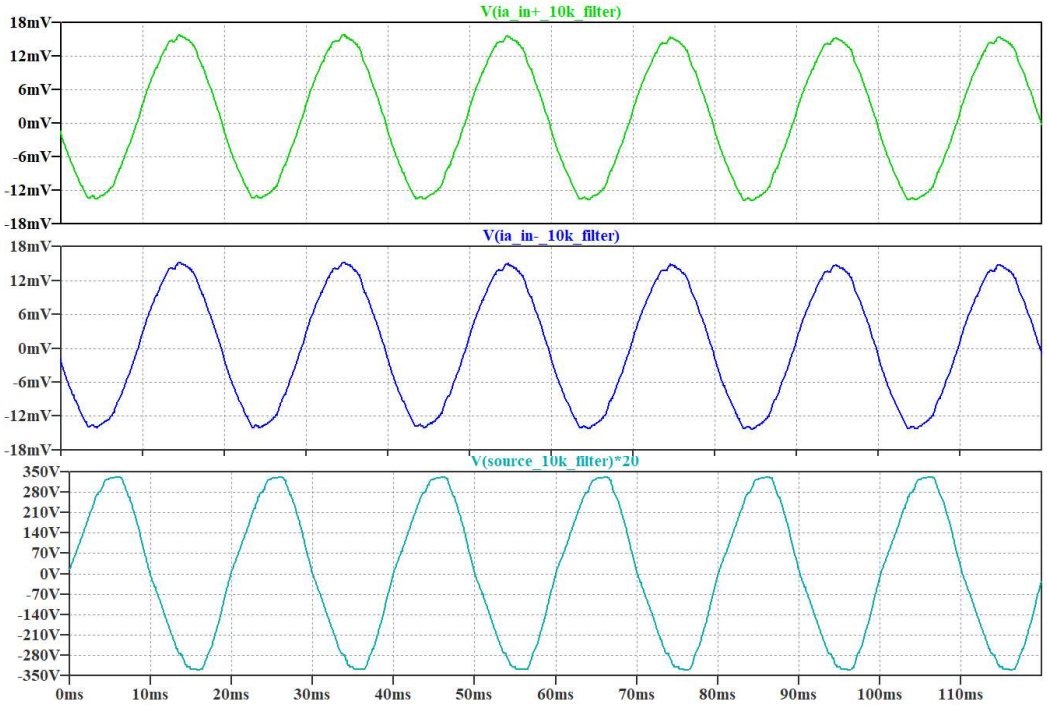


Figure 40 – Case 3 Measurements of Participant **C**. Measurements taken from the Voltage Follower Outputs for Electrode A and B; and Plug point source with 20:1 Step Down Transformer.

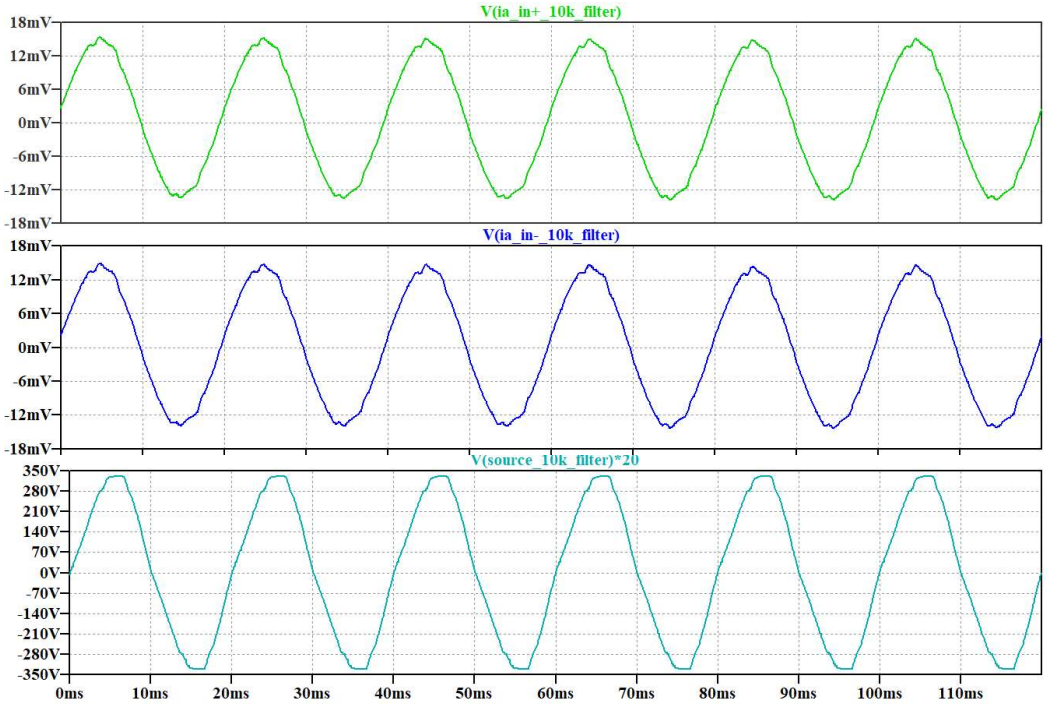


Figure 41 – Case 4 Measurements of Participant **C**. Measurements taken from the Voltage Follower Outputs for Electrode A and B; and Plug point source with 20:1 Step Down Transformer.

Sample Data – Discussion

Several characteristics of the data were noted and listed below.

- Signals from Case 2 and Case 3, as shown in Figure 39 and Figure 40, produce similar results for the IA inputs and display an almost 10 ms phase delay after the source.
- Case 1 and Case 4, as shown in Figure 38 and Figure 41, produced similar results for the IA inputs.
- The phase differences between the Cases 1 & 4 set and the Cases 2 & 3 set indicate that there possibly was galvanic circulation and changing the polarity of the EMI noise source, changes the polarity of the IA measurements.

4.3.3. Experiment Data Analysis

ANALYSIS OF THE DATA FROM

Table 12 to Table 14 is processed using the column headings, Voltage Follower Output Measurements and Source measurements, to do basic statistical calculations.

Voltage Follower Output Measurements (Out_A and Out_B)

The "$Out_A - Out_B$" amplitudes are shown in Table 17. The range was found to be between -92.45 μV and 128 μV. There was no particular correlation between the Cases and the polarity of the difference. The percentage of the difference relative to the average across both voltage followers was calculated and also shown in this table. The range of the percentages was found to be between -0.98 % and 1.23 %. The average and median percentages across all four channels were found to be 0.074 % and 0.002 %, respectively.

The average and median values above indicate the "$Out_A - Out_B$" amplitudes were small enough that averaging *Out_A* and *Out_B* magnitude for each participant can be considered. Table 18 is the result of the calculation. The magnitudes across the four cases ranged between 3.69 mV and 25.78 mV. The magnitudes for the baseline measurements ranged from 0.38 mV to 2.38 mV.

TABLE 17 – ANALYSIS OF OUTPUT VOLTAGES DIFFERENCE BETWEEN ELECTRODES FOR ALL FOUR CASES

	Out_A − Out_B (μV)				$\frac{Output\ Difference}{Output\ Average}$ %			
Participant ID	Case 1	Case 2	Case 3	Case 4	Case 1	Case 2	Case 3	Case 4
Participant A	19.95	-0.02	0.02	0.00	0.27%	2.06%	0.14%	0.43%
Participant B	29.45	0.00	0.03	-0.06	0.27%	0.59%	0.14%	0.76%
Participant C	56.65	0.70	40.05	-61.15	0.48%	0.02%	0.30%	0.42%
Participant D	-29.35	-6.95	-32.85	59.15	0.11%	0.07%	0.10%	0.69%
Participant G	28.55	58.05	9.70	64.95	0.13%	0.36%	0.08%	0.24%
Participant H	7.90	0.40	-18.50	-3.28	0.15%	0.02%	0.17%	0.04%
Participant I	-25.15	-17.30	-19.65	45.00	0.05%	0.03%	0.02%	0.90%
Participant J	-19.70	-58.60	32.95	33.65	0.25%	0.33%	0.29%	0.40%
Participant K	-11.75	-35.90	-92.45	-31.00	0.03%	0.22%	0.94%	0.30%
Participant L	45.05	20.30	42.75	40.05	2.78%	1.36%	1.28%	0.78%
Participant M	-2.40	50.60	54.60	23.73	0.18%	0.33%	0.38%	1.58%
Participant N	-55.70	-22.33	94.50	-1.50	1.64%	1.29%	1.10%	0.48%
Participant O	0.00	-2.80	-60.80	-4.95	0.07%	0.06%	0.37%	0.04%
Participant P	-63.55	-24.30	1.45	72.30	0.50%	0.17%	0.05%	0.30%
Participant Q	-4.30	45.00	11.50	22.80	0.05%	0.36%	0.11%	0.28%
Participant R	-35.15	-1.80	25.15	42.65	0.21%	0.09%	0.29%	0.47%
Participant S	-7.40	7.25	-18.25	15.10	0.11%	0.03%	0.15%	0.27%

Participant T	39.50	41.75	62.90	128.65	0.29%	0.26%	0.25%	1.03%

TABLE 18 – AVERAGED OUTPUT VOLTAGES BETWEEN ELECTRODES FOR ALL FOUR CASES

	Average Voltage (mV)				
Participant ID	Baseline	Case 1	Case 2	Case 3	Case 4
Participant A	0.947	7.64	3.69	10.46	9.29
Participant B	0.754	5.48	4.20	8.93	10.88
Participant C	0.774	13.21	15.32	14.85	14.65
Participant D	0.621	12.69	14.07	17.02	11.49
Participant G	0.949	7.05	11.33	14.75	19.47
Participant H	0.814	7.20	10.88	10.65	4.60
Participant I	0.375	8.19	12.28	8.54	7.73
Participant J	0.756	10.90	20.41	10.10	7.85
Participant K	0.931	6.60	12.71	9.68	7.90
Participant L	2.348	6.34	8.68	10.81	16.01
Participant M	1.757	8.44	21.67	19.77	4.19
Participant N	1.007	5.70	4.39	7.66	5.76
Participant O	2.379	12.75	9.69	16.92	8.49
Participant P	2.252	17.46	24.68	25.78	21.88
Participant Q	1.754	10.69	13.99	11.62	9.70
Participant R	1.817	11.49	15.25	15.47	13.94
Participant S	0.774	9.85	15.66	14.82	5.37
Participant T	1.612	11.72	13.42	22.24	13.05

The Baseline measurement was conducted to record the offset due to any residual coupling in the Anechoic Chamber. By subtracting the offset from each of the Case measurements, the EMI due to only interacting with the cable is obtained. The result is shown in Table 19. Average and median calculations were taken across the four Cases. The nine shaded entries in the table indicate a less than ±5% difference between the median and average measurements. The nine remaining unshaded entries indicate that the dataset has a high level of skewness and may result in larger errors when fitting the model to the data. Figure 42 describes the data found in Table 19 in a box-and-whisker graph. From the box-and-whisker graph, one can see that there is a variety of values and a pattern is not easily discernible.

TABLE 19 – ANALYSIS OF AVERAGED VOLTAGE FOLLOWER OUTPUT VOLTAGES, BASELINE OFFSET REMOVED, FOR ALL FOUR CASES. SHADED VALUES INDICATE A LESS THAN ±5% DIFFERENCE BETWEEN THE MEDIAN AND AVERAGE MEASUREMENTS

	Average Voltage – Baseline Offset Removed(mV)					
Participant ID	Case 1	Case 2	Case 3	Case 4	Average	Median
Participant A	6.69	2.74	9.51	8.34	6.82	7.51
Participant B	4.72	3.45	8.18	10.13	6.62	6.45

Participant C	12.43	14.55	14.07	13.88	13.73	13.98
Participant D	12.07	13.45	16.40	10.87	13.19	12.76
Participant G	6.10	10.38	13.80	18.52	12.20	12.09
Participant H	6.39	10.06	9.83	3.79	7.52	8.11
Participant I	7.82	11.90	8.16	7.35	8.81	7.99
Participant J	10.14	19.65	9.34	7.09	11.56	9.74
Participant K	5.67	11.78	8.75	6.97	8.29	7.86
Participant L	3.99	6.34	8.46	13.66	8.11	7.40
Participant M	6.69	19.91	18.02	2.43	11.76	12.35
Participant N	4.70	3.39	6.65	4.75	4.87	4.72
Participant O	10.38	7.31	14.54	6.11	9.58	8.84
Participant P	15.21	22.42	23.52	19.62	20.20	21.02
Participant Q	8.93	12.24	9.87	7.94	9.75	9.40
Participant R	9.67	13.43	13.66	12.13	12.22	12.78
Participant S	9.08	14.89	14.05	4.59	10.65	11.56
Participant T	10.10	11.80	20.62	11.43	13.49	11.62

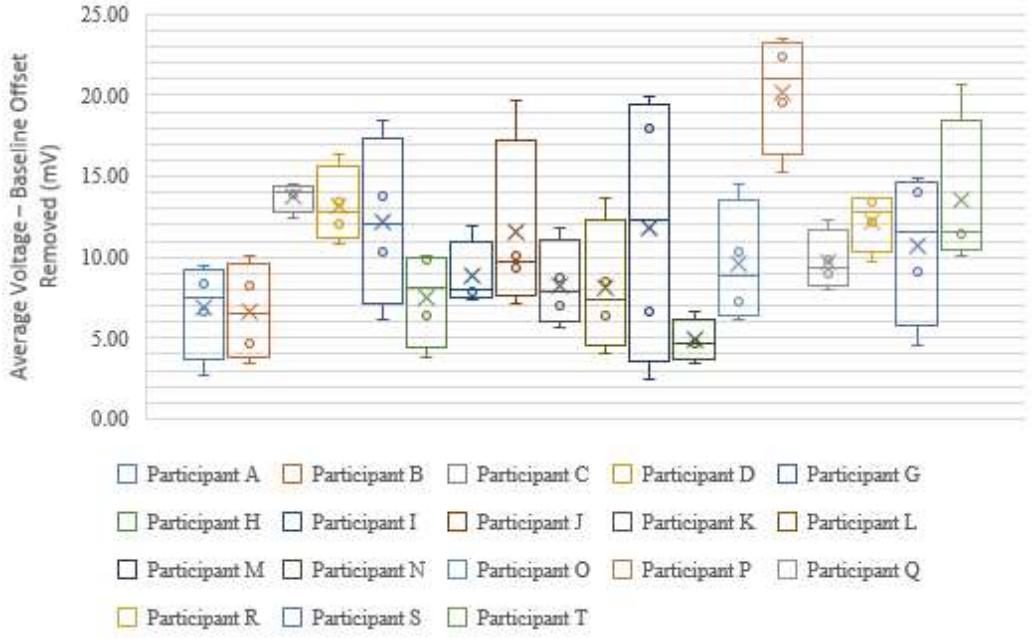


Figure 42 – Box and Whisker Diagram of Averaged Voltage Follower Output Voltages, Baseline Offset Removed, for all Four Cases.

Source

The power supply or source was measured to have a range between 328 V and 332.2 V across all the participants. The average and median were 329.9 V and 330 V, respectively.

4.3.4. Experiment Discussion

A generalised deduction that the human bodies conduct EMI due to contact with insulated, AC-powered objects can be made from the tables and figures in Section 4.3.2. The tables and figures presented to demonstrate that the four Case measurements recorded when the participant was grasping the cable was noticeably larger than the baseline measurements.

This controlled environment resulted in the EMI coupled to participants, which the baseline offset is removed, ranged from 2.4 mV_{peak} to 23.5 mV_{peak}. This magnitude is higher than the EMG signals produced at low to mild stimulation. Given another prepared environment with multiple EMI sources due to electrical equipment and cabling. It is hypothesised that one can expect far higher EMI induced voltage measurement circulating through the body. Capacitive coupling to multiple, parallel sources would result in lower capacitive reactance due to Equation (1) and thus, the human body is less insulated and allocated a larger potential difference.

Experimentation Reliability

As described in the IEC TS 60479-1, the values of body impedance depend on several factors such as current path, touch voltage, duration of current flow, frequency, degree of moisture of the skin, surface area of contact, the pressure exerted and temperature [33], [34]. Since the pressure exerted, degree of skin moisture and temperature were not controlled parameters or variables, there was a mixture of consistent and inconsistent results collected.

The experiments that yielded the shaded entries in Table 19 can be regarded as reliable data sets as there was a small difference between the median and mean values. The bulk of the data collected potentially infer larger chance of unreliability as there was a noticeable difference between the median and mean. The usual way to remove such inconsistencies require multiple repeated experiments per participant and to have a larger sample of participants, which required more time and resources.

4.4. Chapter Summary

In this chapter, the experimental setup, experimental procedure, and results were discussed. The experiment took place in an Anechoic chamber to mitigate external and uncontrolled EMI sources. A basic voltage follower sensor was used to detect the EMI induced voltages at the participant's bicep when interacting with a flat, two-core cable as a noise source. The data was recorded using an oscilloscope.

The outcomes of the experiment's results are as follows:

- Collections of participant parameters to populate models,
- Collections of participant voltage measurements at the electrodes to determine the appropriate Inter-Pathway Resistance values, and
- A maximum EMI voltage magnitude of 23.52 mV was measured off Participant **P**.

A wide range in the EMI induced voltage measurements could have been due to various degrees of factors such as the participant's skin characteristics, applied pressure of grasp or the contact area of the grasp. Input parameters have been collected to populated the unique models for each participant and the optimisation process discussed in the next section will attempt to proximate to the output measurements are to be used Overall, the data collected does have inconsistencies due to the unique nature of the participants and their actions. Further developments in this human body electric circuit model would benefit from a more intensive follow-up experimentation and confirm the outcomes of this dataset.

[ii] Plots and measurement described by “Filtered” or “10 kHz Filtered” means that the raw data was passed through a 10 kHz Low Pass Filter to attenuate the noise produced by the equipment used in the experiment but still maintain the EMG signal spectrum measured by the IA.

Chapter 5

MODEL ASSEMBLY AND OPTIMIZATION

In this chapter, the model will be assembled from the sub-models discussed in Chapter 3, along with the parameters recorded in Chapter 4. Optimisation using a basic genetic algorithm will be done to narrow the difference between the simulated measurements and the experimental measurements.

5.1. Unified Model of Experiment

Combining the Noise Source model, the H2H human body circuit model and the Measurement system model, we obtain the model in Figure 43 and the Noise Source connection diagram in Figure 44. The colour used in Figure 44 indicates that each of the cases has different connections. See Appendix A for an unabridged circuit diagram of the four cases in the model.

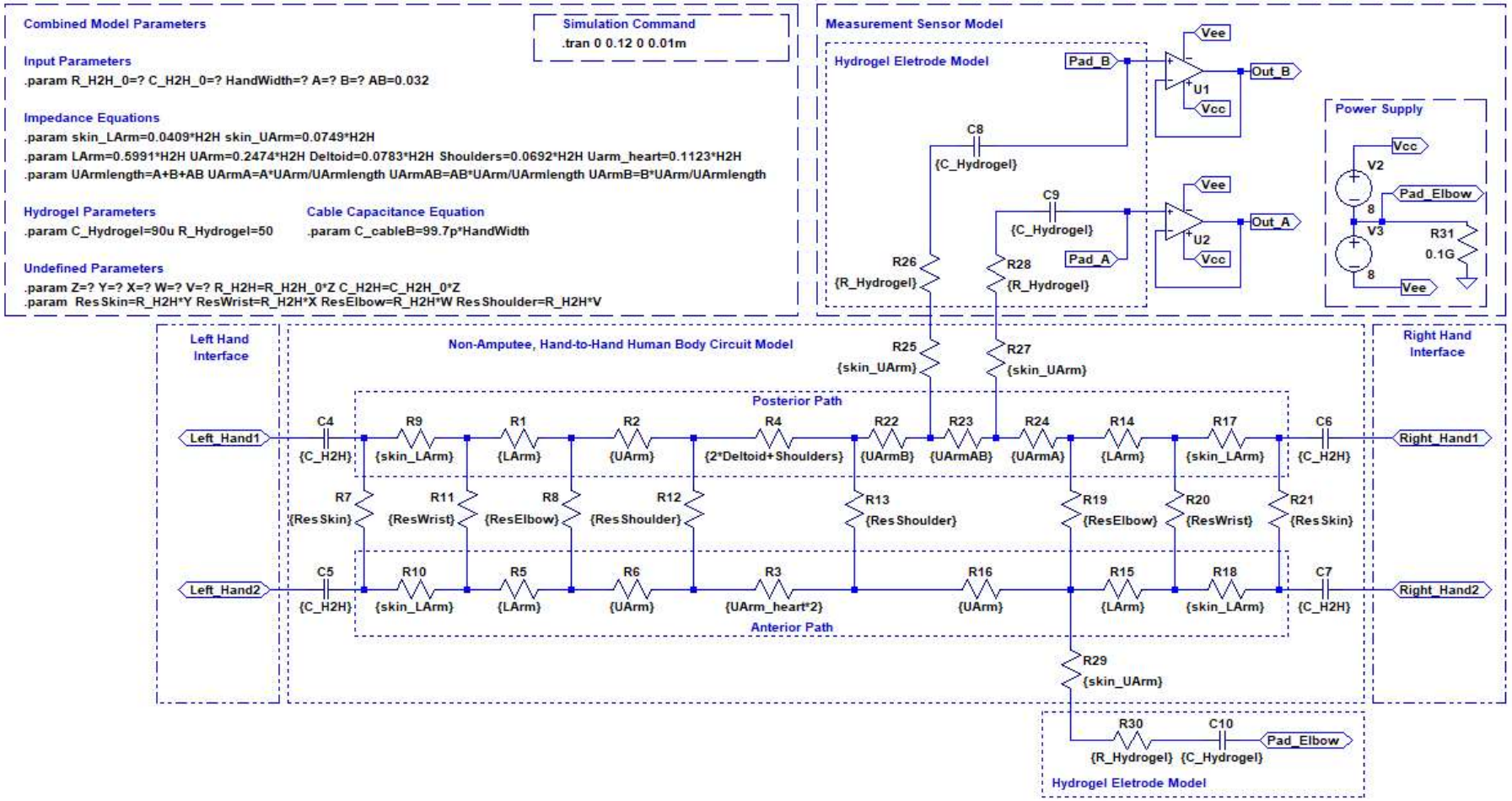


Figure 43 – Unified Model of Experiment, with the Noise Source connection shown in Figure 44

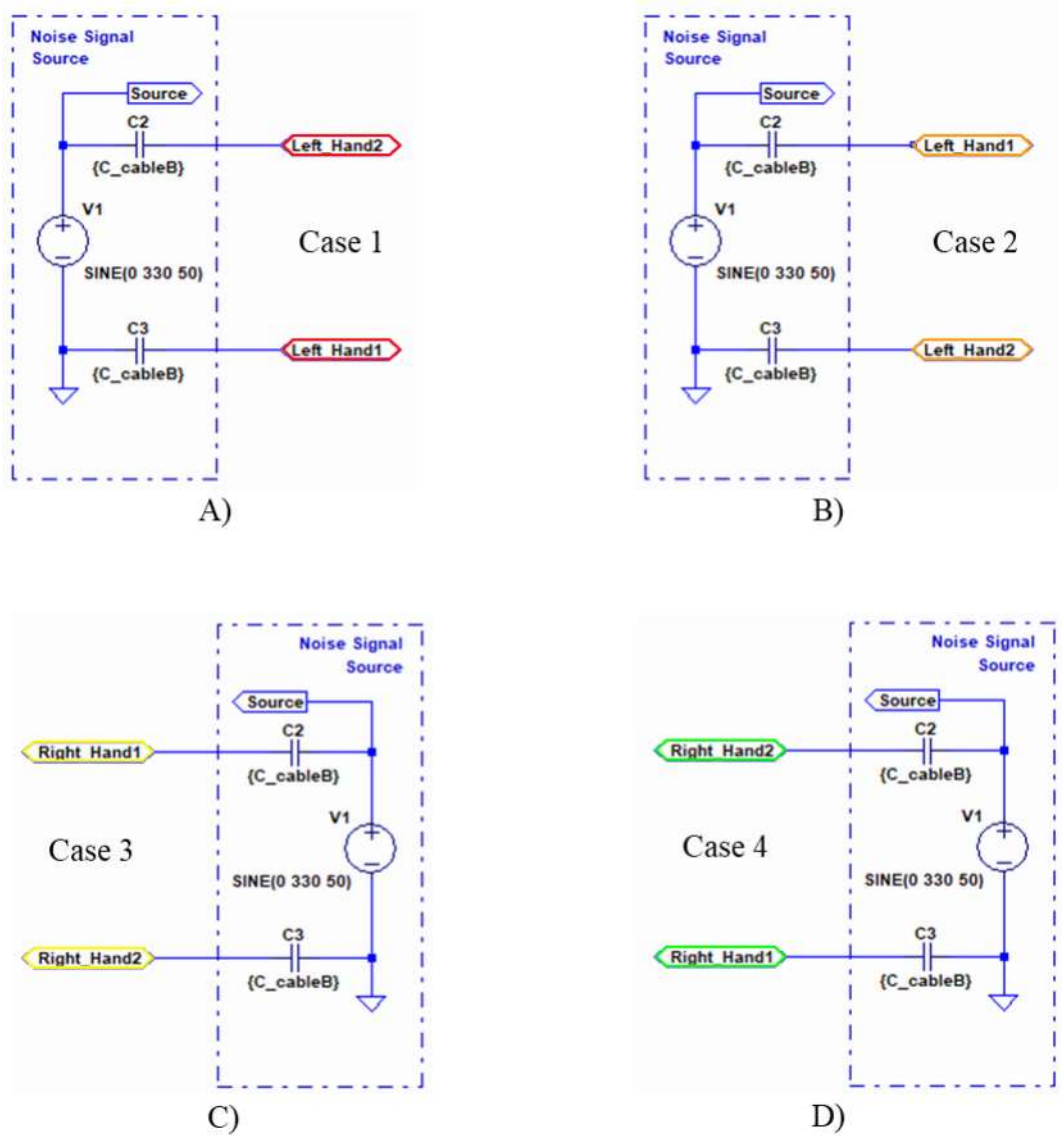


Figure 44 – Noise Source Connection Diagram for the Four Different Cases. A) Case 1, B) Case 2, C) Case3, and D) Case 4

The re-iteration of the case descriptions is below.

- Case 1: Left-Hand grasp – Live-in-Palm cable orientation
- Case 2: Left-Hand grasp – Neutral-in-Palm cable orientation
- Case 3: Right-Hand grasp – Neutral-in-Palm cable orientation
- Case 4: Right-Hand grasp – Live-in-Palm cable orientation

Constant Z

Due to:

- the "hydrating" effect of sanitiser used on the participants before the H2H impedance measurement, and
- the process of correlating H2H impedance to galvanic circulation,

a correction factor constant 'Z' was introduced to scale up the measured H2H impedance, now referred to as 'R_{H2H_0}', to offset the effect of hydrating the participants' hands with sanitizing liquid before the H2H impedance measurements. The resulting mathematical relationships are shown in Equations (16) and (17) and will be used in the optimization process described in the next sub-section.

$$R_{H2H} = Z \times R_{H2H_0}\ (\Omega) \tag{16}$$

$$C_{H2H} = Z \times C_{H2H_0}\ (F) \tag{17}$$

5.2. Model Optimisation Results and Error Calculations

In order to develop the resistance values for *ResSkin*, *ResWrist*, *ResElbow* and *ResShoulder* with the goal of maintain proportionality of the magnitudes with respect to the participant's H2H impedance, a genetic algorithm was developed. The process is described in detail in Appendix C. The parameters *Z*, *Y*, *X*, *W* and *V* used in the optimization process correspond to the correction factor constant and the resistance values for *ResSkin*, *ResWrist*, *ResElbow* and *ResShoulder*, respectively.

The models for each of the 18 participants were simulated as described in Appendix B and the results are shown in Table 20, Table 21, and Table 22. Table 20 describes the Naturally Selected' parameters *Z*, *Y*, *X*, *W* and *V* corresponding to the Participant Parameter inputs to the model.

Table 21 compares the averaged output voltages from the experiment, which follows from Table 19, and the simulation, along with a relative error calculation. Table 22 is a comparison of *V(Out_A) – V(Out_B)* magnitude between the Experiment and the Simulation measurements.

5.2.1. 'Naturally Selected' Parameters *Z*, *Y*, *X*, *W* and *V* Combinations

Table 20 shows the average, median and modes across all the participants. The combination of *Z = 10*, and *Y =X = W= V= 3.16228* appeared twice and was found to be the only combination to be repeated across participants.

TABLE 20 – PARTICIPANT PARAMETERS AND THE' NATURALLY SELECTED' PARAMETERS *Z*, *Y*, *X*, *W* AND *V*

	Participant Parameters (Inputs)					Optimised Parameters Result				
Participant ID	Hand Width (m)	R_{H2H_0} (Ω)	C_{H2H_0} (nF)	Span A (m)	Span B (m)	Z	Y	X	W	V
Participant A	0.100	2085	55.94	0.10	0.14	2.683	10.000	10.000	1.259	1.000
Participant B	0.105	2540	36.52	0.14	0.13	5.179	2.154	2.154	2.154	2.154
Participant C	0.100	2222	40.06	0.125	0.125	7.197	6.813	6.813	6.813	6.813
Participant D	0.115	1370	48.64	0.13	0.13	10.000	10.000	10.000	6.310	6.310
Participant G	0.100	2193	22.52	0.13	0.12	5.179	100.000	10.000	10.000	3.981
Participant H	0.100	2400	24.03	0.13	0.14	7.197	4.642	3.687	3.687	2.326
Participant I	0.095	1410	93.15	0.11	0.15	10.000	6.813	6.813	6.813	6.813
Participant J	0.095	1835	49.41	0.12	0.18	10.000	3.162	3.162	3.162	3.162
Participant K	0.100	1650	62.26	0.13	0.13	10.000	3.162	3.162	3.162	3.162
Participant L	0.090	1737	33.89	0.14	0.13	5.179	100.000	39.811	25.119	1.585
Participant M	0.105	1667	55.26	0.15	0.15	10.000	100.000	3.981	2.512	6.310
Participant N	0.100	1810	59.33	0.10	0.14	10.000	1.000	1.000	1.000	1.000
Participant O	0.100	1938	33.50	0.13	0.14	10.000	4.642	4.642	4.642	4.642
Participant P	0.100	2031	66.40	0.13	0.14	7.197	100.000	10.000	10.000	10.000
Participant Q	0.095	2292	62.02	0.12	0.13	10.000	3.162	2.512	2.512	2.512
Participant R	0.090	2316	36.70	0.12	0.12	10.000	4.642	2.326	1.848	1.848
Participant S	0.095	2213	35.19	0.12	0.13	7.197	6.813	6.813	6.813	5.412
Participant T	0.115	1792	35.19	0.14	0.14	10.000	6.813	4.299	4.299	4.299
Average	0.100	1972	47.22	0.126	0.137	8.167	26.323	7.287	5.672	4.074
Median	0.100	1985	44.35	0.13	0.135	10.000	6.813	4.470	3.993	3.572
Mode	0.100			0.13	0.140	10.000	6.813	10.000	6.813	1.000

5.2.2. Averaged Output Voltages with Relative Error

Table 21 describes the simulation error relative to the experiment measurements. The model's overall average error of 27.42 % was found reasonable due to the inconsistencies in the experiment data and the amount of correction that can be afforded by parameter sweeping five variables. The model's overall median error was 25.14 %. The difference between the average calculation and the median indicates that the model accuracy is skewed and may be due to probabilistic nature of a genetic algorithm coinciding with poorer consistency for Case 4 measurements.

Comparing the average voltages between the simulated values and the experiment measurements for each case. Case 2 and Case 3 appears to be roughly similar by being 1 mV apart or deviating 8.82% and 7.91% for the respective cases. The average for Case 1 and Case 4 were larger than 2 mV, thus less consistent with a 24.1 % and 44.8% deviation respectively. See Figure 45 for a box-and-whisker representation of the each cases' relative errors shown in Table 21. It is shown that the optimisation yielded a range of relative error values as each person is unique. However, if one is gauging the average relative error across participants, one can see that the lower and upper quartile is around 20 % and 30% respectively

Heat Map and Colourisation Analysis

The colour scheme for the heat map was defined as:

- Green is for errors 10 % and lower,
- Yellow is for errors around 20 %, and
- Red is for errors 40 % and higher

By analysing the relative errors for Cases, one can see that 39 % of the individual case entries have green fills, 22% have yellow/orange fills and 39 % have red fills. Collectively, one can see that Case 3 attained the lowest set errors, whereas Case 4 got the highest.

TABLE 21 – COMPARISON AND ERROR CALCULATION OF AVERAGED OUTPUT VOLTAGES BETWEEN EXPERIMENT AND SIMULATION

	Experiment Average Voltage (mV)				Simulation Average Voltage (mV)				Simulation Relative Error %				
Participant ID	Case 1	Case 2	Case 3	Case 4	Case 1	Case 2	Case 3	Case 4	Case 1	Case 2	Case 3	Case 4	Average
Participant A	6.69	2.74	9.51	8.34	2.52	2.80	3.14	2.34	62.28%	2.11%	67.01%	72.00%	50.85%
Participant B	4.72	3.45	8.18	10.13	4.61	5.41	5.51	3.54	2.35%	56.95%	32.58%	65.00%	39.22%
Participant C	12.43	14.55	14.07	13.88	7.51	14.11	15.80	6.25	39.62%	3.00%	12.25%	54.95%	27.45%
Participant D	12.07	13.45	16.40	10.87	7.53	14.50	16.47	7.02	37.62%	7.81%	0.42%	35.44%	20.32%
Participant G	6.10	10.38	13.80	18.52	5.82	12.18	13.95	5.54	4.64%	17.30%	1.05%	70.10%	23.27%
Participant H	6.39	10.06	9.83	3.79	6.34	8.75	9.80	4.71	0.76%	13.02%	0.36%	24.18%	9.58%
Participant I	7.82	11.90	8.16	7.35	6.37	11.89	13.47	5.33	18.53%	0.07%	64.95%	27.46%	27.75%
Participant J	10.14	19.65	9.34	7.09	6.40	11.89	9.66	4.76	36.90%	39.47%	3.40%	32.89%	28.16%
Participant K	5.67	11.78	8.75	6.97	6.09	8.19	8.86	4.56	7.43%	30.44%	1.25%	34.61%	18.43%
Participant L	3.99	6.34	8.46	13.66	3.83	6.93	8.38	3.61	3.94%	9.38%	1.04%	73.53%	21.97%
Participant M	6.69	19.91	18.02	2.43	6.67	11.02	12.58	5.43	0.20%	44.66%	30.19%	123.17%	49.56%
Participant N	4.70	3.39	6.65	4.75	4.70	4.93	4.62	3.58	0.17%	45.55%	30.60%	24.76%	25.27%
Participant O	10.38	7.31	14.54	6.11	7.92	12.60	14.09	6.05	23.68%	72.33%	3.06%	1.00%	25.02%
Participant P	15.21	22.42	23.52	19.62	8.85	22.37	24.86	8.68	41.82%	0.24%	5.68%	55.75%	25.87%
Participant Q	8.93	12.24	9.87	7.94	7.50	9.68	10.43	5.28	16.01%	20.94%	5.69%	33.53%	19.05%
Participant R	9.67	13.43	13.66	12.13	6.73	8.35	8.99	4.54	30.42%	37.80%	34.19%	62.58%	41.25%
Participant S	9.08	14.89	14.05	4.59	6.94	12.76	14.39	5.63	23.56%	14.31%	2.47%	22.54%	15.72%
Participant T	10.10	11.80	20.62	11.43	8.11	12.82	14.46	6.73	19.70%	8.63%	29.88%	41.14%	24.84%
Average	8.38	11.65	12.64	9.42	6.36	10.62	11.64	5.20	20.54%	23.56%	18.12%	47.48%	27.42%
Median	8.38	11.85	11.76	8.14	6.54	11.46	11.50	5.31	19.12%	15.80%	5.69%	38.29%	25.14%

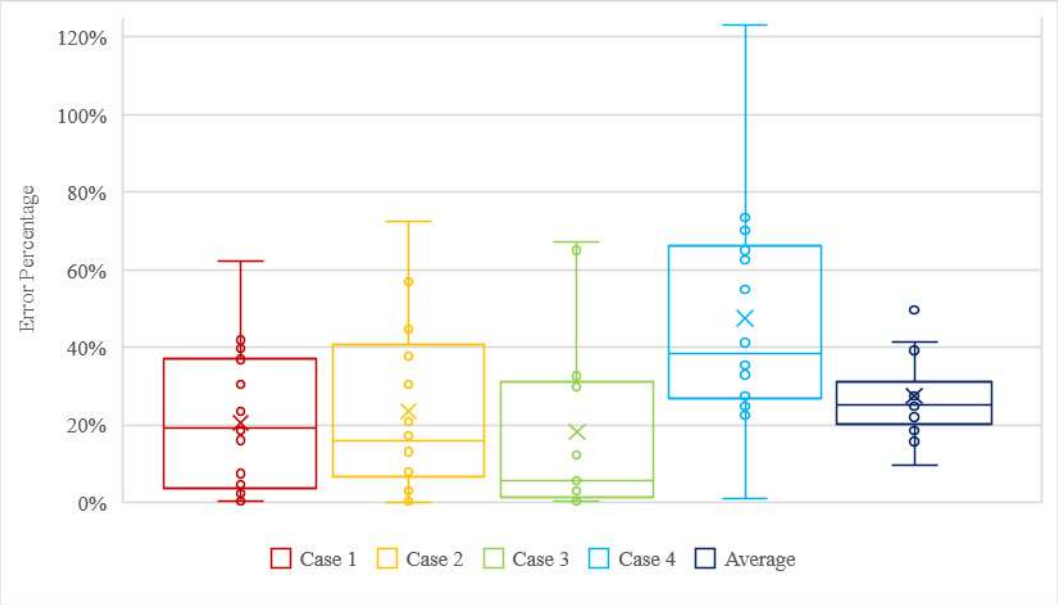


Figure 45 – Box-and-Whisker diagram describing the clustering of relative error data shown in Table 21 for the four different cases.

*Participant **H**'s Best Performance*

Participant **H's** model was found to produce the least amount of errors. The overall error recorded was 9.58%. The good performance was due to the order of the voltage magnitudes where Case 2 and Case 3 both held the higher values, followed by Case 1, and lastly, Case 4 had the smallest value.

5.2.3. *V(Out_A) – V(Out_B)* Magnitude Comparison

The *V(Out_A) – V(Out_B)* measurements in the simulations were used as a fitness criterion for selecting the most suitable parameters for each participant. Due to allowing the magnitude of the difference to be 200 μV, the resulting average for each case being higher than when compared to the experiment results.

TABLE 22 – COMPARISON OF $V(IA_Input+) - V(IA_Input-)$ BETWEEN FROM THE EXPERIMENT AND THE SIMULATION MEASUREMENTS

	$V(IA_Input+) - V(IA_Input-)$ (μV)							
	Experiment Measurements				Simulation Measurements			
Participant ID	Case 1	Case 2	Case 3	Case 4	Case 1	Case 2	Case 3	Case 4
Participant A	19.95	-0.02	0.02	0.00	34.33	45.77	-80.11	-25.75
Participant B	29.45	0.00	0.03	-0.06	68.67	91.55	-99.20	-41.96
Participant C	56.65	0.70	40.05	-61.15	61.05	129.70	-186.95	-55.30
Participant D	-29.35	-6.95	-32.85	59.15	45.80	114.45	-190.70	-61.05
Participant G	28.55	58.05	9.70	64.95	22.85	61.05	-190.75	-56.25
Participant H	7.90	0.40	-18.50	-3.28	72.45	106.85	-183.10	-59.12
Participant I	-25.15	-17.30	-19.65	45.00	45.80	106.85	-152.60	-42.00
Participant J	-19.70	-58.60	32.95	33.65	76.30	106.85	-144.95	-45.78
Participant K	-11.75	-35.90	-92.45	-31.00	83.95	118.25	-144.95	-51.50
Participant L	45.05	20.30	42.75	40.05	3.82	11.40	-175.45	-46.74
Participant M	-2.40	50.60	54.60	23.73	72.50	137.30	-144.95	-45.75
Participant N	-55.70	-22.33	94.50	-1.50	129.70	137.33	-106.81	-64.85
Participant O	0.00	-2.80	-60.80	-4.95	76.30	144.95	-190.75	-61.00
Participant P	-63.55	-24.30	1.45	72.30	38.15	114.45	-198.35	-57.20
Participant Q	-4.30	45.00	11.50	22.80	114.45	164.05	-198.35	-76.30
Participant R	-35.15	-1.80	25.15	42.65	122.05	167.85	-198.35	-70.57
Participant S	-7.40	7.25	-18.25	64.95	57.20	114.45	-186.90	-53.40
Participant T	39.50	41.75	62.90	128.65	76.30	145.00	-198.35	-68.65
Average	-1.52	3.00	7.39	24.78	66.76	112.12	-165.09	-54.62
Median	-3.35	-0.01	5.57	23.26	70.56	114.45	-185.00	-55.77

5.2.4. Discussion

The developed H2H Human Body circuit model estimated the CC-EMI voltage due to the grasp of an insulated flat, two-core power cable, with an overall error of 27.4 %. These errors ranged from 9.58 % to 50.85%, indicating that for some participants, the model does well and for some participants it does not do well. Achieving average errors in the twenties can be considered acceptable because of a relatively novel approach to electrically modelling the human body

5.3. Chapter Summary

In this Chapter, the unified model was created from the sub-models and a genetic algorithm was devised to determine the unknown parameters that represent the

internal resistance of the body. The model's average error across 18 participants was found to be 27.4 %.

The magnitude of the errors was considered acceptable because it was achieved using more accessible equipment than an MRI-based human body impedance measurement procedure. It is a possibility that the approach of inducing EMI into the body using CC maybe the primary contributor to the varying outcome errors since there would be a probabilistic nature in the way a participant would grasp the lamp cable. A more intensive experimentation method that involved repeated tests of participants and a larger participant sample would have improved the quality of the developed model.

Achieving lower errors may benefit from optimising with more than three generations of genetic algorithm., a larger sample and an automated genetic algorithm process. Model validation is required to evaluate the model for consistency.

Chapter 6

MODEL VALIDATION AND CRITICAL ANALYSIS

In this chapter, the process of model validation was conducted to verify the consistency of the developed model. A similar experiment to the one described in Chapter 4 was conducted to collect measurements which the model would need to predict using the inter-pathway resistor parameters obtained in Chapter 5.

A critical analysis of the developed model and research conducted is also discussed, along with potential supporting works that could improve the attempt in modelling the H2H region of the human body as an electric circuit.

6.1. Model Validation

Further inspection of the resulting optimised parameters for each participant in Table 20 indicated there is a loose clustering of similar parameter combinations. As shown in Table 23, there are roughly three clusters. One participant from each cluster returned to participate in the validation experiment so that there was a spread across the participant pool. These participants are Participant **K**, Participant **C** and Participant **P.**

TABLE 23 – CLUSTERING OF PARAMETERS *Z*, *Y*, *X*, *W* AND *V* IN PARTICIPANTS

Participant ID	Z	Y	X	W	V	Cluster
Participant B	5.179	2.154	2.154	2.154	2.154	Cluster 1
Participant Q	10.000	3.162	2.512	2.512	2.512	
Participant J	10.000	3.162	3.162	3.162	3.162	
Participant K	10.000	3.162	3.162	3.162	3.162	
Participant H	7.197	4.642	3.687	3.687	2.326	
Participant R	10.000	4.642	2.326	1.848	1.848	
Participant O	10.000	4.642	4.642	4.642	4.642	
Participant S	7.197	6.813	6.813	6.813	5.412	Cluster 2
Participant C	7.197	6.813	6.813	6.813	6.813	
Participant T	10.000	6.813	4.299	4.299	4.299	
Participant I	10.000	6.813	6.813	6.813	6.813	
Participant D	10.000	10.000	10.000	6.310	6.310	
Participant G	5.179	100.000	10.000	10.000	3.981	Cluster 3
Participant L	5.179	100.000	39.811	25.119	1.585	
Participant P	7.197	100.000	10.000	10.000	10.000	
Participant M	10.000	100.000	3.981	2.512	6.310	
Participant A	2.683	10.000	10.000	1.259	1.000	Ungrouped
Participant N	10.000	1.000	1.000	1.000	1.000	

6.1.1. Validation Experiment

The validation experiment procedure is a mirror of the main experiment procedure discussed in Section 4.2, where the participant is prepared for the EMI sensor to be placed on the left-hand bicep. The reason for mirroring the main experiment was to maintain consistencies with the main experiment and to take advantage of the human body's tendency for bilateral symmetry[65]. This advantage was most beneficial to the model circuitry which only required to be "flipped on the vertical axis" thus saving time on modifying the model for the validation model.

Oscilloscope Measurement Procedure

The same three groups of measurements were recorded as discussed in Section 4.2.3, however the left hand is used instead of the right hand, and vice versa. Each measurement procedure is described below.

Oscilloscope Measurement 1A: Baseline: A baseline measurement was recorded where the participant was standing beside the table, but not touching any surfaces.

Oscilloscope Measurements 2A and 3A: Case 1 and Case 2 these two cases required the participant to grasp the lamp's insulated cable with their right hand while the oscilloscope recorded the EMI voltage measurements. This method was performed for both Case 1 and Case 2, which were Measurements 2 and 3 respectively. The participant was made sure to not be tramping any power cable or grounding paths that would have affected the purpose of the experiment.

Oscilloscope Measurements 4A and 5A: Case 3 and Case 4 In these two cases, the EMI will be introduced to the body using the left hand instead, while the EMI sensor remained in the same position as found in Measurements 1A to 3A.

Comments

The light modification of the main experiment into the validation experiment verifies whether the optimised models of the participants still holds true while still keeping most parameters constant. Since the modification was to mirror the main experiment, this tests confirms that the human body impedance is practically symmetrical along the vertical axis if similar EMI voltage results can be obtained

The re-iteration of the case descriptions is below.

- Case 1: Right Hand – Live-in-Palm
- Case 2: Right Hand – Neutral-in-Palm
- Case 3: Left Hand – Neutral-in-Palm
- Case 4: Left Hand – Live-in-Palm

6.1.2. Validation Experiment Results

In this sub-section, the participant parameters and experiment measurements are discussed.

Participant Parameter Measurements

The experiment was conducted with 3 non-amputee, right-handed dominant participants. The gender demographics of the data sample was 2 males and 1 female. Table 24 is a record of the new participant electrode position measurements. The hand width and H2H impedance measurements was carried over from the main experiment conducted in Section 4.2.3.

TABLE 24 – PARTICIPANT PARAMETER MEASUREMENTS RECORDED OFF NON-AMPUTEE PARTICIPANTS

		Distance between Electrodes	
Participant ID	Gender	Span A (m)	Span B (m)
Participant C	Male	0.125	0.125
Participant K	Male	0.130	0.130
Participant P	Female	0.130	0.140

Validation Experiment Measurements

TABLE 25,

Table 26 and Table 27 contain the peak voltage measurements when processing all the non-amputee participants' raw data as described in the next sub-section using Participant C as the sample.

TABLE 25 – CONDENSED TABLE OF NON-AMPUTEE BASELINE MEASUREMENTS FOR VALIDATION EXPERIMENT

		Hand-to-Hand Impedance		Baseline			
Participant ID	Hand Width (m)	Resis. (Ω)	Cap. (nF)	Out_A (mV)	Out_B (mV)	Δ Out (μV)	Source (V)
Participant C	0.100	2222	40.06	1.10	1.09	14.28	336.6
Participant K	0.100	1650	62.26	1.21	1.23	-21.43	337.3
Participant P	0.100	2031	66.40	0.85	0.85	-2.50	335.9

TABLE 26 – CONDENSED TABLE OF NON-AMPUTEE CASE 1 AND CASE 2 MEASUREMENTS FOR VALIDATION EXPERIMENT

Participant ID	Case 1: Right hand, Live-in-Palm				Case 2: Right hand, Neutral-in-Palm			
	Out_A (mV)	Out_B (mV)	Δ Out (μV)	Source (V)	Out_A (mV)	Out_B (mV)	Δ Out (μV)	Source (V)
Participant C	12.79	12.68	110.15	337.7	16.44	16.46	-17.75	336.4
Participant K	7.08	7.10	-22.80	338.0	10.65	10.63	20.55	336.0
Participant P	7.98	7.96	12.25	337.4	28.03	28.13	-98.60	338.0

TABLE 27 – CONDENSED TABLE OF NON-AMPUTEE CASE 3 AND CASE 4 MEASUREMENTS FOR VALIDATION EXPERIMENT

Participant ID	Case 3: Left hand, Neutral-in-Palm				Case 4: Left hand, Live-in-Palm			
	Out_A (mV)	Out_B (mV)	Δ Out (μV)	Source (V)	Out_A (mV)	Out_B (mV)	Δ Out (μV)	Source (V)
Participant C	17.87	17.86	9.55	338.0	12.40	12.41	-13.00	338.0
Participant K	10.68	10.68	0.25	338.0	6.28	6.32	-42.75	338.0
Participant P	22.93	22.91	16.75	338.0	9.36	9.35	11.90	336.8

6.1.3. Validation Experiment Data Analysis

Analysis of the data from Table 25 to Table 27 is processed using the column headings, Voltage Follower Output Measurements and Source measurements, to do basic statistical calculations.

Voltage Follower Output Measurements (Out_A and Out_B)

Table 18 below is the result of averaging *Out_A* and *Out_B* for each case. The magnitudes across the four cases ranged between 3.69 mV and 25.78 mV. The magnitudes for the baseline measurements ranged from 0.38 mV to 2.38 mV.

TABLE 28 – VALIDATION EXPERIMENT: AVERAGED OUTPUT VOLTAGES BETWEEN ELECTRODES FOR ALL FOUR CASES

	Average Voltage (mV)				
Participant ID	Baseline	Case 1	Case 2	Case 3	Case 4
Participant C	1.09	12.73	16.45	17.86	12.41
Participant K	1.22	7.09	10.64	10.68	6.30
Participant P	0.85	7.97	28.08	22.92	9.35

The result of baseline offset removal is shown in Table 29. The data contained in the table appears to be fairly symmetrical when comparing Case 1 with Case 4, and Case 2 with Case 3.

TABLE 29 – VALIDATION EXPERIMENT: ANALYSIS OF AVERAGED VOLTAGE FOLLOWER OUTPUT VOLTAGES, BASELINE OFFSET REMOVED, FOR ALL FOUR CASES.

	Average Voltage – Baseline Offset Removed(mV)			
Participant ID	Case 1	Case 2	Case 3	Case 4
Participant C	11.64	15.35	16.77	11.31
Participant K	5.87	9.43	9.46	5.09
Participant P	7.12	27.24	22.07	8.51

Source

The power supply or source was measured to have a range between 335.9 V and 338.0 V across all the participants. The average and median were 337.3 V and 337.7 V, respectively.

6.1.4. Validation Model

The unified circuit diagram for the validation experiment is shown in Figure 47 and the corresponding connection diagram for the CC model is shown in Figure 46. Since this validation experiment was a mirror of the main experiment, the only difference is the swapping the positions of the left- and right- hand interface nodes. The inter-pathway parameters Z, Y, X, W and V used in each participant's model was obtained from Table 20.

Due the slight change in supply voltage experienced during the experimentation, the models of the participants will be simulated with a supply of 337.5 V instead of the 330V used during the main experiment.

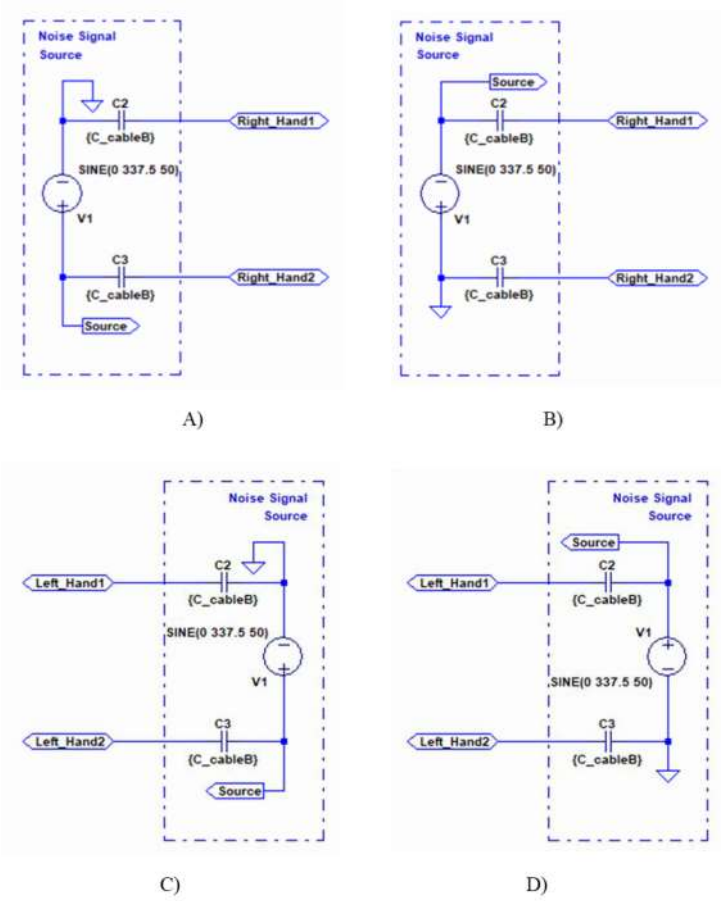


Figure 46 – Noise Source Connection Diagram for the Four Different Cases. A) Case 1, B) Case 2, C) Case3, and D) Case 4

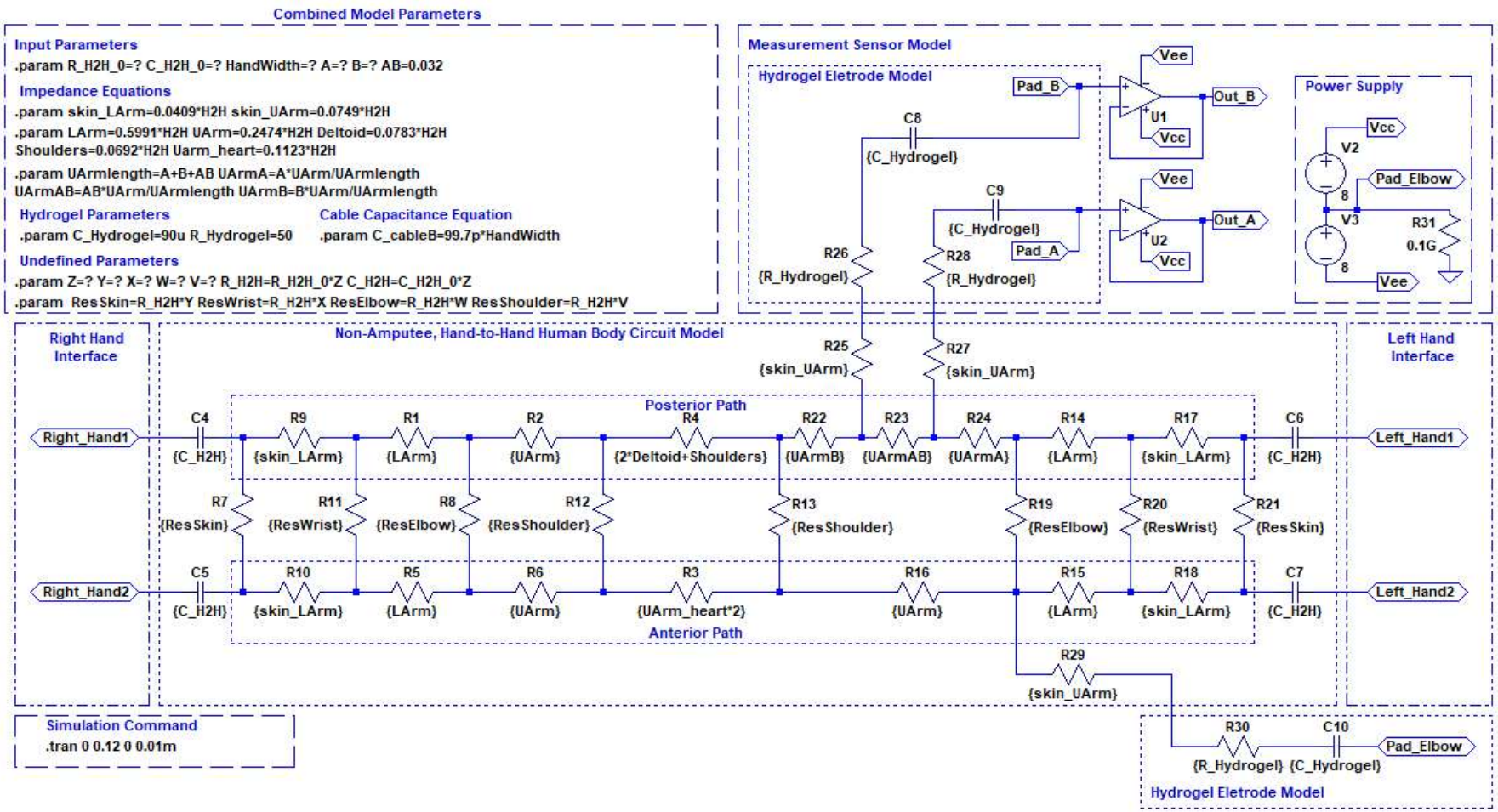


Figure 47 – Unified Model of Validation Experiment, with the Noise Source connection shown in Figure 46

The re-iteration of the case descriptions is below.

- Case 1: Right-Hand grasp – Live-in-Palm cable orientation
- Case 2: Right-Hand grasp – Neutral-in-Palm cable orientation
- Case 3: Left-Hand grasp – Neutral-in-Palm cable orientation
- Case 4: Left-Hand grasp – Live-in-Palm cable orientation

6.1.5. Simulated Results of Validation Model

Table 30 below describes the simulation error relative to the validation experiment measurements. The average error for the model during validation testing was found to be 15 %. This was considered good result; however, the result is tentative due to the small sample size.

Comparing the overall errors for each case, Case 2 and Case 3 again appears to be best performing cases. This time round, Case 1 had the worst average error of 22.4 % instead of Case 4, which now achieved an average error of 18.7%.

6.1.6. Discussion

Using the same heat-map colour scheme from main experiment data analysis, which are defined as; Green is for errors 10 % and lower, Yellow is for errors around 20 %, and Red is for errors 40 % and higher. The heat-map is now predominantly green, coinciding with the lower errors. When comparing the validation data to the main experiment data of the selected participants in Table 31, Case 2 and Case 3 have similar errors for both experiments. A big reduction in errors was found for Case 1 and Case 4.

Overall, the results of the validation experiment and simulation favourably confirms the plausibility of the developed human body electric circuit model.

TABLE 30 – COMPARISON AND ERROR CALCULATION OF AVERAGED OUTPUT VOLTAGES BETWEEN VALIDATION EXPERIMENT AND SIMULATION

	Experiment Average Voltage (mV)				Simulation Average Voltage (mV)				Simulation Relative Error %				
Participant ID	Case 1	Case 2	Case 3	Case 4	Case 1	Case 2	Case 3	Case 4	Case 1	Case 2	Case 3	Case 4	Average
Participant C	11.64	15.35	16.77	11.31	7.68	14.44	16.17	6.39	33.98%	5.96%	3.58%	43.47%	21.75 %
Participant K	5.87	9.43	9.46	5.09	6.23	8.38	9.07	4.66	6.17%	11.12%	4.19%	8.33%	7.45%
Participant P	7.12	27.24	22.07	8.51	9.05	22.89	25.44	8.88	27.06%	15.96%	15.24%	4.42%	15.67%
Average									22.40%	11.01%	7.67%	18.74%	14.96%

TABLE 31 – EXTRACT OF TABLE 21: COMPARISON AND ERROR CALCULATION OF AVERAGED OUTPUT VOLTAGES BETWEEN EXPERIMENT AND SIMULATION

	Experiment Average Voltage (mV)				Simulation Average Voltage (mV)				Simulation Relative Error %				
Participant ID	Case 1	Case 2	Case 3	Case 4	Case 1	Case 2	Case 3	Case 4	Case 1	Case 2	Case 3	Case 4	Average
Participant C	12.43	14.55	14.07	13.88	7.51	14.11	15.80	6.25	39.62%	3.00%	12.25%	54.95%	27.45%
Participant K	5.67	11.78	8.75	6.97	6.09	8.19	8.86	4.56	7.43%	30.44%	1.25%	34.61%	18.43%
Participant P	15.21	22.42	23.52	19.62	8.85	22.37	24.86	8.68	41.82%	0.24%	5.68%	55.75%	25.87%
Average	8.38	11.65	12.64	9.42	6.36	10.62	11.64	5.20	29.62%	11.22%	6.39%	48.43%	23.92%

6.2. Critical Analysis

Modelling the human body as an electric circuit and determining the CC-EMI that flows through the body is not a straightforward task. There is a complex relationship between the measurable external parameters of the participants and the impedances of the electrical current paths within the body. And there are few more parameters, like grasp pressure, that could have been considered and/or controlled to reduce the variations in the EMI measurements.

For the model to obtain a successful outcome, it would have needed to meet the requirements that were discussed in Section 1.5. The sub-sections below discuss the successes and failures of this research, as well as the satisfaction of the problem statement.

6.2.1. Successes

The following objectives were met by the model:

- Developed a higher detailed electrical model of the hand-to-hand path of the human body.
- The Model of the hand-to-hand path of the human body has sufficient complexity, or elements, to further modify the model for alternate scenarios regarding the position of the EMG sensor on the arm.
- The Model of the hand-to-hand path of the human body is designed to interface with dipole EMI sources.
- Simulations of Case 2 and Case 3 models in both the main and validation experiment yield low errors, indicating the acceptability of the model.

6.2.2. Failures

The following objectives were not met by the model:

- Errors yielded from the simulations of Case 1 and Case 4 models do not confirm nor deny the plausibility of the developed model as the main experiment had mainly satisfactory to poor errors, and the validation model had acceptably low errors.
- The ability to simulate varying phase differences between the different cases, using the source as a reference.

The shortcomings of the model were due to the inability to incorporate:

- the op-amp TL081's SPICE model into the simulation, and
- the power supply sample recording from the experiment as the power source in the simulation.

6.2.3. Satisfying Problem Statement

The research was able to identify electrical circuit models that appropriately represents the CC-EMI on EMG measurements conducted on the upper arms of non-amputees.

This model serves as a foundation for future CC-EMI scenarios that would affect persons who use EMG sensors. These potential future scenarios may involve left-hand dominant subjects, amputees, other EMI sources, multiple EMI sources, or other measurement location on the human body.

Common Mode Rejection Ratio

Returning to the objective of determining the CMRR for EMG-sensor design development, the two sources of the data are the empirical experiment measurement and the simulated measurements. The minimum, median and maximum voltage measurements of the empirical data are 2.43 mV, 9.97 mV and 23.5 mV, respectively. The required CMRR required to attenuate these measurements below the required noise of 2 μV_{RMS} are 58.7 dB, 70.9 dB and 78.4 dB, respectively.

For the simulated results, the minimum, median and maximum voltage measurements are 2.34 mV, 7.26 mV and 24.8 mV, respectively. The required CMRR required to attenuate these measurements below the required noise are 58.3 dB, 68.18 dB and 78.9 dB, respectively.

The outcome of the empirical data is a straight forward deduction which tells the observer that the required CMRR would be at least 78.4 dB. However, for the simulated data, the deduction is prone to error which is 27.4 % on average. The minimum and maximum CMRR required are in proximity to the empirical data but there was a much bigger difference between the CMRR from the median values.

If one were to compare the simulated measurements that are associated with the minimum and the maximum from the empirical data described in the paragraph above, the simulated measurements are 5.43 mV and 24.8 mV. The corresponding CMRR required for these two values are 65.7 dB and 78.9 dB. In this case, the minimum is definitely a distinct value but ultimately, the maximum values are of more importance in noise attenuation design and the simulated values correspond to the empirical values.

6.2.4. Research Contributions

The objective of this research is to develop a model that can represent the EMI on EMG measurements taken on an upper limb amputee in a home/office setting. By achieving the objective, some contributions made to this field of research are:

- The expansion of the existing electric circuit model of the upper limbs and upper torso region of human body into the ladder network that can simulate galvanic flow due to a dipole signal source. Thus the model has the ability to detect the polarity change from the EMI source.
- Providing an experiment method which can be used to examine the flow of EMI interference that is due to near-field or capacitive coupling with sources. This method was demonstrated for the events where the subject's

measurements are not ground or common-node referenced to a non-foot region of the human body.

- The experiment method may provide useful data on the magnitudes of the EMI which can assist in EMG sensor design and development. Especially in the noise attenuation techniques where the system is designed for approximated EMI noise "roof" value, and thus the effective CMRR can be determined.
- The model, as a tool, can be used to estimate the EMI magnitude that could be circulating through the subject's body. However, the model requires a reference scenario to calibrate the model with the subject's unique characteristics.
- Results of the simulations may provide the EMI measurements required to calculate the required CMRR against the 20 μV noise floor value.

6.3. Chapter Summary

Through the processes of model validation, the developed model was found to produce favourable results with a small sample of participants. The average errors obtained were 15 % which was an improvement from 23.9 % obtained from the main experiment for the three participants.

The magnitude of the errors was considered acceptable because it was achieved using more accessible equipment than an MRI-based FEM human body impedance measurement procedure. A more intensive experimentation method that involved repeated tests of participants and a larger participant sample would have improved the quality of the developed model.

Chapter 7

FUTURE WORKS AND CONCLUSION

This chapter concludes the research presented in this document. The objectives, methods and results of the research are discussed. As well as the main deductions from the discussion in the previous chapter.

This research was aimed towards the improvement of EMG devices utilised for prosthetic arm devices by assisting in the prediction of CC-EMI magnitudes that the device user will experience in home or office environment. Knowledge of the EMI at the site of the EMG sensor will aid specifying the CMRR required on the device, thus reducing the likelihood of amputees experiencing an unresponsive or uncontrollable prosthetic device that is a burden. To do so, this research address the general problem of the lack of an electric circuit model of the human body that can be applied for the subject capacitively-coupling with a dipole EMI source, like a lamp cable.

Literature on human body electric circuit modelling and electrical properties of the human body was presented. The existing Freiberger human body model was modified to apply for the experiment scenario of a participant grasping a lamp cable with their hands with the EMI sensor placed on the right arm's bicep. A basic equation that describes the relationship between the participant's hand width and the coupling capacitance was developed using COMSOL simulations. This

equation was subsequently used to introduce the EMI to the developed human body circuit model.

The EMI voltage measurements collected during the experimentation phase were used to optimise the participants' unique models for lower errors. The main model achieved an overall error of 27.4 % and an error ranged between 9.58 % to 50.85%. This indicating that for some participants, the model does well and for some participants it does not do well. A validation experiment was conducted and simulated to confirm the optimisation parameters produced by the main experiments data is applicable for more than one scenario. The acceptable average error of 15 % resultant of the validation process indicates that the flexibility of developed model. However, the acceptable outcome is a story of averaged results where one set performs well and the other not so well.

There is a complex relationship between the measurable external parameters of the participants and the impedances of the electrical current paths within the body. And modelling the human body as an electric circuit and determining the CC-EMI that flows through the body is not a straightforward task. A more intensive approach is required for the experimentation process requiring multiple recordings of each case measurement or a segment of the hand-to-hand model needs to be scrutinised before wholly confirming the validity of the developed model.

Overall, the model developed can determine EMI induced currents conducting through the hand-to-hand region of the body and delivers plausible results. Therefore, the developed model should be able to contribute to assisting the CMRR specification of EMG devices in the future.

7.1. Possible Improvements and Future Works

Through the process of the experimental data collection and the model development, the need for accurate and confidently repeatable data as necessary to develop a model with low errors. The sections below discuss some improvements that could be made to improve the experiment and model development.

7.1.1. Experiment

Regarding the experiment, improvements can be made with more data and modifying the scope and experiment design.

More Data

As mentioned several times, the opportunity to conduct multiple data sets for each participant and sampling over a larger and more diversified population would have improved the research outcome. However, due to the health risks and cost implications of such a study during a pandemic, more intensive data collection was not pursued.

Scope and Experiment Design

Possibly, attempting to model the internal impedance of the entire Hand-to-hand span with EMI as a signal source was ambitious. Reducing to modelling objective to a smaller region and adding more measurement nodes for both anterior and posterior paths could have resulted in a model with a lower error deviation. Example cases would be modelling the impedances across the wrist, the lower arm, upper arm, etc. If models of these smaller regions were available, it would reduce the reliance for the genetic algorithm to determine the theoretical impedances between the anterior and posterior pathways.

Alternatively, if the focus was more on the hand-to-hand human body circuit model rather than the EMI, then the access and use of electrical muscle stimulation equipment would have provided a clinically safe way of inducing a controlled electrical signal into the body for the sensor to measure. Controlling more of the parameters discussed in Section 4.3.4 may contribute to more consistent data.

Once the model achieves a more consistent and lower error percentage, then experimenting with inducing EMI with other electrical objects and environments will demonstrate the durability of the model.

7.1.2. Model Development

Regarding the model development, improvements can be made by considering Matlab as the development platform.

LTspice versus Matlab

The main desire to use LTspice was the ease of loading SPICE models of the component used in the sensor circuitry. However, compatibility issues between the parameter sweeping genetic algorithm and the SPICE-coded op-amp resulted in replacing the SPICE-coded op-amp with a virtual op-amp.

Assuming that the use of virtual components was the only option, then it makes more sense to redevelop the model in Matlab. Where the circuit model will reside in Simulink form and the parameter sweeping genetic algorithm would be generated through the Matlab code and interact with the Simulink model.

7.2. Chapter Conclusion

This chapter concludes the research aimed towards improving the EMI noise predictions for EMG-controlled prosthetic hand applications and therefore assist in the development of reliable EMG-controlled prosthetics. Providing amputees with a future with reliable prosthetics will greatly improve their quality of life.

REFERENCES

[1] M. Kutz, 'Bioelectricity and Its Measurement', in *Biomedical Engineering and Design Handbook, Volume 1*, 2nd edition., New York: McGraw-Hill Education, 2009. [Online]. Available: https://www.accessengineeringlibrary.com/content/book/9780071498388/chapter/chapter20

[2] J. H. Nagel, 'Biopotential Amplifiers', in *The Biomedical Engineering Handbook*, Second Edition., J. D. Bronzino, Ed. CRC Press LLC, 2000, p. Chapter 70.

[3] Y. Jiang *et al.*, 'Effective Biopotential Signal Acquisition: Comparison of Different Shielded Drive Technologies', *Applied Sciences*, vol. 8, no. 2, p. 276, Feb. 2018, doi: 10.3390/app8020276.

[4] Y. Jiang *et al.*, 'Comparison of Different Shielding Methods in Acquisition of Physiological Signals', in *2017 39th Annual International Conference of the IEEE Engineering in Medicine and Biology Society (EMBC)*, Seogwipo, Jul. 2017, pp. 2325–2328. doi: 10.1109/EMBC.2017.8037321.

[5] A. Appathurai *et al.*, 'A study on ECG signal characterization and practical implementation of some ECG characterization techniques', *Measurement*, vol. 147, p. 13, Dec. 2019, doi: 10.1016/j.measurement.2019.02.040.

[6] Analog Devices Inc., *Linear Circuit Design Handbook - 1st Edition*, First. MA, USA, 2008. Accessed: Apr. 02, 2019. [Online]. Available: https://www.elsevier.com/books/linear-circuit-design-handbook/zumbahlen/978-0-7506-8703-4

[7] B. Carter, 'High-speed notch filters', *Analog Applications Journal*, no. Q1, p. 8, 2006.

[8] D. T. Mewett, H. Nazeran, and K. J. Reynolds, 'Removing power line noise from recorded EMG', in *2001 Conference Proceedings of the 23rd Annual International Conference of the IEEE Engineering in Medicine and Biology Society*, Istanbul, Turkey, 2001, vol. 3, pp. 2190–2193. doi: 10.1109/IEMBS.2001.1017205.

[9] M. B. I. Reaz, M. S. Hussain, and F. Mohd-Yasin, 'Techniques of EMG signal analysis: detection, processing, classification and applications', *Biological Procedures Online*, vol. 8, no. 1, p. 11, Dec. 2006, doi: 10.1251/bpo115.

[10] S. Yacoub and K. Raoof, 'Noise Removal from Surface Respiratory EMG Signal', *World Academy of Science, Engineering and Technology*, no. 14, pp. 643–650, 2008.

[11] G. Lu *et al.*, 'Removing ECG noise from surface EMG signals using adaptive filtering', *Neuroscience Letters*, vol. 462, no. 1, pp. 14–19, Sep. 2009, doi: 10.1016/j.neulet.2009.06.063.

[12] M. Golabbakhsh, M. Masoumzadeh, and M. F. Sabahi, 'ECG AND POWER LINE NOISE REMOVAL FROM RESPIRATORY EMG SIGNAL USING ADAPTIVE FILTERS', vol. 5, no. 4, p. 6, 2011.

[13] P. Kamboj, 'ECG and PLI Artifacts Cancellation from Electromyogram', *IOSR Journal of Electronics and Communication Engineering*, vol. 3, no. 3, pp. 22–27, 2012, doi: 10.9790/2834-0332227.

[14] M. Patidar, N. Jain, and A. Parikh, 'Classification of Normal and Myopathy EMG Signals using BP Neural Network', *International Journal of Computer Applications*, vol. 69, no. 8, pp. 12–16, May 2013, doi: 10.5120/11861-7645.

[15] J. Piskorowski, 'Time-efficient removal of power-line noise from EMG signals using IIR notch filters with non-zero initial conditions', *Biocybernetics and Biomedical Engineering*, vol. 33, no. 3, pp. 171–178, Jan. 2013, doi: 10.1016/j.bbe.2013.07.006.

[16] F. R. Hashim, J. J. Soraghan, L. Petropoulakis, and N. G. N. Daud, 'EMG cancellation from ECG signals using modified NLMS adaptive filters', in *2014 IEEE Conference on Biomedical Engineering and Sciences (IECBES)*, Kuala Lumpur, Malaysia, Dec. 2014, pp. 735–739. doi: 10.1109/IECBES.2014.7047605.

[17] C. J. De Luca, 'The Use of Surface Electromyography in Biomechanics', *Journal of Applied Biomechanics*, vol. 13, no. 2, pp. 135–163, May 1997, doi: 10.1123/jab.13.2.135.

[18] S. N. Makarov *et al.*, 'Virtual Human Models for Electromagnetic Studies and Their Applications', *IEEE Reviews in Biomedical Engineering*, vol. 10, pp. 95–121, 2017, doi: 10.1109/RBME.2017.2722420.

[19] 'Table 1 | Advantages and disadvantages of imaging modalities used with...', *ResearchGate*. https://www.researchgate.net/figure/Advantages-and-disadvantages-of-imaging-modalities-used-with-targeted-or-non-targeted_tbl1_273515519 (accessed Sep. 28, 2020).

[20] A. Equenazi, M. Flack, and S. Yoo, 'Basic Principles in the Rehabilitation of Persons with Limb Amputation', in *Principles of Rehabilitation Medicine*, Book, Section vols, R. Mitra, Ed. New York, NY: McGraw-Hill Education, 2019. Accessed: May 16, 2019. [Online]. Available: accessmedicine.mhmedical.com/content.aspx?aid=1159832408

[21] D. G. Smith and H. B. Skinner, 'Chapter 11. Amputations', in *Current Diagnosis & Treatment in Orthopedics*, 5th ed., H. B. Skinner and P. J. McMahon, Eds. New York, NY: The McGraw-Hill Companies, 2014. Accessed: May 16, 2019. [Online]. Available: accessmedicine.mhmedical.com/content.aspx?aid=57819330

[22] C. J. De Luca, 'Electromyography', in *Encyclopedia of medical devices and instrumentation*, 2nd ed., vol. 3, 6 vols, J. G. Webster, Ed. Boston, Massachusetts: Wiley-Interscience, 2006, pp. 98–109.

[23] D. Prutchi and M. Norris, *Design and Development of Medical Electronic Instrumentation: A Practical Perspective of the Design, Construction, and Test of Medical Devices*. Hoboken, NJ, USA: John Wiley & Sons, Inc., 2004. doi: 10.1002/0471681849.

[24] C. J. De Luca, 'Surface Electromyography: Detection and Recording', Delsys Incorporated, 2002. [Online]. Available: https://www.delsys.com/Attachments_pdf/WP_SEMGintro.pdf

[25] E. Vavrinsky *et al.*, 'Sensor System for Wireless Bio-Signal Monitoring', *Procedia Chemistry*, vol. 6, pp. 155–164, 2012, doi: 10.1016/j.proche.2012.10.142.

[26] J. V. Basmajian and C. J. De Luca, *Muscles Alive: Their Functions Revealed by Electromyography*. Baltimore: Williams & Wilkins, 1985.

[27] E. A. Clancy, E. L. Morin, and R. Merletti, 'Sampling, noise-reduction and amplitude estimation issues in surface electromyography', *Journal of Electromyography and Kinesiology*, vol. 12, no. 1, pp. 1–16, Feb. 2002, doi: 10.1016/S1050-6411(01)00033-5.

[28] A. Nonclercq and P. Mathys, 'Reduction of power line interference using active electrodes and a driven-right-leg circuit in electroencephalographic recording with a minimum number of electrodes', in *The 26th Annual International Conference of the IEEE Engineering in Medicine and Biology Society*, Sep. 2004, vol. 1, pp. 2247–2250. doi: 10.1109/IEMBS.2004.1403654.

[29] Clker-Free-Vector-Images, *Male Figure Human Free Photo*. Accessed: Oct. 09, 2020. [Online]. Available: https://www.needpix.com/photo/download/29358/male-figure-human-body-form-shape-standing-diagram-free-vector-graphics

[30] O. College, *English: The skeletal muscles of the body typically come in seven different general shapes.* 2013. Accessed: Dec. 28, 2020. [Online]. Available: https://commons.wikimedia.org/wiki/File:Fascicle_Muscle_Shapes.jpg

[31] M. Haberman, A. Cassino, and E. Spinelli, 'Estimation of Stray Coupling Capacitances in Biopotential Measurements', *Med Biol Eng Comput*, vol. 49, no. 9, p. 1067, Jul. 2011, doi: 10.1007/s11517-011-0811-6.

[32] M. S. Wegmüller, 'Intra-Body Communication for Biomedical Sensor Networks', Doctor of Sciences Dissertation, ETH, ZURICH, 2007. [Online]. Available: https://pdfs.semanticscholar.org/a58a/301a413da8a57cd9441d46b3cb2152f0befb.pdf

[33] SOUTH AFRICAN NATIONAL STANDARD, 'SANS 60479-1:2006 - Effects of current on human beings and livestock, Part 1: General aspects'. SABS Standards Division, Jan. 2013.

[34] International Electrotechnical Commission, 'IEC TS 60479-1:2006 - Effects of current on human beings and livestock, Part 1: General aspects'. International Electrotechnical Commission, Jan. 2013.

[35] H. Freiberger, 'Der elektrische widerstand des menschlichen körpers gegen technischen gleich- und wechselstrom ...', J. Springer, Berlin, 1934.

[36] National Research Council (US) and Institute of Medicine (US) Committee on the Mathematics and Physics of Emerging Dynamic Biomedical Imaging, *Electrical Impedance Tomography*. National Academies Press (US), 1996. Accessed: May 05, 2020. [Online]. Available: https://www.ncbi.nlm.nih.gov/books/NBK232489/

[37] B. Kibret, M. Seyedi, D. T. H. Lai, and M. Faulkner, 'Investigation of Galvanic-Coupled Intrabody Communication Using the Human Body Circuit Model', *IEEE J. Biomed. Health Inform.*, vol. 18, no. 4, pp. 1196–1206, Jul. 2014, doi: 10.1109/JBHI.2014.2301165.

[38] M. Fernandez and R. Pallas-Areny, 'A comprehensive model for power-line interference in biopotential measurements', in *IMTC/99. Proceedings of the 16th IEEE Instrumentation and Measurement Technology Conference (Cat. No.99CH36309)*, May 1999, vol. 1, pp. 573–578 vol.1. doi: 10.1109/IMTC.1999.776816.

[39] R. E. Serrano, M. Gasulla, O. Casas, and R. Pallas-Areny, 'Power line interference in ambulatory biopotential measurements', in *Proceedings of the 25th Annual International Conference of the IEEE Engineering in Medicine and Biology Society (IEEE Cat.*

No.03CH37439), Sep. 2003, vol. 4, pp. 3024-3027 Vol.4. doi: 10.1109/IEMBS.2003.1280777.

[40] P. S. Luna-Lozano and R. Pallas-Areny, 'Power-Line Interference in the ECG Obtained with Capacitive Electrodes', in *5th European Conference of the International Federation for Medical and Biological Engineering*, Berlin, Heidelberg, 2012, pp. 910–913. doi: 10.1007/978-3-642-23508-5_236.

[41] Andrews, 'Electrical aspects of lightning strikes to humans', in *The Lightning Flash*, Cooray, Ed. Institution of Engineering and Technology, 2014, pp. 701–723. doi: 10.1049/PBPO069E_ch16.

[42] P. E. Sutherland, 'Circuit Model of the Human Body', in *Principles of Electrical Safety*, Hoboken, NJ, USA: John Wiley & Sons, Inc., 2014, pp. 90–100. doi: 10.1002/9781118886397.ch5.

[43] G. Biegelmeier, 'New Experiments with Regard to Basic Safety Measures for Electrical Equipment and Installations', in *Electrical Shock Safety Criteria*, Elsevier, 1985, pp. 161–172. doi: 10.1016/B978-0-08-025399-2.50014-X.

[44] G. Biegelmeier, 'New Knowledge on the Impedance of the Human Body', in *Electrical Shock Safety Criteria*, Elsevier, 1985, pp. 115–132. doi: 10.1016/B978-0-08-025399-2.50014-X.

[45] G. Biegelmeier, 'Wirkungen des elektrischen Stroms auf Menschen und Nutztiere: Lehrbuch d. Elektropathologie', VDE-Verl, Berlin, Germany, 1986.

[46] J. P. Reilly, 'Chapter 2 - Impedance and Current Distribution', in *Applied Bioelectricity*, New York, NY: Springer New York, 1998, pp. 12–72. doi: 10.1007/978-1-4612-1664-3.

[47] J. P. Reilly, *Applied Bioelectricity*. New York, NY: Springer New York, 1998. doi: 10.1007/978-1-4612-1664-3.

[48] R. J. Taylor, 'Body Impedance for Transient High Voltage Currents', in *Electrical Shock Safety Criteria*, J. E. Bridges, G. L. Ford, I. A. Sherman, and M. Vainberg, Eds. Pergamon, 1985, pp. 251–258. doi: 10.1016/B978-0-08-025399-2.50025-4.

[49] C. Gabriel, 'Dielectric Properties of Biological Materials', in *Bioengineering and Biophysical Aspects of Electromagnetic Fields*, 3rd Edition., B. Greenebaum and F. S. Barnes, Eds. USA: CRC Press, 2018, pp. 51–97.

[50] C. Gabriel, 'Compilation of the Dielectric Properties of Body Tissues at RF and Microwave Frequencies.', KING'S COLL LONDON (UNITED KINGDOM) DEPT OF PHYSICS, Jan. 1996. Accessed: Oct. 09, 2019. [Online]. Available: https://apps.dtic.mil/docs/citations/ADA303903

[51] S. Gabriel, R. W. Lau, and C. Gabriel, 'The dielectric properties of biological tissues: III. Parametric models for the dielectric spectrum of tissues', *Phys. Med. Biol.*, vol. 41, no. 11, pp. 2271–2293, Nov. 1996, doi: 10.1088/0031-9155/41/11/003.

[52] J.-P. Gibret, *Human fist different sides*. 2016. Accessed: Aug. 12, 2021. [Online]. Available: https://commons.wikimedia.org/wiki/File:Human_fist_different_sides.svg

[53] SOUTH AFRICAN NATIONAL STANDARD, 'SANS1574-2:2016 - Electric Flexible Cables with Solid Extruded Dielectric Insulation - Part 2: PVC Insulated Flexible Cables for Domestic, Office and Similar Environments (cords)'. SABS Standards Division, Jul. 2016.

[54] G. Elert, ‘Dielectrics’, *The Physics Hypertextbook*. https://physics.info/dielectrics/ (accessed May 19, 2020).

[55] U.S. DEPARTMENT OF HEALTH, EDUCATION, AND WELFARE and Public Health Service, ‘Selected Body Measurements of Children 6-11 Years’, *DHEW Publication No. (HSM) 73-1605*, vol. 11, no. 123, p. 54, Jdnuary 1973.

[56] NASA, ‘Section 3: ANTHROPOMETRY AND BIOMECHANICS’, in *Man-Systems Integration Standards*, Revision B., vol. 1, 2 vols, 1995. Accessed: Jun. 04, 2020. [Online]. Available: https://msis.jsc.nasa.gov/sections/section03.htm

[57] Texas Instruments Incorporated, ‘TI sample | Homepage’. https://samples.ti.com/store/ (accessed Sep. 02, 2020).

[58] Texas Instruments Inc., ‘TL06xx Low-Power JFET-Input Operational Amplifiers’, Texas Instruments Inc., Datasheet SLOS078L, May 2015. Accessed: May 27, 2020. [Online]. Available: https://www.ti.com/store/ti/en/p/product/?p=TL061CDR

[59] Texas Instruments Inc., ‘TL07xx Low-Noise JFET-Input Operational Amplifiers’, Texas Instruments Inc., Datasheet SLOS080N, Jul. 2017. Accessed: May 27, 2020. [Online]. Available: https://www.ti.com/store/ti/en/p/product/?p=TL071CDR

[60] Texas Instruments Inc., ‘TL08xx JFET-Input Operational Amplifiers’, Texas Instruments Inc., Datasheet SLOS081I, May 2015. Accessed: May 27, 2020. [Online]. Available: https://www.ti.com/store/ti/en/p/product/?p=TL081CDR&keyMatch=TL081CDR&tisearch=Search-EN-everything

[61] ‘Left Hand Clip Art Free Download’. https://clipart.me/human-people/left-hand-clip-art-44311 (accessed Feb. 08, 2021).

[62] K. Chinen, I. Kinjo, A. Zamami, K. Irei, and K. Nagayama, ‘New equivalent-electrical circuit model and a practical measurement method for human body impedance’, *Bio-Medical Materials and Engineering*, vol. 26, no. s1, pp. S779–S786, Aug. 2015, doi: 10.3233/BME-151369.

[63] Twitter, *Person standing emoji clipart. Free download transparent .PNG | Creazilla*. Accessed: Oct. 09, 2020. [Online]. Available: https://creazilla.com/nodes/53598-person-standing-emoji-clipart

[64] J.-P. GIBERT, *Human fist from three sides.jpg*. 2016. Accessed: Oct. 09, 2020. [Online]. Available: https://commons.wikimedia.org/wiki/File:Human_fist_different_sides.svg

[65] M. C. Corballis, ‘Bilaterally Symmetrical: To Be or Not to Be?’, *Symmetry*, vol. 12, no. 3, Art. no. 3, Mar. 2020, doi: 10.3390/sym12030326.

[66] M. Čepin, ‘Genetic Algorithm’, in *Assessment of Power System Reliability*, London: Springer London, 2011, pp. 257–269. doi: 10.1007/978-0-85729-688-7_18.

APPENDIX A – CIRCUIT FIGURES OF UNIFIED MODEL

The four circuit figures A1, A2 A3 and A4, are the proposed model for each of the four cases of the main experiment and the validation experiment. Figure A1 and A2 are diagrams of Case 1 and Case 2, respectively were the participant introduced the electromagnetic interference into the body by grasping the lamp's insulated cable with their left hand. Figures A3 and A4 are diagrams of Case 3 and Case 4, respectively were the participant introduced the electromagnetic interference into the body by grasping the lamp's insulated cable with their right hand and served as the validation experiment for the model.

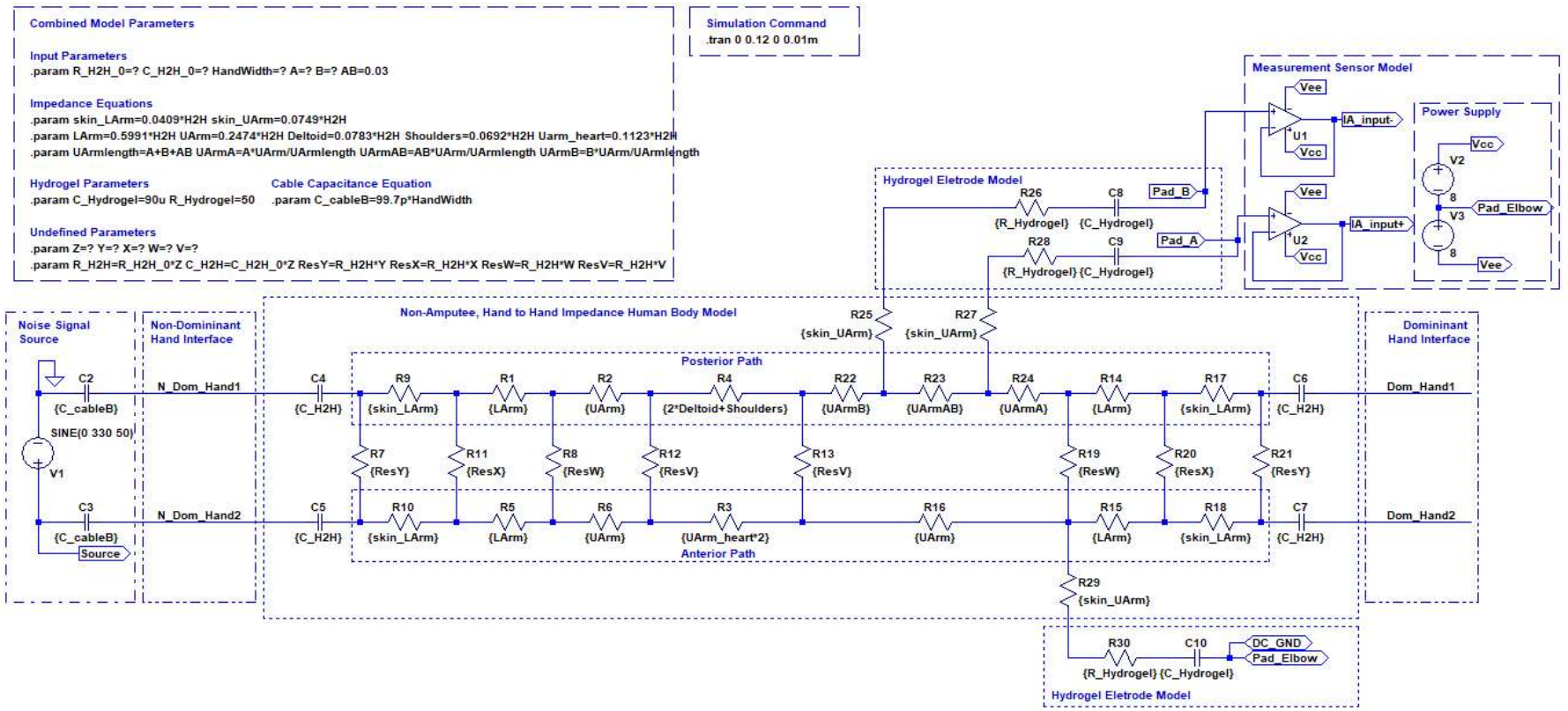


Figure A1 – Model of Experiment for Case 1 Measurement

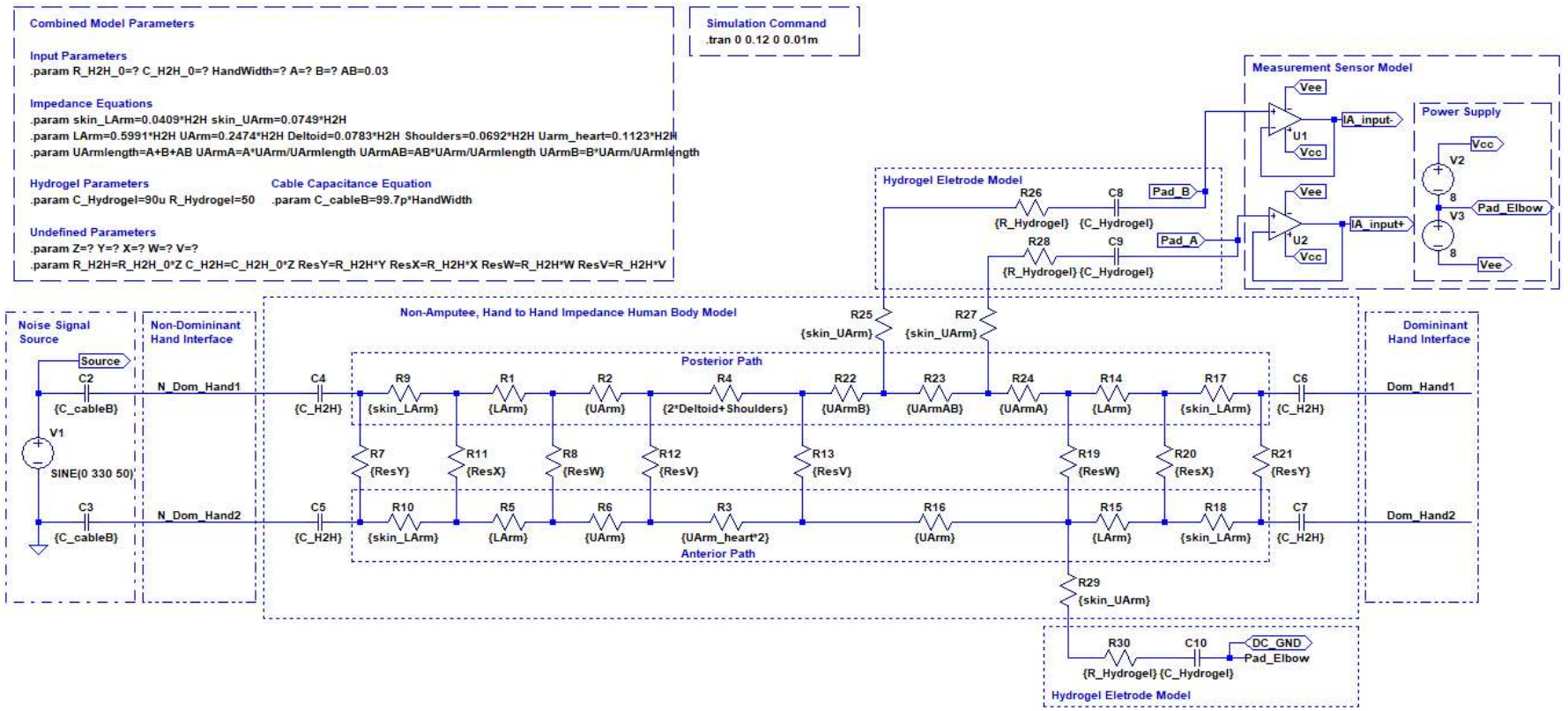


Figure A2 – Model of Experiment for Case 2 Measurements

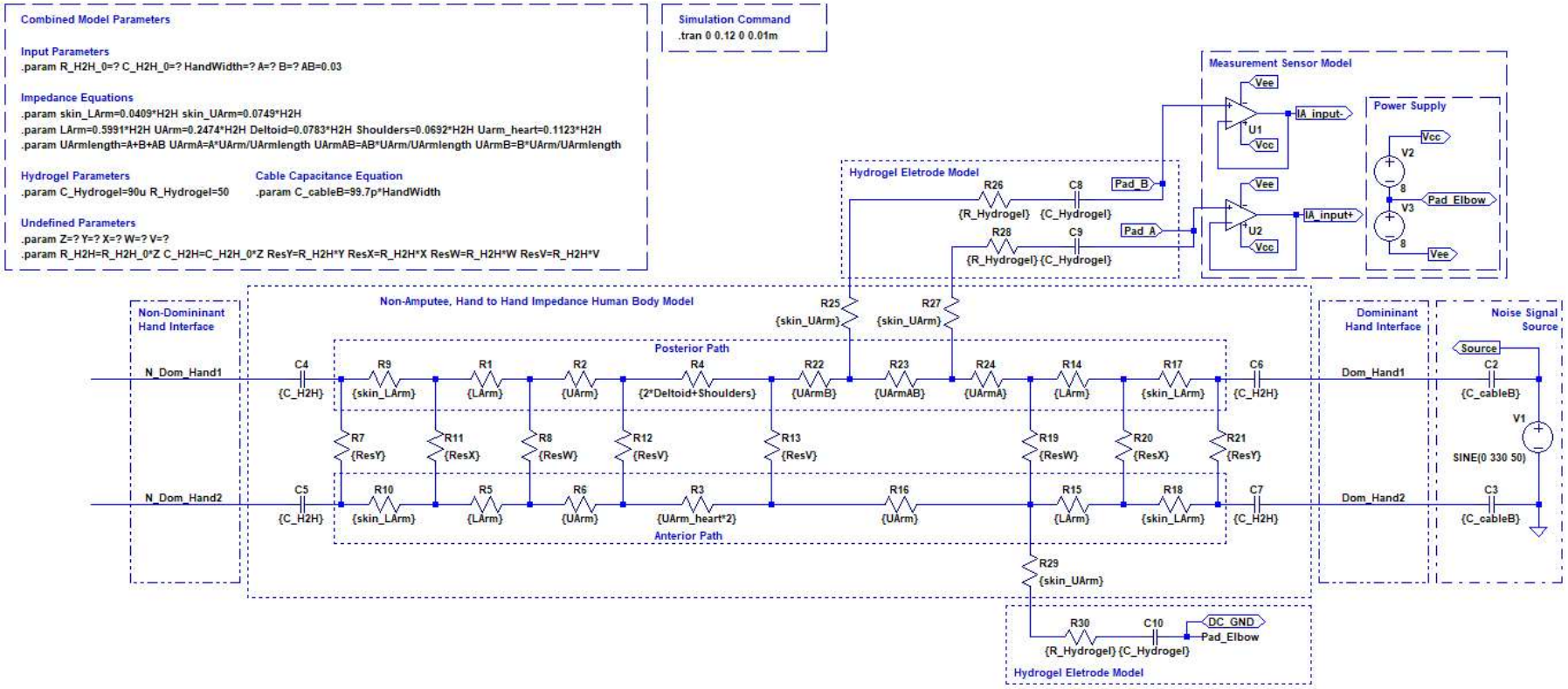


Figure A3 – Model of Experiment for Case 3 Measurements

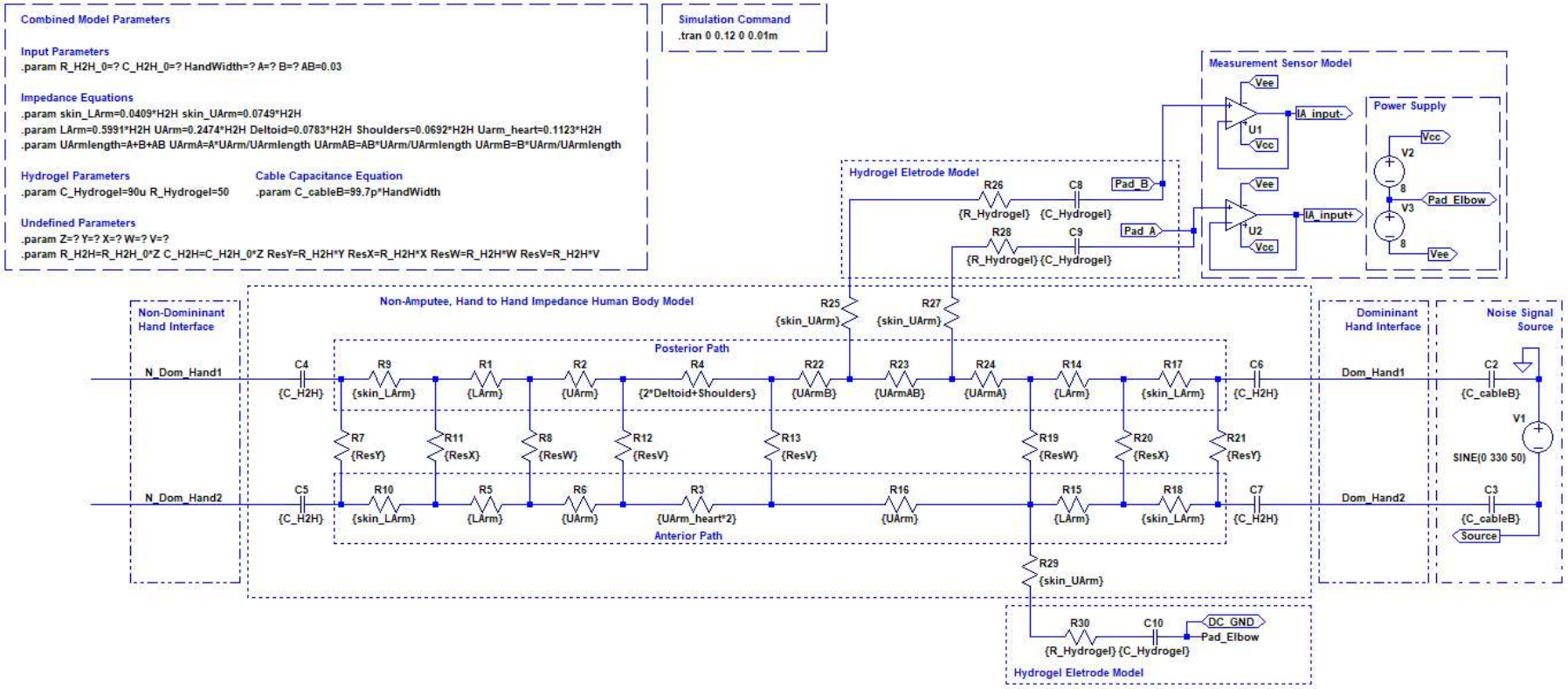


Figure A4 – Model of Experiment for Case 4 Measurements

APPENDIX B – APPLICATION SAMPLE OF GENETIC ALGORITHM – PARTICIPANT A

Using the input parameters that describe Participant A from Table 11 and the desired outputs found in Table 17 and Table 19, the parameter sweep models were generated on LTspice. The setting and results of the generations are shown in the sub-sections below.

The LTspice measurement commands used in the simulation are listed below:

- *.meas TRAN BicepA PP V(Out_A)-V(pad_elbow) FROM 0.02 TO 0.12*
- *.meas TRAN BicepB PP V(Out_B)-V(pad_elbow) FROM 0.02 TO 0.12*

Generation 1

The generation was conducted with the sweep commands listed below.

.step dec param Z 1 100 5
.step dec param Y 1 100 5
.step dec param X 1 100 5
W=X
V=X

The desired parameters that the optimisation needs to obtain are shown in Table 32 and were obtained from Table 19.

TABLE 32 – DESIRED AVERAGE OUTPUT VOLTAGES THAT THE MODEL NEEDS TO OPTIMIZE TO (VALUES OBTAINED FROM TABLE 19)

Case 1	Case 2	Case 3	Case 4	Average	Median
6.69	2.74	9.51	8.34	6.82	7.51

Based on a visual inspection of the desired voltage follower measurements in Table 32, one can infer that the voltage measurement for Case 2 is an outlier because it is the furthest from the median.

The 10 best combinations for Case 1 and Case 2 yielded error percentages between 42 % and 44 %, with *Z=6.31* and *X=1* being popular parameters. The 10 best combinations for Case 3 and Case 4 yielded error percentages between 11 % and 22 %, with *Z= 15.8* and *X=1* being popular parameters

One trend that was identified was that the magnitude of the *V(Out_A) – V(Out_B)* difference was proportional to the magnitude of the *Z* value. As seen in Figure 48 and Figure 49, the values of Z greater than 10 can have a difference in voltage greater than 250 µV which is greater than the fitness criterion magnitude. The result of evaluating *V(Out_A) – V(Out_B)* was that values of *Z* should not be greater than 10 and therefore it is a condition for re-definition of the sweep parameters.

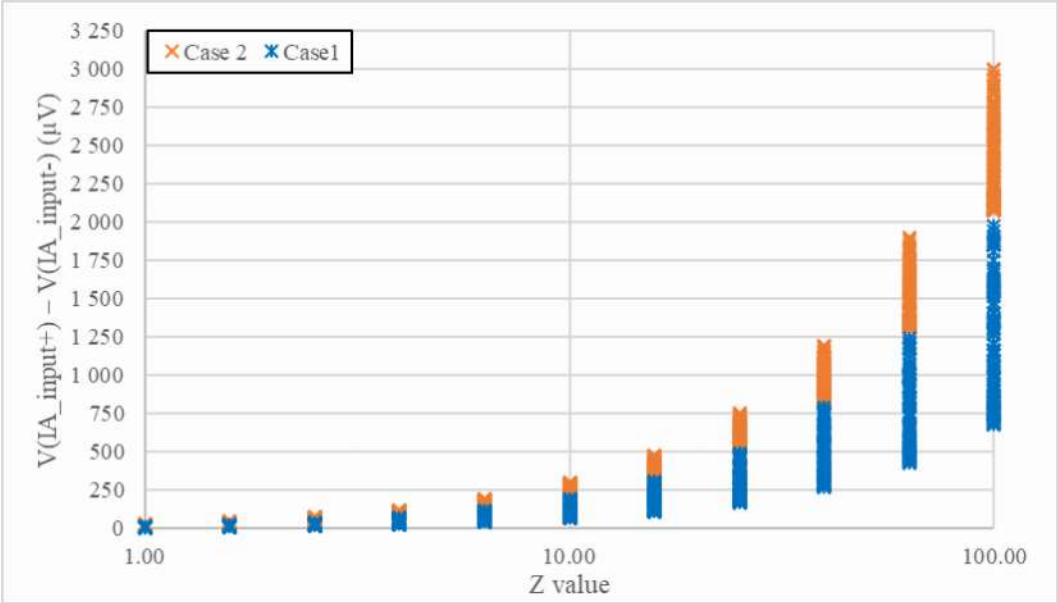


Figure 48 – Comparison of *V(Out_A) – V(Out_B)* against Z Values used in Parameter Optimization for Case 1 and Case 2, for Participant **A** – Generation 1

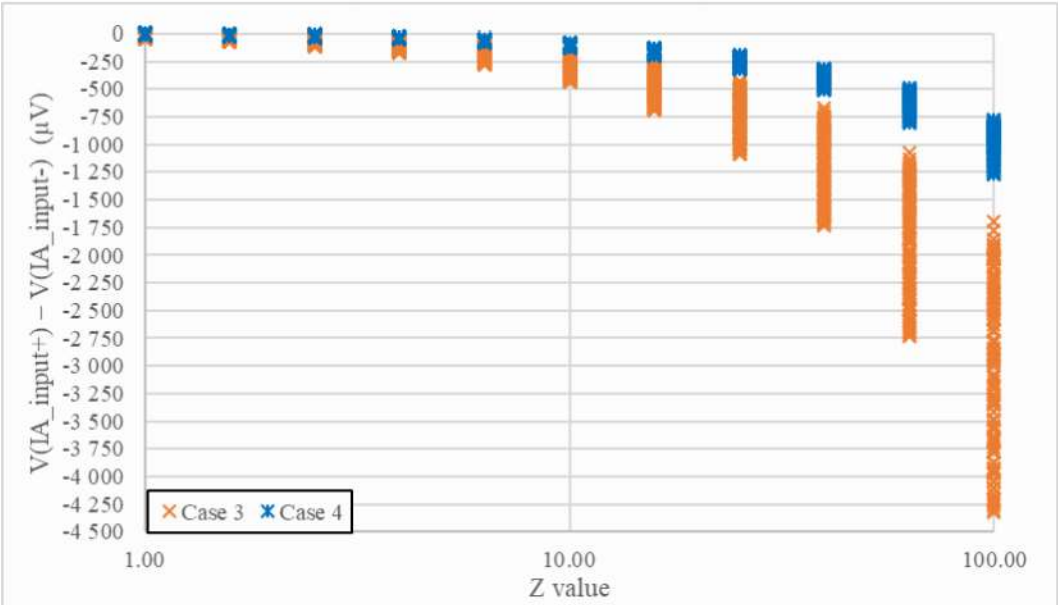


Figure 49 – Comparison of *V(Out_A) – V(Out_B)* against Z Values used in Parameter Optimization for Case 3 and Case 4, for Participant **B** – Generation 1

Generation 2 – Main Experiment Data

The generation was conducted with the sweep commands listed below. The total number of combination in this setup is 1 352.

.step dec param Z 1 10 7

.step dec param Y 1 100 6

.step dec param X 1 100 6

W=X

V=X

The 10 best combinations for Case 1 and Case 2 are shown in Table 33, yielding error percentages between 42 % and 44 %, with *Z= 7.2* and *X=1* being popular parameters. The combination that produces the best fit for then main dataset was *Z=7.19686*, *Y=1* and *X=1*. However, *Y=1* is the smallest number within the range swept values. Therefore, the parameter combination *Z=7.19686* and *Y= 3.16228* for the next generartion because it will allow a wider variation of *X*, *W* and *V* values to be swept.

TABLE 33 – GENERATION 2 – TOP 10 COMBINATIONS OF VARIABLES *Z*, *Y* AND *X* THAT PRODUCED LOWEST RELATIVE ERROR FOR MAIN EXPERIMENT AND MEET NATURAL SELECTION REQUIREMENTS.

Z	Y	X	Is Y ≥ X ?	Case 1	Case 2	Average Relative Error
7.20	1.00	1.00	TRUE	22.17%	99.84%	41.59%
7.20	1.47	1.00	TRUE	21.94%	101.78%	41.90%
7.20	2.15	1.00	TRUE	21.77%	103.66%	42.25%
7.20	3.16	1.00	TRUE	21.66%	105.12%	42.53%
7.20	4.64	1.00	TRUE	21.55%	106.31%	42.74%
7.20	6.81	1.00	TRUE	21.46%	107.28%	42.92%
7.20	10.00	1.00	TRUE	21.43%	107.84%	43.03%
7.20	14.68	1.00	TRUE	21.37%	108.46%	43.15%
7.20	21.54	1.00	TRUE	21.32%	108.67%	43.16%
7.20	31.62	1.00	TRUE	21.32%	108.88%	43.21%

Generation 2 –Validation Experiment Data

The generation was conducted with the sweep commands listed below. The total number of combination in this setup is 1 352.

.step dec param Z 1 10 7

.step dec param Y 1 100 6

.step dec param X 1 100 6

W=X

V=X

The 10 best combinations for Case 3 and Case 4 are shown in Table 34, yielding error percentages between 21.7% and 25.3 %, with *Z= 7.19686* and *X=2.15443* being popular parameters. The combination that produces the best fit for then verification dataset was *Z=7.19686*, *Y= 10* and *X= 2.15.* Therefore, the parameter combination *Z=7.19686* and *Y=10* for the next generartion.

TABLE 34 – GENERATION 2 – TOP 10 COMBINATIONS OF VARIABLES *Z*, *Y* AND *X* THAT PRODUCED LOWEST RELATIVE ERROR FOR VALIDATION EXPERIMENT AND MEET NATURAL SELECTION REQUIREMENTS

Z	Y	X	Is Y ≥ X ?	Case 3	Case 4	Average Relative Error
7.20	10.00	2.15	TRUE	0.68%	42.70%	21.69%
7.20	6.81	2.15	TRUE	1.49%	42.75%	22.12%
7.20	14.68	2.15	TRUE	2.32%	42.62%	22.47%
7.20	4.64	2.15	TRUE	4.32%	42.77%	23.55%
5.18	46.42	3.16	TRUE	0.07%	47.46%	23.77%
5.18	68.13	3.16	TRUE	0.72%	47.35%	24.03%
5.18	100.00	3.16	TRUE	1.12%	47.27%	24.19%
5.18	31.62	3.16	TRUE	0.73%	47.67%	24.20%
5.18	21.54	3.16	TRUE	1.93%	47.90%	24.91%
7.20	3.16	2.15	TRUE	7.91%	42.68%	25.29%

Generation 3 – Main Experiment Data

A third-generation on the main experiment model was conducted with the sweep commands are listed below. The aim was to select intervals for the three variables that would at least range between 1 and constant *Y*'s value and result in a minimum of 1 331 possible combinations across the three variables. Since *Y = 3.16228*, ten intervals per logarithmic decade was required.

.step dec param X 0.316228 3.16228 10

.step dec param W 0.316228 3.16228 10

.step dec param V 0.316228 3.16228 10

Z=7.19686

Y=3.16228

The 10 best combinations for Case 1 and Case 2 are shown in Table 35, yielding error percentages between 40.9 % and 41.6 %. The combination that produces the best fit for then main dataset was *Z=7.19686*, *Y=3.16228, X=W=1.58* and *V=0.316228*.

TABLE 35 – GENERATION 3 − TOP 10 COMBINATIONS OF VARIABLES *Z*, *Y* AND *X* THAT PRODUCED LOWEST RELATIVE ERROR FOR MAIN EXPERIMENT AND MEET NATURAL SELECTION REQUIREMENTS.

X	W	V	Is X ≥ W ≥ V?	Case 1	Case 2	Average Relative Error
1.58	1.58	0.32	TRUE	21.72%	98.58%	40.93%
1.26	1.26	0.32	TRUE	24.68%	89.89%	40.98%
2.00	2.00	0.32	TRUE	19.01%	107.00%	41.01%
1.00	1.00	0.32	TRUE	27.70%	80.99%	41.02%
2.51	2.51	0.32	TRUE	16.53%	114.79%	41.09%
2.00	1.58	0.32	TRUE	21.32%	100.46%	41.10%
1.26	1.00	0.32	TRUE	27.36%	82.38%	41.12%
1.58	1.26	0.32	TRUE	24.31%	91.63%	41.14%
0.79	0.79	0.32	TRUE	30.81%	72.15%	41.15%
2.51	2.00	0.32	TRUE	18.58%	108.88%	41.16%

Generation 3 – Validation Experiment Measurements

A third-generation on the verification experiment model was conducted with the sweep commands are listed below.

.step dec param X 1 10 10
.step dec param W 1 10 10
.step dec param V 1 10 10
Z=7.19686
Y=10

The 10 best combinations for Case 3 and Case 4 are shown in Table 36, yielding error percentages between 23.1 % and 34.67 %. The combination that produces the best fit for then verification dataset was *Z=7.19686*, *Y=10* and *X=W=V= 2.51189.*

TABLE 36 – GENERATION 3 – TOP 10 COMBINATIONS OF VARIABLES *Z*, *Y* AND *X* THAT PRODUCED LOWEST RELATIVE ERROR FOR VALIDATION EXPERIMENT AND MEET NATURAL SELECTION REQUIREMENTS

X	W	V	Is X ≥ W ≥ V?	Case 3	Case 4	Average Relative Error
2.51	2.51	2.51	TRUE	6.41%	39.83%	23.12%
2.51	2.00	2.00	TRUE	4.54%	44.18%	24.36%
2.00	2.00	2.00	TRUE	9.27%	44.24%	26.75%
2.51	2.00	1.58	TRUE	8.47%	45.76%	27.11%
2.00	2.00	1.58	TRUE	12.88%	45.79%	29.34%
3.16	1.58	1.58	TRUE	10.80%	48.08%	29.44%
2.51	1.58	1.58	TRUE	14.61%	48.22%	31.41%
2.00	1.58	1.58	TRUE	18.54%	48.17%	33.35%
2.51	1.58	1.26	TRUE	17.99%	49.57%	33.78%
3.98	1.26	1.26	TRUE	17.81%	51.71%	34.76%

Simulation Considerations

A few changes and processes were considered to reduce errors, unnecessary computations and simplify the population for the parameter sweeping.

Number of Generations Required

The simulations of the genetic algorithm conducted in the last section had two generations to determine the constants *Z* and *Y*, and one generation to determine the constants *X*, *W* and *V*. Since the trend of *V(Out_A) – V(Out_B)* difference was proportional to the magnitude of the *Z* value was seen with the first participant. It was decided that to reduce computation time, the remaining participants will begin their genetic algorithm at Generation 2. This is assuming that a similar outcome would occur and it was considered unnecessary to evaluate combinations that do not meet the Fitness criteria.

Population Control

The natural selection process involved generating the simulation and transferring the text file data to a spreadsheet, to perform calculations. The manual operations

required a template spreadsheet to be devised for speeding up the calculation process.

Generation 2, being a starting point, was straight-forward in determining the parameter settings and was shared across all the participants. The parameters for Generation 3, being dependant on the constant *Y* from Generation 2, would require different rules based on the constant *Y*'s value. To maintain either the population at 1 000 combinations and nine intervals per logarithmic decade.

If constant $Y \leq 10$, then the minimum limit would be equal to $0.1 \times Y$ and the maximum limit would be equal to Y, which would result in 1 000 combinations if there was 9 interval per logarithmic decade. The additional benefit to this is that common numbers between limits will exist and will ease median and mode calculations.

If constant $Y > 10$, then the minimum and maximum limits will be '1' and 'Y, respectively. But due to the computing limit of 1 400 combinations for parameter sweeping, a custom parameter setup will need to be devised to find a good compromise between the use of higher-order intervals and computational time.

APPENDIX C - DETERMINING INTER-PATHWAY RESISTANCES USING GENETIC ALGORITHM

Currently, the model is incomplete due to the unknown parameters *Z*, *Y*, *X*, *W*, and *V*, which represent the resistances between the anterior and posterior paths for the Stratum Corneum surface, wrist region, elbow region and shoulder region, as a scaled factor of the H2H impedance.

It was decided to perform a Genetic Algorithm-based method using the known inputs and outputs, listed below, to determine the five constants.

- Inputs
    - Hand-to-hand Resistance (R_{H2H_0})
    - Hand-to-hand Capacitance (C_{H2H_0})
    - Hand Width
    - The span between Elbow electrode to Electrode A (Span A)
    - The span between Shoulder to Electrode B (Span B)
    - Source
- Outputs
    - IA Input Voltages

- Difference between voltages

Genetic Algorithm takes inspiration from the concept of natural evolution where the organisms with 'high suitability' or 'fitness' given environment survive to populate the next generation. This algorithm is a probabilistic search method based on natural selection and genetic recombination principles and uses historical information to evaluate new search points with the better performance [66].

7.2.1. Model Amendments

The three aspects of the model development that were amended due to modelling complications and reducing model complexity are:

- Use of Phase Difference for model optimisation,
- use of power supply Source Recording, and
- using the op-amp TL081 SPICE model.

Phase Difference

Using the phase differences between the power source and the *Out_A* and *Out_B* phases as an optimisation parameter may have a benefit in producing a more accurate Human Body circuit model. However, concurrent optimisation for two important parameters add complexity and may hinder the viability of the model proposed.

Power Supply Source Recording

Initial plans involved using the source measurement recording, taken during each case measurement, as an input waveform for the CC model. However, due to the model not producing 50 Hz waveforms at the voltage follower outputs, it was replaced by a pure sine wave source.

A further simplification was to make all the participant's models use 330 V_{PEAK}, 50 Hz sine wave as an input waveform for the CC model because the median for the source voltage peak was 330 V. The range of the minimum and maximum V_{PEAK} was at most a 0.6% deviation from the median. and it is assumed that fixing all the at 330 V would simplify the modelling process and contribute a negligible error to the final model accuracy.

TL081 SPICE model

The measurement sensor was included as part of the components that influence the measurements. Originally, the TL081's SPICE netlist was intended to be used in the model, however, there were compatibility complications with the SPICE model and the floating ground reference. To maintain the floating ground, the virtual op-amp with the settings described in Figure 27 was used to compensate.

7.2.2. Genetic Algorithm Pseudo-Code

The flow of the pseudo-code for the desired algorithm is shown in Figure 50. The process begins with definitions which in this case are the model developed, the known inputs and outputs described in the section above and undefined constants.

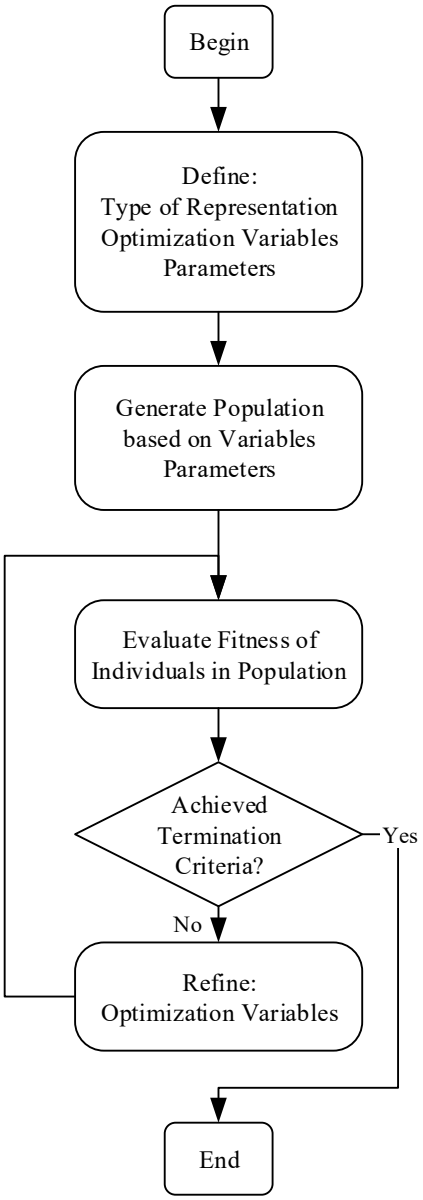


Figure 50 – Flowchart of the Pseudo-code for the desired Genetic Algorithm [66]

Population

The population will be composed of the combinations of the undefined parameters. Since the model is developed on LTspice, there is a limit of three parameters that parameter sweep function (*.step*) can process in one simulation, Therefore, the algorithm will have two stages of tuning. The first stage will evaluate the unknown parameters *Z*, *Y* and *X*. Once a suitable *Z* and *Y* constant are found, then the second stage begins where the parameters *X*, *W*, and *V* will be swept. The unknown

parameters values will be swept logarithmically across the decades at a given number of intervals. Ideally, the total number of combinations was set between 1 000 and 1 400. Since the unknown parameters are scaling up factors, the range of values was arbitrarily selected between 1 and 100.

Fitness Evaluation

The population fitness was evaluated by the measurement:

- Relative error percentage between the experiment's *Out_A* and *Out_B*'s combined average magnitude, and the simulation's average magnitude for each Case, and
- Difference between the *Out_A* and *Out_B*'s magnitude voltage for each Case,

Due to the experimental dataset's skewness found in Table 19, the best combination of parameters *Z*, *Y*, *X*, *W* and *V* was the combination that produced the least relative error. This relative error was determined in two different way depending on the outcome of Table 19 which separates the participants into those with relatively un-skewed data (shaded grey in Table 19) and the relatively skewed data (unshaded in Table 19).

The relatively unskewed data will have equal error weighting in the fitness evaluation of 50% because the main experiment measurements and the validation experiment measurements are evaluated separately. The skewed data will have unequal error weighting, where the outlier will have a lower weighting of 25% instead of eliminating it. This unequal weighting can occur in either the main experiment measurements and the validation experiment measurements, but never in both. This was done to reduce the effect of error percentages due to a case with outlier measurements.

If several combinations yield adequate results in the first stage, the combination with the higher *Y* value will be selected as it allows for a greater range of *X*, *W* and *V* values. The combinations also had to meet the following criteria:

- Equation (10) which describes that $Y > X > W > V$, and
- The difference between the IA input voltages for each Case should have a magnitude less than 200 μV which was an approximately a 50 % deviation on the maximum of 128 μV found in the experiment data.

Note that the voltage follower outputs were measured with reference to the DC ground or the elbow electrode. The node math for *Out_A* and *Out_B* respectively was defined as Equations (18) and (19) below.

$$V(Out_A) - V(Pad_Elbow) \tag{18}$$

$$V(Out_B) - V(Pad_Elbow) \tag{19}$$

Termination Criterion

The genetic algorithm will end after the third generation has been developed. Therefore, there is no criterion directly implemented on the data produced by the model.

Refine Population

Originally, this part of the pseudo-code involved the genetic recombination processes such as genetic selection, genetic crossover, and genetic mutation [66]. However, due to the non-automated approach to optimising the variables in the model, it was preferred to increase the precision on a range of numbers that yield successful fitness criteria.

7.2.3. Applying the Genetic Algorithm

From the experience of processing the experiment data, it is known that there may have flaws in the application of the experiment and due to the multivariable nature of defining a human into a measurable set of parameters, it was decided to model each participant individually to obtain minimal errors in the model. Appendix B demonstrates the application of the devised genetic algorithm using Participant A as a sample.